ENERGY AND CHARGE STATE DEPENDENCES OF TRANSFER IONIZATION TO SINGLE CAPTURE RATIO FOR FAST MULTIPLY CHARGED IONS ON HELIUM

by

RIDVAN UNAL

B.S., Middle East Technical University, 1988

M.S., Kansas State University, 1997

AN ABSTRACT OF A DISSERTATION

Submitted in partial fulfillment of the
Requirements for the degree

DOCTOR OF PHILOSOPHY

Department of Physics
College of Arts and Sciences

KANSAS STATE UNIVERSITY
Manhattan, Kansas
2001

ABSTRACT

The charge state and energy dependences of Transfer Ionization (TI) and Single Capture (SC) processes in collisions of multiply charged ions with He from intermediate to high velocities are investigated using coincident recoil ion momentum spectroscopy. The collision chamber is commissioned on the 15-degree port of a switching magnet, which allows the delivery of a beam with very little impurity. The target was provided from a supersonic He jet with a two-stage collimation. The two-stage, geometrically cooled, supersonic He jet has significantly reduced background contribution to the spectrum compared to a single stage He jet. In the case of a differentially pumped gas cell complex calculations based on assumptions for the correction due to the collisions with the contaminant beam led to corrections, which were up to 50%. The new setup allows one to make a direct separation of contaminant processes in the experimental data using the longitudinal momentum spectra. Furthermore, this correction is much smaller (about 8.8%) yielding better overall precision.

The collision systems reported here are 1 MeV/u $O^{(4-8)+}$, 0.5-2.5 MeV/u $F^{(4-9)+}$, 2.0 MeV/u $Ti^{15,17,18+}$, 1.6-1.75 MeV/u $Cu^{18,20+}$ and 0.25-0.5 MeV/u $I^{(15-25)+}$ ions interacting with helium. We have determined the $\frac{s_{TI}}{s_{SC}}$ ratio for high velocity highly charged ions on He at velocities in the range of 6 to 10 au and observed that the ratio is monotonically decreasing with velocity. Furthermore, we see a ratio that follows a q^2 dependence. Above q = 9 the experimental values exceed the q^2 dependence prediction due to antiscreening. C. D. Lin and H. C. Tseng have performed coupled channel calculations for the energy dependence of TI and SC for F^{9+} + He and find values slightly higher than our measured values, but with approximately the same energy dependence. The new data, Si, Ti and Cu, go up only to q = 20 and show a smooth monotonically increasing TI/SC ratio. The TI/SC ratio for $I^{(15-25)+}$ demonstrates a very steep rise with energy and disagrees with previous measurements in the literature at 0.25 MeV/u. The latter data clarifies one of the long standing puzzles in the relative TI/SC cross sections for very high q-ions.

ENERGY AND CHARGE STATE DEPENDENCES OF TRANSFER IONIZATION TO SINGLE CAPTURE RATIO FOR FAST MULTIPLY CHARGED IONS ON HELIUM

by

RIDVAN UNAL

B.S., Middle East Technical University, 1988

M.S., Kansas State University, 1997

A DISSERTATION

Submitted in partial fulfillment of the
Requirements for the degree

DOCTOR OF PHILOSOPHY

Department of Physics
College of Arts and Sciences

KANSAS STATE UNIVERSITY
Manhattan, Kansas
2001

Approved:

Major Professor
Patrick Richard

TABLE OF CONTENTS

LIST OF TABLES ……..…….….iii

LIST OF FIGURES …….…….…….iv

ACKNOWLEGEMENTS…….……...…..vii

I. INTRODUCTION…….…...1

II. LITERATURE REVIEW…….……...…5

Transfer Ionization Mechanisms ……...…...……11

i. Kinematical Capture plus Ionization, KC-I TI……....…….…..11

ii. p-e-n Thomas TI……...…...……..….13

iii. p-e-e Thomas TI……...……..…13

iv. Correlated Kinematical Capture and Ionization (c-K-TI)…….…….15

Motivation for the Present Study……...…..…….16

III. EXPERIMENT……...……19

J. R. Macdonald Laboratory and the tandem Van de Graaff……..19

Superconducting Heavy-Ion Booster Linear Accelerator (LINAC)…….……..21

Experimental Setup……...…..…22

Spectrometer…….…..26

Calculation of the TOF……...……27

Recoil detector….……...…29

Electronics…….……..……..……..30

Data Collection and Analysis….……..……..……..…32

IV. RESULTS AND DISCUSSION……..……..….…….39

A. TI and SC in 1 MeV/u O^{8+} + He: A Test Case…….....39

B. Systematic Study of Velocity and Charge State Dependences of TI to SC Ratio for F^{q+} Incident on He……...….……...……...48

C. Total One-Electron Transfer Cross Sections for F^{9+} and F^{8+} Incident on He…...62
D. TI and SC for Z > 9 projectiles……..…….…....69
E. Mechanisms for Transfer ionization Ion-He Collisions…….……..…..82
V. CONCLUDING REMARKS……86
References……..…….89
Appendix A: Calibration of the Detector……...94
Appendix B: Spectrometer Dimensions…….98
Appendix C: Data Acquisition and Analysis Code……99
ABSTRACT

LIST OF TABLES

Table Page

4.1. The ratio of transfer ionization to single capture for F^{q+} incident on He……..…..50

4.2. Measured cross sections for one-electron transfer, single capture and transfer ionization for F^{8+} incident on He……...62

4.3. Measured cross sections for one-electron transfer, single capture and transfer ionization for F^{9+} incident on He……...65

4.4. The ratio of transfer ionization to single capture for 2 MeV/u A^{q+} incident on He…….……..70

4.5. The ratio of transfer ionization to single capture for 1.6 and 1.75 MeV/u Cu^{q+} incident on He……..……..…...……..71

4.6. The ratio of transfer ionization to single capture for I^{q+} incident on He…….72

LIST OF FIGURES

Figure Page

2.1 Single ionization (SI) and single capture (total single projectile charge change, i.e., SC+TI, at lower velocities) cross sections for O^{8+} on He……..……7

2.2. Ratio of cross sections $s^{2+}/(s^{+}+s^{2+})$ for capture plus ionization……...….8

2.3. Ratio of the cross sections of transfer ionization and single capture for 2 MeV/u projectile ions incident on He……...…..10

2.4 The schematic representation of the kinematical capture and independent ionization that makes the KC-I TI process (TS2)……..…….12

2.6. The schematic representation of the e-e Thomas scattering for H^{+}-He collision...…14

2.7. Comparison of probabilities with respect to impact parameters for different channels with different effective potentials at 1MeV…….17

3.1. Top view of the J. R. Macdonald Laboratory. The COLTRIMS experimental setup is commissioned at the LRB-15 port…….19

3.2. NEC Pelletron Charging System for a positive terminal Pelletron…….20

3.3. Schematic diagram of the experimental apparatus……...…..24

3.4. Two-stage gas jet assembly……...25

3.5. 2-D Detector (e-side) and spectrometer…….……28

3.6. POVRAY image of experimental setup……...……..29

3.7. Block diagram of electronics……...……..31

3.8. 2.0 MeV/u F^{5+} on He as data were being collected……...33

3.9. A screen print of 2 MeV/u F^{5+} on He during data analysis for single capture case…….…...34

3.10. A screen print of 2 MeV/u F^{5+} on He during data analysis for transfer ionization case……..…...35

3.11.1.75 MeV/u Cl^{14+} on He as data were being collected……..…....36

3.12. The TAC spectra for 1.75 MeV/u Cl^{14+}on He ……..……....37

3.13.Gate on He^{++} TAC peak as seen on recoil detector……...…38

4.1. The 2-D recoil ion momentum spectrum of He^{+} ions in coincidence with O^{4+} from 1 MeV/u O^{5+} He……..41

4.2.The 2-D recoil ion momentum spectrum of He^{2+} ions in coincidence with O^{4+} from 1 MeV/u O^{5+} + He collisions as observed on the position sensitive recoil-ion detector…….43

4.3. TI to SC ratio for 1 MeV/u O^{q+} incident on He……..45

4.4. The ratio of transfer ionization to single capture for 0.5 MeV/u $F^{(4-8)+}$ incident on He……...…….52

4.5. The ratio of transfer ionization to single capture for 0.75 MeV/u $F^{(4-8)+}$ incident on He……...….53

4.6. The ratio of transfer ionization to single capture for 1.0 MeV/u $F^{(4-9)+}$ incident on He……54

4.7. The ratio of transfer ionization to single capture for 1.25 MeV/u $F^{(4-9)+}$ incident on He……...….55

4.8. The ratio of transfer ionization to single capture for 1.5 MeV/u $F^{(4-9)+}$ incident on He……...……56

4.9. The ratio of transfer ionization to single capture for 1.75 MeV/u $F^{(4-9)+}$ incident on He……57

4.10. The ratio of transfer ionization to single capture for 2.0 MeV/u $F^{(4-9)+}$ incident on He…….……58

4.11. The ratio of transfer ionization to single capture for 2.5 MeV/u $F^{(5-9)+}$ incident on He……59

4.12. The ratio of transfer ionization to single capture for F^{9+} incident on He…….61

4.13. Cross sections for total one-electron transfer, single capture, and transfer ionization for F^{8+} incident on He……...….63

4.14. Total one-electron transfer cross sections for F^{9+} incident on He……...66

4.15. Cross sections for total one-electron transfer, single capture, and transfer ionization for F^{9+} incident on He……..……..……67

4.16. Cross sections for total one-electron transfer, single capture, and transfer ionization for F^{9+} incident on He……68

4.17. Charge state dependence of SC and TI processes in 2 MeV/u A^{q+} on He system……...73

4.18. Charge state dependence of SC and TI processes in 2 MeV/u A^{q+} on He system…….74

4.19. Charge state dependence of SC and TI processes in A^{q+} on He system……...…75

4.20. The ratio of transfer ionization to single capture for 0.25 MeV/u I^{q+} incident on He……..76

4.21. The ratio of transfer ionization to single capture for 0.375 MeV/u I^{q+} incident on He……..77

4.22. The ratio of transfer ionization to single capture for 0.5 MeV/u I^{q+} incident on He……..78

4.23. Energy dependence of the ratio of $\frac{s_{TI}}{s_{SC}}$ for I^{19+} on He. Datz *et al*.[49] data are for I^{16+} at 0.10 MeV/u and for I^{19+} at 0.25 MeV/u……..79

4.24. Charge state dependence of SC and TI processes in A^{q+} on He system……...80

4.25. Velocity dependence of scaled ratio of $\frac{s_{TI}}{s_{SC}}$ for H^{+} on He and the scaled ratio of $\frac{s_{TI}}{s_{SC}}$ for $F^{(8\text{-}9)+}$ on He……..84

4.26. Velocity dependence of scaled ratio of $\frac{s_{TI}}{s_{SC}}$ for H^{+} on He and the scaled ratio of $\frac{s_{TI}}{s_{SC}}$ for F^{9+} on He with: $R(scaled) = \frac{R(measured) - R(shake)}{Z^2} + R(shake)$ …85

ACKNOWLEDGMENTS

I wish to thank my major professor, Pat Richard, for his help, encouragement, and patience throughout my studies. He is a true example for me as a physicist and as a person. He taught me a lot as a scientist, as an educator, and as a human being. His teachings will be a guide for me in my professional life. I wish to thank him especially for his understanding and care during my medical setbacks.

I wish to extend my thanks to my committee members, C. D. Lin, Itzik Ben-Itzhak, Peter Sherwood, and D. V. Satish Chandra, my outside chair. Special thanks go to C. D. Lin for his help and teaching me atomic physics. I also would like to thank Itzik Ben-Itzhak for his helpful discussions during my beam times in the Macdonald Laboratory. For all of his assistance in keeping the research facility up and running, my thanks to Tom Gray, and also to Kevin Carnes for tuning the LINAC and helping with computer issues, and all the many things for which are hard to list here. I also wish to extend my thanks to Vince Needham for coming three or four times at night to fix resonators when Mother Nature caused them to fail, in particular during my beam time runs.

I wish to thank Mike Wells and Al Rankin for their professional skills and their friendship during my studies here. I appreciate their willingness to help me whenever I needed their assistance. I wish to extend my thanks to Bob Krause for keeping the tandem and source up and running during my experiments. Bob Krause started the source many times during the weekend, sacrificing his free time. I would like to acknowledge the help I received from the machine and electronics shops, especially from Dave Hill, Bob Geering, Ron Jackson, and Scott Chainey.

My appreciation goes to Mahendrajit Singh for designing the gas jet and chamber used in my research, and Hiro Tawara for helping me with beam times during his visits to Kansas State. I wish to extend my thanks also to my colleagues, Habib Aliabadi, Mikhail Zamkov, and Manolis Benis for their helpful discussions, help during my beam times and their friendship that made my research easier and enjoyable. Also, I would like to thank Nathan Woody and Omur Kalkan for baby-sitting the tandem during the beam times and especially Nathan Woody for assisting me with the POVRAY figures.

I wish to extend my special thanks to Dea Richard for reading the manuscript and making invaluable suggestions that made my dissertation more readable and for listening to me patiently during my research days.

Also, I wish to extend very special thanks to my wife, friend, mother of my children, and true love, Nurten Unal, for her patience and encouragement throughout our marriage, and in particular during the difficult times I experienced medical setbacks.
I truly admire her for the care she gives to our children. I would like to thank my sons, Boran and Ahmet, for making my studies and life very exciting. They have asked very hard questions like 'when will I be done' and 'will I be completely through with school', and especially when they thought they should not go to grade school but instead begin their education at the graduate level. I wish to extend to my lovely daughter, Gizem, for being a beautiful part of our family. My thanks also go to my family members, especially to my Father and Mother, for their patience and encouragement over many miles and many years. Surely I have missed them all of the time.

I wish to thank my in-laws for their visit with us and their encouragement during my studies.

I. INTRODUCTION

Since the first decade of the last century, charge transfer cross sections for multiply charged projectiles in gas targets have been investigated.[1-4] These charge transfer cross sections are useful not only for testing theoretical calculations but also for a variety of applications including (but not limited to) accelerator design, beam transport, radiation damage in biological and other materials, astrophysical processes, and fusion energy technology.[5,6]

The quantitative investigation of charge transfer began in the 1920's by using naturally radioactive sources of alpha particles. In the 1950's, high-energy studies of charge transfer were facilitated with the cyclotron and the lower-energy Cockcroft-Walton accelerators that are used in nuclear research. In the 1960's tandem Van de Graaff accelerators were introduced into use for accelerating high-energy heavy ions. In the last two decades, researchers have intensified their studies in charge transfer.

Collisions involving multiply charged ions and neutral atoms are characterized by the presence and simultaneous action of several collision channels, resulting in multi-electron transitions within and between participating systems. One of the simplest examples of the interacting two electron-collision systems is the collision between fully stripped ions and the helium atom. For two electron target atoms both one- and two electron transitions are possible. These processes can be specified as follows:

$A^{q+} + He \rightarrow A^{q+} + He^{+} + e$	SI	- Single ionization
$\rightarrow A^{(q-1)+} + He^{+}$	SC	- Single electron capture
$\rightarrow A^{(q-1)+} + He^{2+} + e$	TI	- Transfer ionization
$\rightarrow A^{q+} + He^{2+} + e + e$	DI	- Double ionization
$\rightarrow A^{(q-2)+} + He^{2+}$	DC	- Double electron capture

Many reviews of charge transfer have been published since the 1950's. The authors of some of the reviews are listed here: Massey and Burhop[7], Allison[8], Allison and

Garcia-Munoz[9], Hasted[10], Betz[11], Tawara and Russek[12], Massey and Gilbody[13], Gilbody[14], and Bransden and McDowell[15].

In this thesis transfer ionization and the ratio of transfer ionization to single capture for fast highly charged ions on He will be investigated over a very large range of projectile Z and projectile energy. The thesis will be divided into five sections: I Introduction, II Literature Review, III Experiment, IV Results and Discussion, and V Conclusions.

In section II, Literature Review, the different transfer ionization channels that have been discussed in the literature will be explored. The transfer ionization process, which involves at least four interacting particles, can proceed via different proposed reaction channels that have been identified as:

i. Kinematical Capture-Ionization, KC-I TI
ii. Projectile-Electron-Nucleus- Thomas, p-e-n Thomas TI
iii. Projectile-Electron-Electron Thomas, p-e-e Thomas TI
iv. Correlated Kinematical Capture TI

For the systems of fast highly charged ions, we expect that TI results primarily from two independent scattering interactions with the projectile (KC-I-TI). The transfer ionization probability can then be expressed as the product of the capture probability times the ionization probability at a given transverse momentum. Under these conditions, the ratio of total TI cross sections to total capture cross sections should drop with $1/E_p$ at the higher velocities. In the Literature Review section we will discuss some details of the different TI processes and review some of the recent experiments. In addition to the TI process, we will elaborate on the Single Capture (SC) process and the TI-to-SC ratio. Furthermore, the related theoretical studies also will be introduced and compared with the experimental results. This discussion will help the reader to get a better grasp of the problem and findings.

In Section III. Experiment, the details of recoil momentum spectroscopy, RIMS, which is the experimental technique used in this study, will be discussed. In general, the RIMS method was first explored in the sixties.[16-19] However, the momentum spread of the target due to the thermal motion of the gas made the technique unusable. The method used in the late seventies and early eighties was revisited. Fortunately, this time the

method was successfully implemented. With the implementation of super cooled gas jet targets, it was possible to obtain some promising final state scattering results. In the nineties the RIMS method[20-33] evolved into Cold Target Recoil Ion Momentum Spectroscopy (COLTRIMS)[34,35] in which the complete momentum balance could be measured with high resolution and high detection efficiency in the few-particle final product stage. In the RIMS method, the longitudinal momentum component and transverse momentum components carry different information. The longitudinal momentum component measurements will reveal information about Q-values that gives the exoergicity of the reaction. On the other hand, the transverse component can be related to the impact parameter and the resulting angular scattering, which is a significant result.

Also in that section is a detailed discussion of our experimental setup. Since we have used both the KSU tandem electrostatic and LINAC accelerators, detailed information about both accelerators will be provided. Readers also will find an extensive discussion and information about the present RIMS setup and more specifically about the geometrically cooled two-stage supersonic helium gas jet, spectrometer, detectors and diagnostic tools on the beam line used for the experiment.

In Section IV. Results and Discussion, the results of our measurements of the TI-to-SC ratio for the fast multiply charged ions on He are reported. Some of the results will be compared with the quantum mechanical coupled-channel calculation. Comparisons are also made with previous data available in the literature. Significant differences are observed between the present measurements and those found in the literature. The present method of RIMS using a supersonic He jet eliminates a problem of impurity interactions encountered in static gas cell methods used in the prior experiments. This is the main contribution of this work. The record is set straight on the relative roles of TI and SC over a large range of collision parameter space. The methods of Q-value measurements as well as the impact parameter analysis will be included in the discussion.

The last section, V Conclusions, includes, but is not limited to, a summary and conclusions we have been able to make from this series of experiments. Possible improvements and future directions of the current measurements also will be presented.

Three appendices are included at the end of the dissertation that contain details of the experimental technique for future reference.

II. LITERATURE REVIEW

In the earlier measurements of single electron transfer from multi-electron targets, the single capture and the transfer ionization channels were not separated,[2,3] i.e both of them contribute to the single-electron-transfer cross section. These measurements were based only on the final charge state distribution following an ion-atom collision.

Fig. 2.1 shows extensive data for capture and ionization available over a wide range of velocities for O^{8+} on He. Measured single electron transfer (SC + TI) cross sections are very flat at the lowest energies up to 1.64 a.u. of velocity compared with measurements above 3.0 a.u. where a sharp decrease with increasing velocity is seen[36]. The data show that the capture process dominates over single ionization up to 2.0 a.u. of velocity. It is evident from the data that the crossover between capture and ionization are expected to occur between $v = 2 - 3 a.u.$ for O^{8+} on He.[36] In the data depicted in Fig. 2.1, the contribution of the TI process is not separated from the true SC process. In the present study we will make that differentiation between these processes for the velocity range of ~4 to 12 a.u. The weak velocity dependence of SC in the low velocity region could be explained with the molecular-orbital (MO) model. However, the MO model is not valid in the high velocity region. Besides, since target ionization can accompany capture, the TI contribution to the electron transfer process should be measured.

In 1979, Horsdal-Pedersen and Larsen[45] reported the measurements of the relative contributions of SC and TI processes to the total transfer process for protons on He in the energy range of 40-400 keV for the first time. Then in 1985, Shah and Gilbody[46] extended these measurements to H^+, He^{2+}, and Li^{3+} for almost the same projectile energy range. Later Knudsen *et al.*[4] extended the projectile energy range for H^+ and He^{2+} up to 1.0 and 1.5 MeV/u, respectively. Fig. 2.2 shows these data along with very low energy data compiled by McGuire *et al.*[47] They have plotted the ratio of transfer ionization to the total one-electron transfer cross section. Since then it has become customary to discuss this process in terms of the ratio of TI-to-SC. In the last decade, measurements made by Tanis *et al.*[48] and Shinpaugh *et al.*[38] for high charge bare projectiles have extended the scope of these measurements to a parameter space where TI can equal or even exceed the single capture. Non-bare projectile ions were included in the study by Tanis *et al.*[48], Datz *et al.*[49], Wu *et al.*[36], and Montenegro *et al.*[50] Fig. 2.3 shows the ratio of the cross sections

of transfer ionization and single capture for 2 MeV/u projectile ions incident on He. In the graph, the theoretical calculation by Shingal *et al.*[51] is also included. Montenegro *et al.*[50] studied 2 MeV/u $Cl^{7+, 9+, 13+, 14+, 15+}$ and $Ti^{15+, 18+}$ on He. Three features appearing in the graph need to be pointed out: the ratio R is expected to have a weak connection with the capture channel for small values of q presenting the characteristic quadratic q dependence of the ionization channel, which was observed previously for bare light ions.[4] The second feature is the observed saturation effect for the ratio between Cl^{14+} and Cl^{15+} projectiles. However, the same effect was not observed in the case of Ti^{15+} and Ti^{18+}. The third feature is the observed difference in the trend of the TI/SC ratio between Montenegro *et al.*[50]and Datz *et al.*[49] measurements. However, there is still a large gap between the projectile charge states used in these two sets of data, and the projectile energy used in these measurements. We should also note that different experimental techniques have been employed. Since the capture channel has low intensity for high projectile velocity and charge states, it can contribute to errors in the TI/SC ratio measurements. Furthermore, small beam impurities can be a major source of error in this kind of measurement if not properly separated. Datz *et al.*[49] have determined the fraction of TI contributing to the total single charge transfer by using the TOF technique with a gas cell. They have not employed longitudinal momentum separation for recoil ions as a tool to separate ionization and true capture events, which will be discussed in the next section.

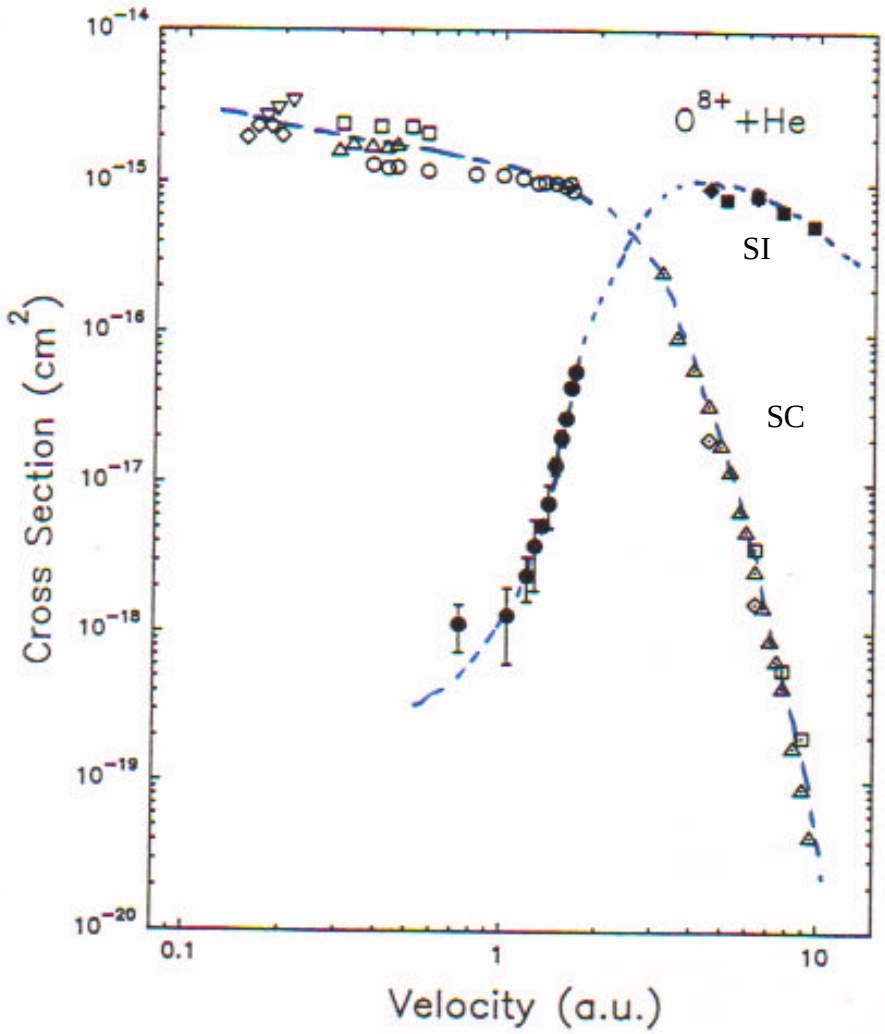

Fig. 2.1 Single ionization (SI) and single capture (total single projectile charge change, i.e., SC+TI, at lower velocities) cross sections for O^{8+} on He. The symbols are: ■ SI, Ref. [37] ◆ SI, Ref. [38] ◇ SC+TI, Ref.[39] ● SI, Ref. [36] ⟐ SC, Ref. [38] ⊡ SC, Ref. [40] ○ SC, Ref. [36] ▽ SC+TI, Ref. [41] △ SC+TI, Ref. [42] △ SC, Ref. [43] SC+TI, Ref. [44]. The dashed lines serve as eyeguides to the data.

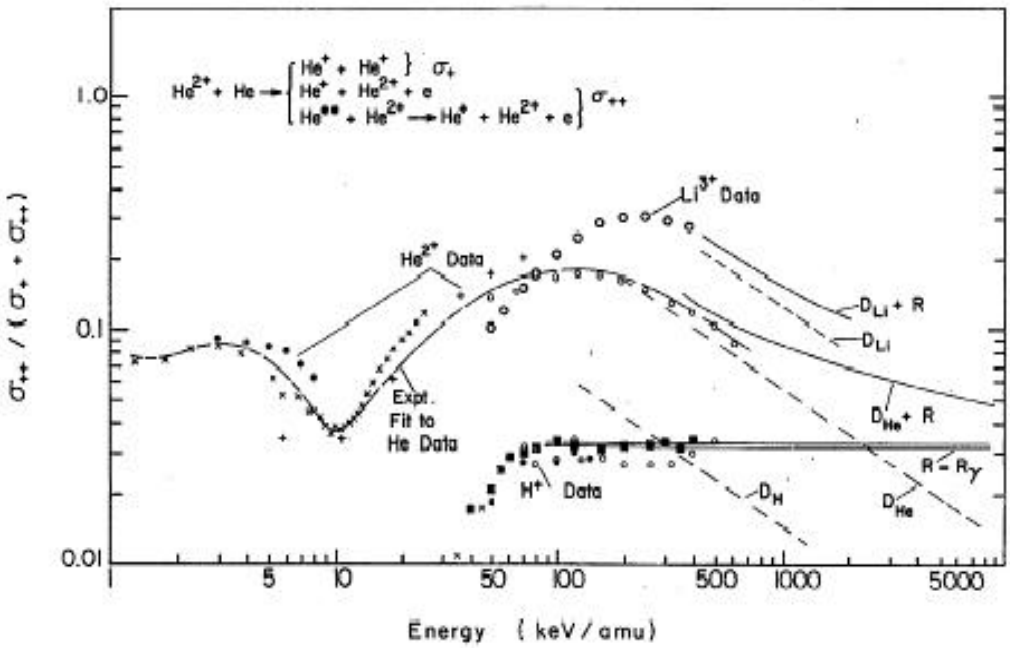

FIG. 2.2. Ratio of cross sections $s^{2+}/\left(s^{+}+s^{2+}\right)$ for capture plus ionization, s^{2+}, to single capture s^{+}, plus capture ionization vs projectile velocity for impact by H^{+}, He^{2+}, and Li^{3+}. $R = R_g$ is the ratio of single-to-double ionization by photons. R represents the rearrangement mechanism. Symbols for data: ?, J. H. McGuire *et al*.[Ref. 47]; ?, Horsdal-Pedersen and Larsen [Ref. 45]; o, Shah and Gilbody [Ref. 46]; x, Afrosimov *et al*. [Refs. 52-54]; +, DuBois [Ref. 55]. Transfer ionization, i.e., double capture to excited states followed by autoionizing action, important at the lower velocities, is included.

FIG. 2.3 Ratio of the cross sections of transfer ionization and single capture for 2 MeV/u projectile ions incident on He. Symbols for data: solid squares, $Cl^{7+,\ 9+}$ inverted triangles, $Cl^{13+,\ 14+,\ 15+}$ and solid lozenges, $Ti^{15+,\ 18+}$, Montenegro *et al*. [Ref. 50]; solid circles O^{7+} and triangles $F^{7+,\ 8+}$, J. L. Shinpaugh *et al*. [Ref. 38]; x, 1 MeV/u $U^{27+,\ 35+}$ Datz *et al*. [Ref. 49]. Theory: Shingal *et al*.[Ref. 51] the thin solid curve labeled $k = 0\%$; the thin solid curve labeled by q^2 is the square law curve relative to the He^{2+} projectile case; the thin solid curves indicated by $k = 13\%$, Montenegro *et al*. [Ref. 50] are model calculations considering 0% and 13% contributions of the excitation channel relative to ionization, at small impact parameters; the open squares (with the dashed curve to guide the eye) are the results of Montenegro *et al*. [Ref. 50] and are model calculations obtained through the excitation to ionization ratio, k, at small impact parameters, given by coupled channel calculations.

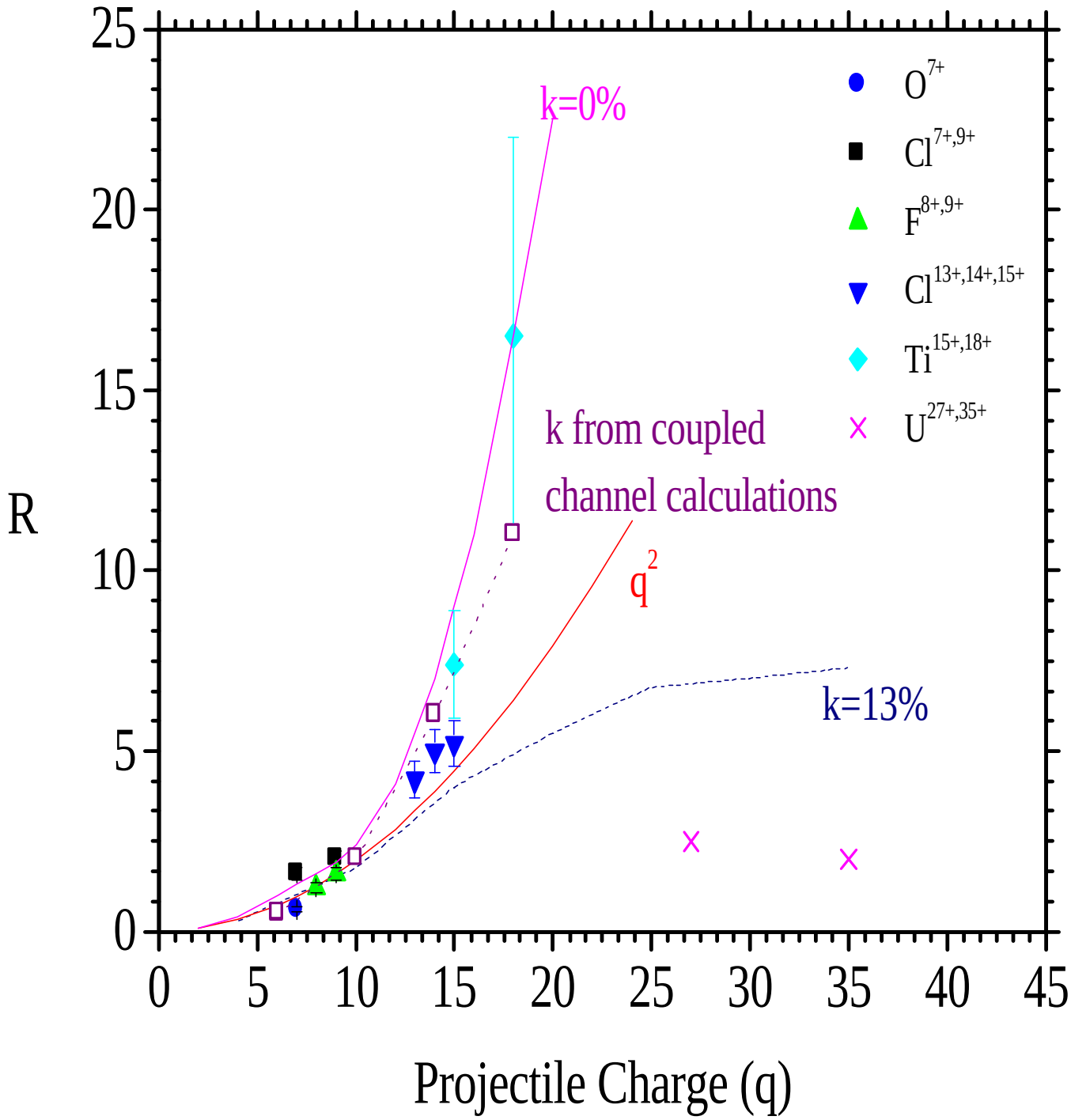
R
Projectile Charge (q)
0
5
10
15
20
25
30
35
40
45
k=0%
k from coupled
channel calculations
q2
k=13%
O7+
Cl7+,9+
F8+,9+
Cl13+,14+,15+
Ti15+,18+
U27+,35+

Transfer Ionization Mechanisms

Several different mechanisms can contribute to the transfer ionization process. In very slow collisions ($\leq 1\,eV/u$) TI can result from autoionization of the quasimolecule formed during the collision.[56] In faster collisions (a few tens of eV/u to several hundreds of keV/u), transfer ionization can be attributed to double capture by the projectile followed by autoionization.[57] L. H. Anderson *et al*.[58] also found evidence that TI can be due to the transfer of two electrons to a highly correlated state of the projectile ion followed by the loss of one of the electrons to the continuum. In the high energy regime ($\geq 1\,MeV/u$), TI is expected to be due mainly to single capture plus direct ionization of the target.

The mechanisms responsible for this non-radiative capture plus ionization process can be grouped into types depending on what compensates the momentum change of the projectile due to the mass transfer by the captured electron (i.e., is it the recoil nucleus, the emitted electrons or a combination of both). Since transfer ionization also requires emitting the second electron to the continuum, it might proceed via relaxation of the target wave function, namely "shake-off", or it may be due to an electron-electron interaction. Another possibility in the second step is a second interaction of the projectile with the target within the independent electron model approximation.

For the purpose of discussion we define four mechanism that have been proposed in the literature as distinct transfer ionization channels

i. Kinematical Capture-Ionization, KC-I TI
ii. Projectile-Electron-Nucleus Thomas, p-e-n Thomas TI
iii. Projectile-Electron-Electron Thomas, p-e-e Thomas TI
iv. Correlated Kinematical Capture TI

i. Kinematical Capture plus Ionization, KC-I TI

KC-I TI is a two-step process with either one or two interactions with the projectile. In the single capture process by KC, electrons whose initial state velocity

closely matches the projectile velocity are captured. The energy and momentum conservation laws dictate that the recoil ion will receive a longitudinal momentum transfer in the backward direction of the projectile ion. This backward momentum transfer is the characteristic signature of the kinematical capture process and is closely related to the Q-value of the reaction. The transverse momentum transfer to the He^+ recoil ion must exactly balance that given to the projectile.

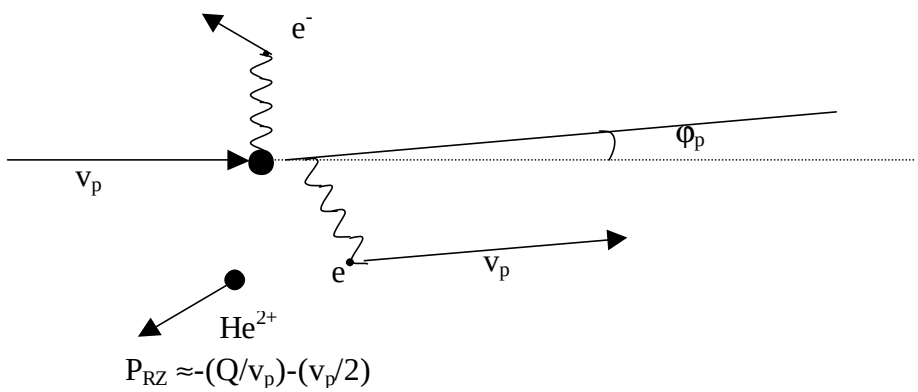

Fig. 2.4 The schematic representation of the kinematical capture and independent ionization that makes the KC-I TI process (via a TS2 or a TS1 process).

In the transfer ionization case, McGuire[59] predicted that the additional ionized electron has a rather small kinetic energy due to either a shake-off process (TS1), two step-one e-n interaction or due to ionization by a second independent interaction between the projectile and the second electron (TS2, two step-one e-n interaction), see Fig 2.4. The projectile direction is taken as the z-axis. Lahmam-Bennani *et al.*[60] have shown that if the continuum electron leaves with small transverse momentum, the transverse momentum of the recoil ion must balance the one received by the projectile; on the other hand, if the continuum electron is ejected by a hard collision between projectile and electron, the recoil ion transverse momentum will be smaller and the projectile transverse

momentum should be balanced primarily with the electron transverse momentum. The KC-I TI is the dominant process leading to TI by high velocity highly charged ions.

ii. p-e-n Thomas TI

The classical scattering processes Thomas[61] described involved a double scattering whereby the nearly free electron is first scattered by the projectile to a laboratory angle of 60^0, for which it attains a velocity equal to that of the projectile, and then is scattered elastically off the target nucleus to redirect this velocity vector in the direction of the projectile. The TI process requires the second electron to be ionized. This is achieved through the shake-off or the independent ionization of the second electron by the projectile as in the KC-I TI process. One characteristic of the shake-off process is that the projectile scattering angle for the KC-I-TI is well defined. For H^+ on He the final H scatters to an angle of 55 mrad.

In the pure electron capture there are only two bodies in the final state therefore the recoil must compensate for momentum change to the projectile and captured electron system. In the TI process either the emitted electron, or the recoil ion, or both share in the momentum transfer from projectile plus captured electron system.

iii. p-e-e Thomas TI

In this classical process, the first electron is hit once by the projectile and is scattered at 45^0 with a velocity equal to the $\sqrt{2}v$ of the projectile as shown in Fig 2.6. It then collides elastically with the other electron to redirect its velocity in the direction of the projectile with a velocity equal to that of the projectile. Since the second electron is ionized, the condition for the TI is satisfied automatically. This process is also known as TS1 (two step-one e-n interaction), which is a two step process with one interaction with the projectile. In this classical picture the second electron is emitted at 90^0 in the laboratory.

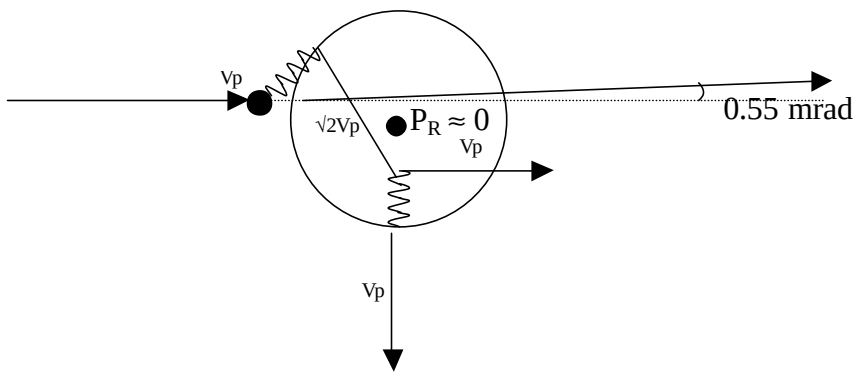

Fig. 2.6. The schematic representation of the e-e Thomas scattering for H^+-He collision.

The p-e-e Thomas scattering creates an opportunity to investigate the dynamic electron electron correlation in atomic collisions. Since the electrons are removed very quickly from the bound state of the target by the p-e-e Thomas scattering, the nucleus will be left behind with its momentum distribution from the initial ground state (no recoil ion momentum). This will lead us to the sum momentum of the two electrons. This p-e-e Thomas scattering process has been reported in the literature by Horsdal-Pederson *et al*.[62] and Palinkas *et al*.[63] Horsdal-Pederson *et al*.[62] have observed significant structures in singly differential cross sections of the TI in proton-helium collisions. They found a peak in the ratio of transfer ionization to total transfer at a scattering angle of about 0.55 mrad at projectile energies of 0.2-0.5 MeV. However, Gayet and Salin[64] could reproduce this peak within the IEM, and Mergel *et al*.[65] experimentally confirmed that this peak is caused mainly by the independent two-step process, which means not by the e-e double scattering. Palinkas *et al.*[63] found a peak in the doubly differential cross section $\frac{d^2 s}{dE_e d\Omega_e}$ at $q_e = 90^0$ and $E_e = 600eV$ at $E_P = 1MeV$. However, Briggs and Taulbjerg[66] reproduced this peak by a second order Brinkman-Kramers approximation (BK2). Later,

Ishihara and McGuire[67] predicted that the Thomas singularity should be located on the ridge at $k = v_P$, where v_p is the projectile velocity. Mergel *et al*.[65] have conducted a kinematically complete experiment on the proton on helium TI process by using COLTRIMS. They have separated the independent two-step process and the p-e-e Thomas scattering in the nine-dimensional momentum space of the final state for the first time. Recently, Schmidt *et al*.[68] reported that the p-e-e Thomas scattering contribution to the total TI process is about 35% for the proton on He collision system at very high velocities.

iv. Correlated Kinematical Capture and Ionization (c-K-TI)

Mergel *et al*.[69] recently have reported about this new TI channel. Their data show strong evidence for this new reaction channel, which they named c-K-TI, mediated by the e-e correlation in the initial momentum wave function. They concluded that only the initial-state correlation can be responsible for this new TI reaction channel. This process remains very speculative at this time.

In summary, Mergel *et al*.[69] have shown that the different TI channels are expected to produce mean recoil momenta centered about the following:

For p-e-e Thomas;

$$(k_x, k_y, k_z) = (0,0,0)$$

For a two-step process with the transverse momentum balanced by the recoil;

$$(k_x, k_y, k_z) = \left[-P_\perp(H^0), 0, -\frac{mv_P}{2} \right]$$

For a two-step process with the transverse momentum balanced by the electron;

$$(k_x, k_y, k_z) = \left[0, 0, -\frac{mv_P}{2} \right]$$

where k_x is to be in the direction of the H^0 transverse momentum $P_\perp(H^0)$, k_y is to be the direction perpendicular to the H^0 scattering plane, and k_z is to be the beam direction.

Motivation for the Present Study

. The cross sections of TI and SC, for the collisions of fast highly charged ions with He, can be written within the IEM using the uncoupled ionization probability,

$P_i(b)$, and capture probability, $P_c(b)$. The probabilities for SI, DI, SC and TI can be expressed in terms these probabilities as

$$\begin{aligned} P_{SI}(b) &= 2P_i(b)(1 - P_i(b) - P_c(b)) \\ P_{DI}(b) &= P_i^2(b) \\ P_{SC}(b) &= 2P_c(b)(1 - P_i(b) - P_c(b)) \\ P_{TI}(b) &= 2P_c(b)P_i(b) \end{aligned} \qquad \text{Eq. 2.1}$$

The cross section for SC and TI can then be written as

$$\begin{aligned} s_{SC} &= 2p\int P_{SC}(b)bdb \\ s_{TI} &= 2p\int P_{TI}(b)bdb \end{aligned} \qquad \text{Eq. 2.2}$$

Substitution of Eq. 2.1 into Eq. 2.2 yields

$$\begin{aligned} s_{SC} &= 2p\int 2P_C(b)(1-P_i(b)-P_C(b))bdb \\ s_{TI} &= 2p\int 2P_C(b)P_i(b)bdb \end{aligned} \qquad \text{Eq. 2.3}$$

One characteristic of these probabilities is that $P_i(b)$ is approximately constant over the range of b where $P_c(b)$ is non-zero. This leads to the following result

$$\begin{aligned} R = \frac{s_{TI}}{s_{SC}} &= \frac{2p\cdot 2P_i(b)\int P_C(b)bdb}{2p\cdot 2(1-P_i(b)-P_C(b))\int P_C(b)bdb} \\ &\approx \frac{P_i(b)(smallb)}{1-P_i(b)-P_C(b)} \end{aligned} \qquad \text{Eq. 2.4}$$

Two center atomic orbital, TCAO, close coupling calculations of $P_i(b)$ and $P_C(b)$ by Tseng and Lin (private communication) for 1 MeV/u F^{9+} on He are presented in Fig. 2.7. In this calculation, they use the independent electron model. In their model for He each electron is assumed to be in an effective Coulomb potential, $V = -\frac{Z_{eff}}{r}$, with an effective charge, $Z_{eff} = 1.7$, such that the binding energy of each electron is half of the

double ionization energy of He. Also, they employed a basis set consisting of 40 atomic states (s, p, d and f) on the projectile ($F^{(9-8)+}$) and 103 atomic states (s, p, d and f) on the target (He^{+}) are used to study the collisions between the projectiles on He for impact energies of 1, 1.25, 1.5 and 2.0 MeV/u. They included some bound and positive energy pseudostates in addition to the exact n=1-5 states of He^{+} in their basis set.

We see from these plots that P_i is indeed approximately constant over the impact parameter range, where the capture cross section is non-zero as assumed in obtaining Eq. 2.4. If we consider the value P_i~0.7 as given in Fig. 2.7 and use Eq. 2.4, one can easily calculate the ratio to be R = 2.5. The ratio obtained by this method is in close agreement with the full calculation R=2.59 that will be presented later [Table 4.2 and Fig. 4.6].

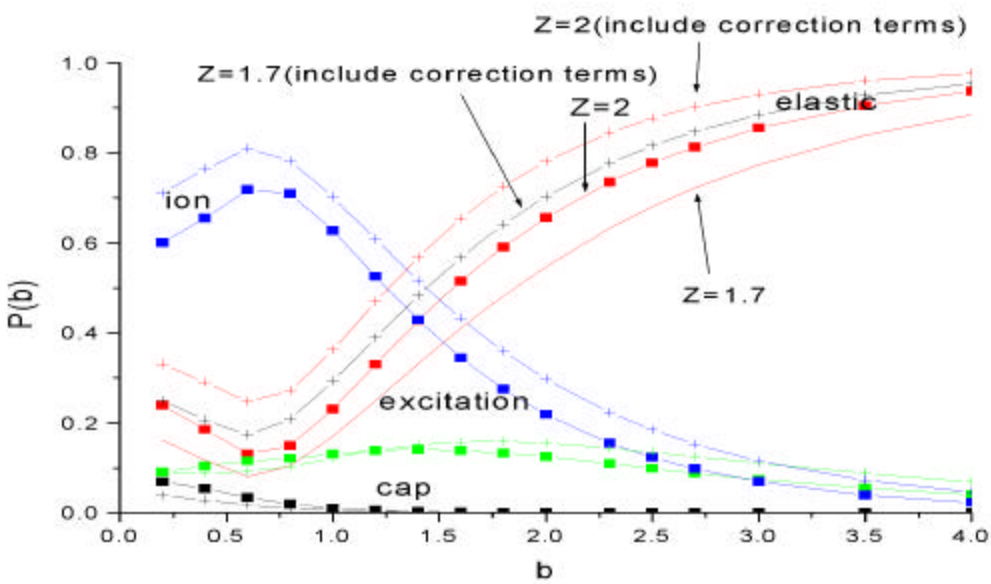

Fig. 2.7. Comparison of probabilities with respect to impact parameters for different channels with different effective potentials at 1MeV. Figure is provided by Tseng and Lin (private communication).

The value of $P_i(b)$ scales as the square of the projectile charge (i.e. q^2) in first order perturbation calculations. It is therefore expected from Eq. 2.4 that the ratio is R~ q^2. The TI/SC ratio for 1 MeV/u He^{2+} + He is measured[44,45] to be 0.11. The q^2 scaling then predicts the ratio for 1 MeV/u F^{9+} + He to be 2.23 which agrees with the result of 2.5 obtained above. Therefore even with $P_i(b)$ values as large as ~0.7 as in the F^{9+} case the q^2 dependence seems to hold. For larger values of q, the approximation $P_I \sim q^2$ breaks down

because the collision goes outside of the scope of the perturbative regime. One can easily imagine that $P_i(b)$ saturates at 1 for these larger values of q. This study aims to find out experimentally what this dependence is going to be. Moreover, the TI/SC ratio is not fully understood for q= 15-30. The only data available in this region are not conclusive because of large error bars associated with it.

The understanding of collisions with bare projectiles is essential to proceed towards dressed projectiles. However, we cannot use the collision information from bare projectiles indiscriminately to predict the behavior of the dressed projectile. In this study, a systematic study of both charge and energy dependence of dressed and undressed projectiles will be conducted. Finally, we will look into the mechanisms of transfer ionization.

III. EXPERIMENT

J. R. Macdonald Laboratory and the tandem Van de Graaff

All experiments were performed in the J. R. Macdonald Laboratory at the tandem/LINAC facility at Kansas State University. Negative ions were extracted from the cesium-sputter type ion source and injected into the EN 7.5 MV tandem Van de Graaff accelerator. A top view of the laboratory is shown in Fig. 3.1.

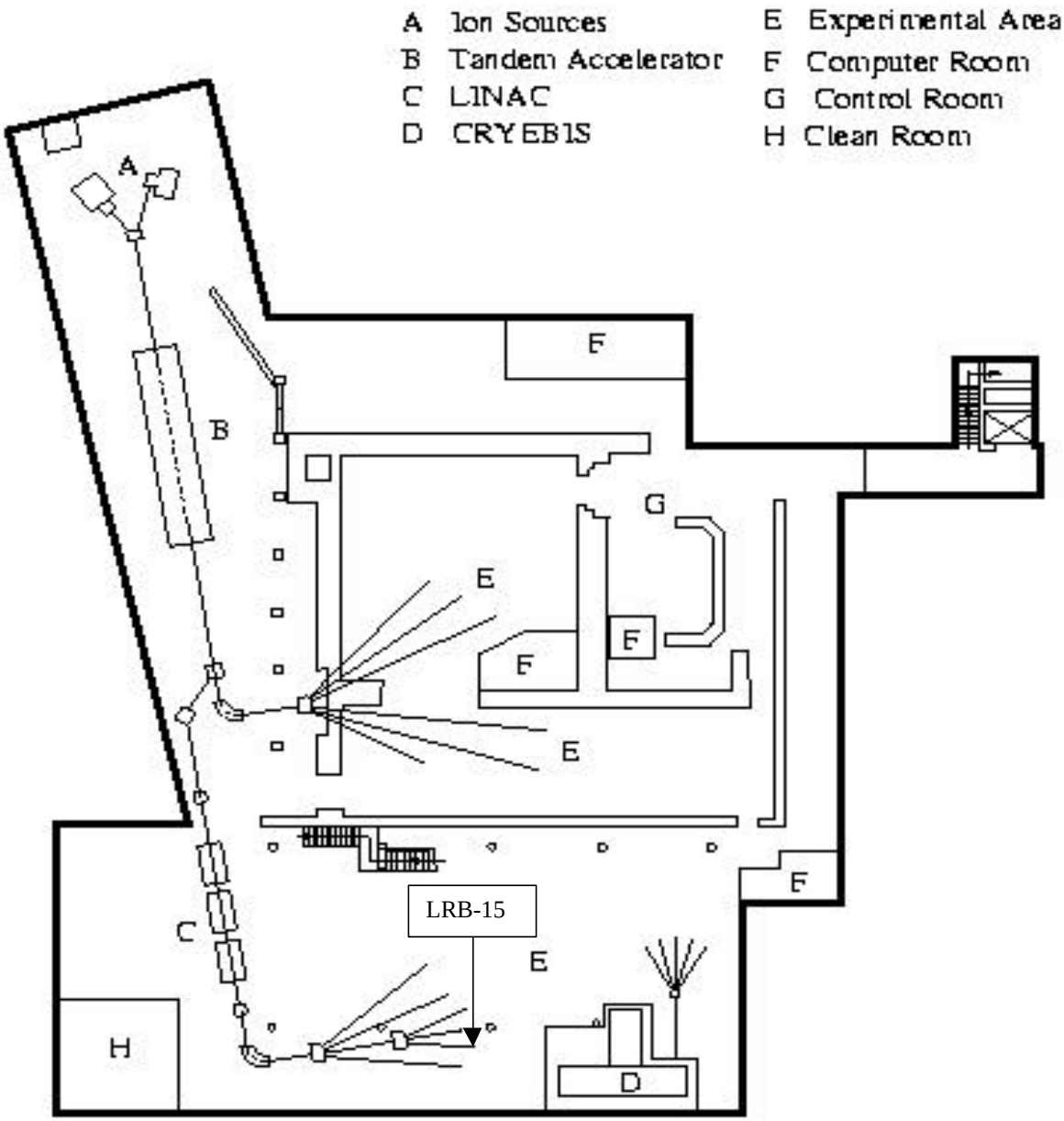

Fig. 3.1. Top view of the J. R. Macdonald Laboratory. The COLTRIMS experimental setup is commissioned at the LRB-15 port.

The tandem accelerator derives its name from the two stages of acceleration that particles travel through in the 35-foot-long evacuated accelerating tube. The terminal is midway along its length and is held at a positive potential up to the maximum voltage. The negatively charged ions injected into the accelerator from the ion source are attracted and are accelerated to the positive potential at the terminal between the first stage and the terminal. At the terminal, the negatively charged ions pass through a gas stripper where electrons are stripped off of the ions. These ions are then repelled and accelerated away from the terminal through the second stage by the positive potential at the terminal. The positive potential at the terminal is maintained by the NEC Pelletron charging system. The Pelletron chains are made of metal pellets connected by insulating nylon links and are charged by an induction scheme that does not use rubbing contacts or corona discharges as shown in Fig. 3.2. There is a chain in both the low energy and high energy columns of the accelerator.

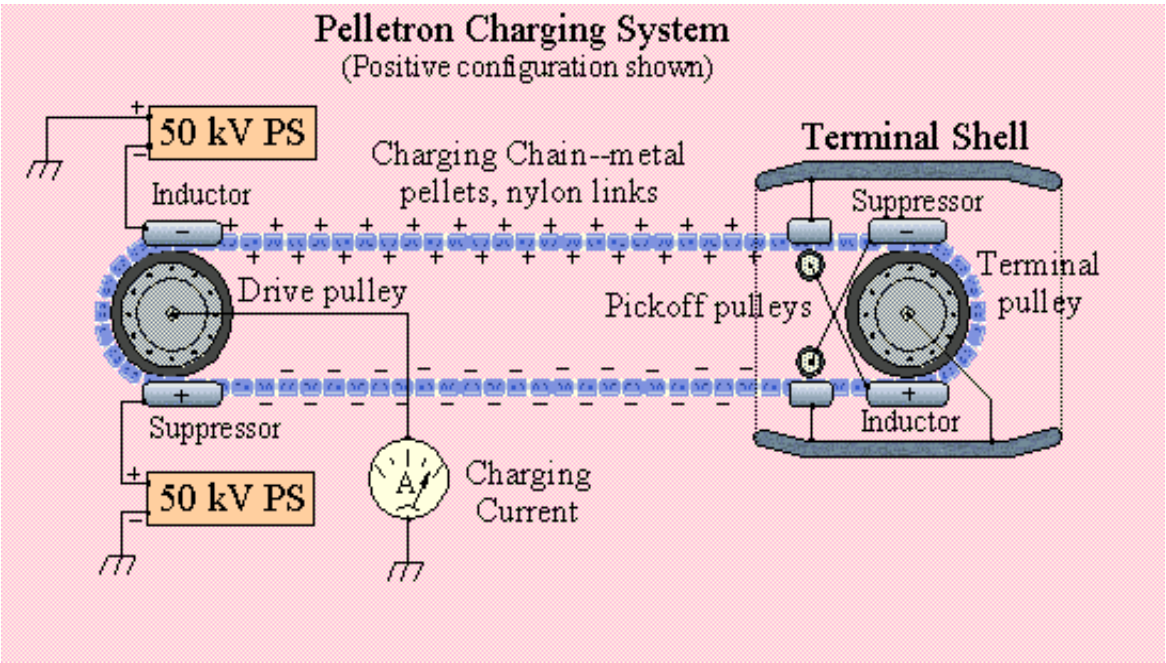

Fig. 3.2. NEC Pelletron Charging System for a positive terminal Pelletron. Pelletron chains are made of metal pellets connected by insulating nylon links and are charged by an induction scheme that does not use rubbing contacts or corona discharges.

For a positive terminal Pelletron, the negatively charged inductor electrode pushes electrons off the pellets while they are in contact with the grounded drive pulley. Since

the pellets are still inside the inductor field as they leave the pulley, they retain a net positive charge. The chain then transports this charge to the high-voltage terminal, where the reverse process occurs. When the charge reaches the terminal, the chain passes through a negatively biased suppressor electrode that prevents arcing as the pellets make contact with the terminal pulley. As the pellets leave the suppressor, the charge flows smoothly onto the terminal pulley, giving the terminal a net positive charge. The chain, accelerating tube, terminal and their support structure are housed inside a large metal tank that is pressurized to 65 p.s.i. with an insulating gas called sulfur hexafluoride. This gas insulates the high voltage at the terminal from surrounding objects. The Pelletron charging system was recently installed in the Van de Graaff, replacing an inferior belt system. The new system has dramatically improved the stability of the ion beam. This stability has greatly influenced our ability to perform experiments, particularly for small beam components. Small intensity beams are very difficult to focus when the intensity fluctuates with time. The new stability is seen in terms of a reduced beam energy spread and in terms of a very stable spacial positioning of the beam.

The ion species of O^{q+} and F^{q+} were accelerated with the tandem. One of the ion species of Si^{q+}, Cl^{q+}, Ti^{q+} or Cu^{q+} emerging from the tandem accelerator was accelerated to a velocity of up to 6% of the speed of light and then passed through the LINAC for further acceleration and steered into the experimental area for use in the experiment.

Superconducting Heavy-Ion Booster Linear Accelerator (LINAC)

The main body of the LINAC consists of 12 niobium split-ring resonators, with a total active accelerating length of 3 meters. Electromagnetic power is fed into the resonators at a frequency of 97 MHz, which causes alternating positive and negative accelerating fields to build up in the structures of the resonators. The average electric field is about 1.8 MV/m, resulting in an equivalent maximum accelerating voltage of 5.4 volts.

Since the accelerating fields inside the resonators are changing as the resonators go through their cycles, particles can be accelerated only at specific times. This requires that the normally continuous flow of positive particles from the tandem accelerator be grouped into equally spaced bunches. The tandem bunched beam arrives at the LINAC with ~2 ns beam pulse width. Two additional LINAC resonators act as bunchers. The first compresses the tandem beam to fit the LINAC's acceptance. A typical time width for an injected beam is around 150 picoseconds. The bunching resonator is the last in the lattice and is used to tailor the beam characteristics for delivery to the target.

Because of the alternating positive and negative accelerating fields in the resonators, the LINAC can be used to both accelerate and decelerate particles. In some of our experiments we used the LINAC in an "accel" mode. The LINAC can accelerate particles to velocities near 15% of the speed of light.

In our case, the ions were momentum analyzed by the first forty-five degree magnet to select the desired energy and ion species of the most abundant charge state beam. It is obtained by post-stripping in a $6\,mg/cm^2$ carbon foil and is momentum and charge analyzed by the second forty-five degree magnet. The ions were either accelerated or just passed through the LINAC and stripped, if necessary just before the 90^0 bending magnet. The ion species were momentum analyzed by the ninety-degree magnet and passed through the first switching magnet. A second switching magnet then deflected related ion species with desired charge state to the experimental region (LRB-15). See Fig. 3.1.

Experimental Setup

The collision chamber is commissioned on the 15-degree port of the second switching magnet, which allows the delivery of a beam with very little impurity as shown in Fig. 3.3. The ion beam is monitored with two beam profile monitors and Faraday cups along its path. Monitoring the beam before and after the chamber was especially useful in determining its passage through the jet. The ion beam is well defined by two four-jaw slits (one before and one after the chamber) and three apertures where one (5 mm) is

before the chamber and the other two are after the chamber (5 and 3 mm). The charge exchange beam is selected with a dipole magnet after the collision chamber.

Fig. 3.3. Schematic diagram of the experimental apparatus. The beam was collimated by two sets of 4-jaw slits, one before (not shown in the figure) and the other one after the second switching magnet separated by approximately two meters and at an angle of 15^0. The beam was bent in the direction of the experiment region with a switching magnet that acted also as a “clean-up” magnet to deflect contaminant ions from the beam, and then through two 5mm circular apertures, one before and one after the collision chamber. Also, the beam profile monitor was used to diagnose the beam and to make necessary adjustments in beam transmission.

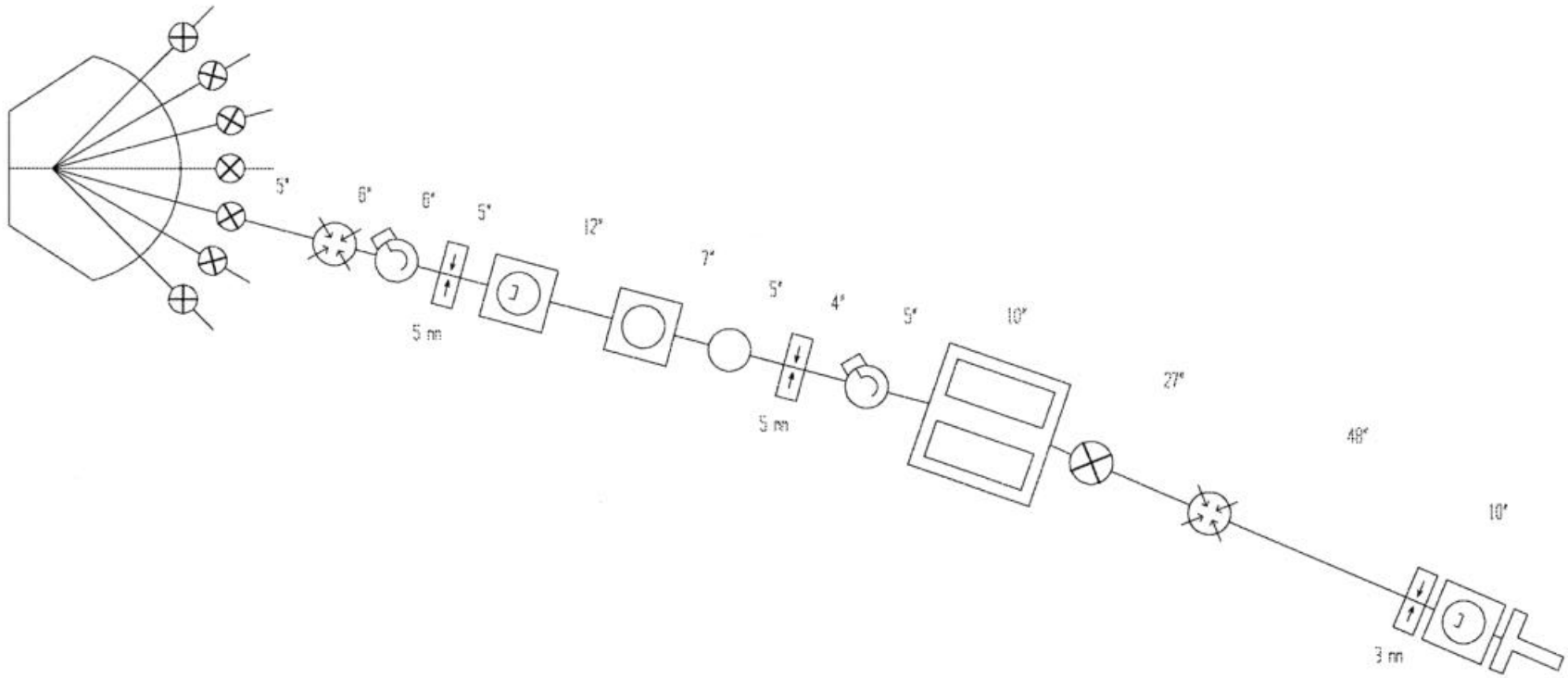
5"
6"
6"
5"
12"
7"
5"
4"
5"
10"
27"
48"
10"
5 mm
5 mm
3 mm

The target was provided using a supersonic He jet with a two-stage collimation as shown in Fig. 3.4.

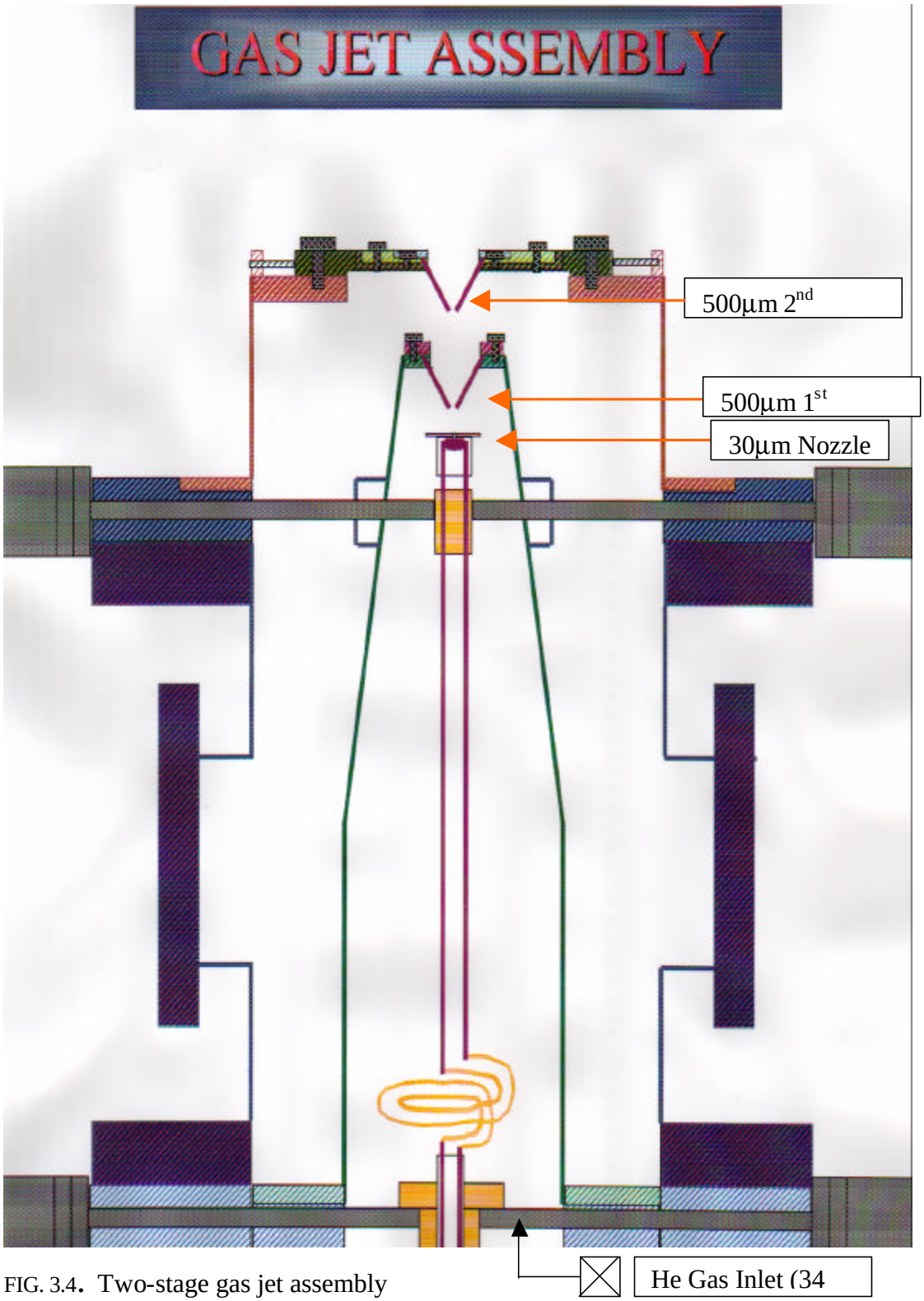

FIG. 3.4. Two-stage gas jet assembly

In our supersonic he jet the nozzle is located 6 mm from the tip of the first skimmer, and the distance between the tip of the second skimmer and the top of the first skimmer is 17 mm. The position of the first skimmer is fixed. The alignment of the 30μm aperture in the nozzle with respect to the first 500μm skimmer is done using two sets of micrometers. The position of the second 500μm skimmer can be adjusted with the set of four screws. The assembly allows one to laser-align the nozzle and the two skimmer apertures as a unit before mounting takes place on the target chamber. The alignment of the assembly was initially tested using nitrogen gas. It was found that the optimum flow of the gas was obtained at a gauge pressure of 15 lb/in^2. Above that pressure the properties of the jet appeared to be destroyed in that a Styrofoam ball placed above the second skimmer no longer reacted to the gas flow. The optimum pressure for He gas was found to be 28 lb/in^2. However, in vacuum the jet is found to behave differently. It appears that even at a pressure of 55 lb/in^2 the jet behaves properly in that the rise in catcher pressure is linear with the increase in the driving pressure (gauge pressure on the gas bottle). The two-stage, geometrically-cooled, supersonic He jet has a significantly reduced background contribution to the spectrum compared to a single stage He jet. In the case of a differentially-pumped gas cell, complex calculations based on assumptions for the correction due to the collisions with the contaminant beam led to corrections, which were up to 50%. The new setup allows one to make direct separation of contaminant processes in the experimental data using the longitudinal momentum spectra. Furthermore, this correction is much smaller (about 8.8%), yielding better overall precision. A measurement of the jet velocity is presented in Appendix A. The jet speed was found to be ~ 1267 m/s.

Spectrometer

Target recoil ions produced in collisions with the projectile were charge-state analyzed using a time-of-flight spectrometer[72] (Fig. 3.5). The recoil ions were extracted by two static-electric field regions, allowed to drift through a field-free region, and detected by a chevron arrangement of two micro-channel plates. Typical channel plate biases were 900 V across each plate. For the recoil side the front of the first channel plate was typically at –1500 V, the front of the second channel plate was at –1000 V and the

back at –100 V. Recoil ion flight times are proportional to the square root of the ratio of the ion mass-to-charge

$$t_R \propto \sqrt{\frac{m_R}{q_R}}$$

where $t_R, m_R,$ and q_R are the recoil ion flight time, recoil ion mass and recoil ion charge, respectively. Typical recoil ion time-of-flight spectra are shown in Figure 3.8.C. It is clear from the spectra that the recoil charge states are separated. The width of each peak is representative of the recoil ion momentum distribution along the field axis, coupled with the width of the beam and the resolution of the time measurement.

The dimensions of the spectrometer were designed to allow for time and spatial focusing of recoil ions produced at different positions in the extraction region due to the width of the beam, which was 2x2 mm at most. The time focusing condition is satisfied when the static electric field-free drift length is twice the length of the electric field acceleration region. The condition for both spatial and time focusing requires the addition of a second electric field region. The appropriate lengths of the electric regions, the drift region and the ratio of the voltages were found by simulations using SIMION. The results are given in Appendix B. Recoil ion flight times were 3.639 and 2.573 μs for He^+ and He^{++} for an extraction voltage of 1500 V on the pusher plate and 852 V on the focusing plate. These plates set up fields of 66.4 V/cm and 232.8 V/cm.

Calculation of the TOF

The time-of-flight of the recoil ions were calculated from

$$t = Cal.Const \times [TOF - T_0]$$

where T_0 is the channel number for time-of-flight equal to zero, TOF is the time-of-flight of the recoils in unit channels and Cal.Const is a calibration constant in nanoseconds per channel.

The calibration constant was obtained by using the master clock from the LINAC.

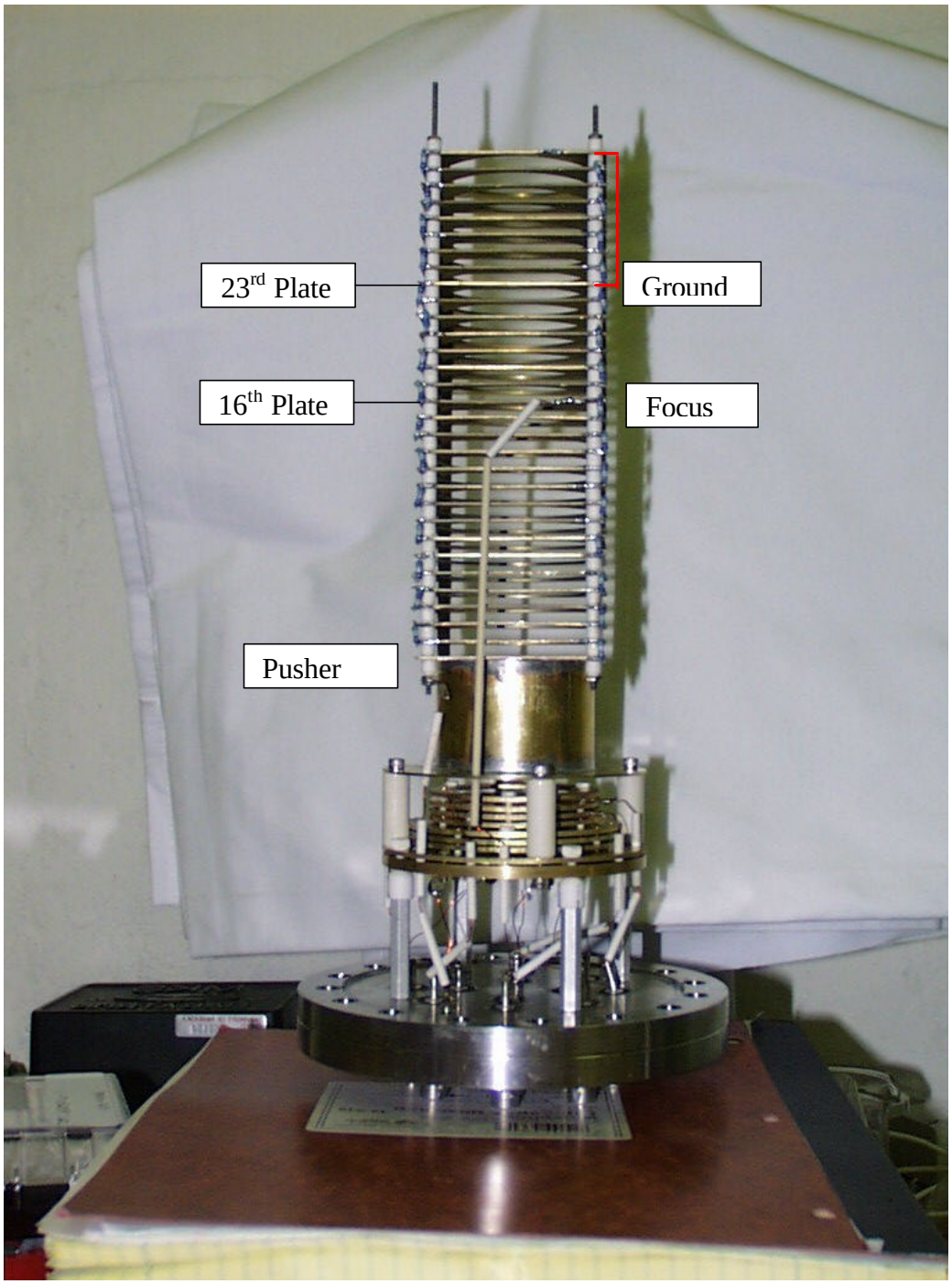

FIG. 3.5. 2-D Detector (e-side) and spectrometer.

Recoil Ion Momentum Spectroscopy technique was used to separate each collision channel by projectile-recoil ion coincidence and to reconstruct all three components of the recoil momentum.

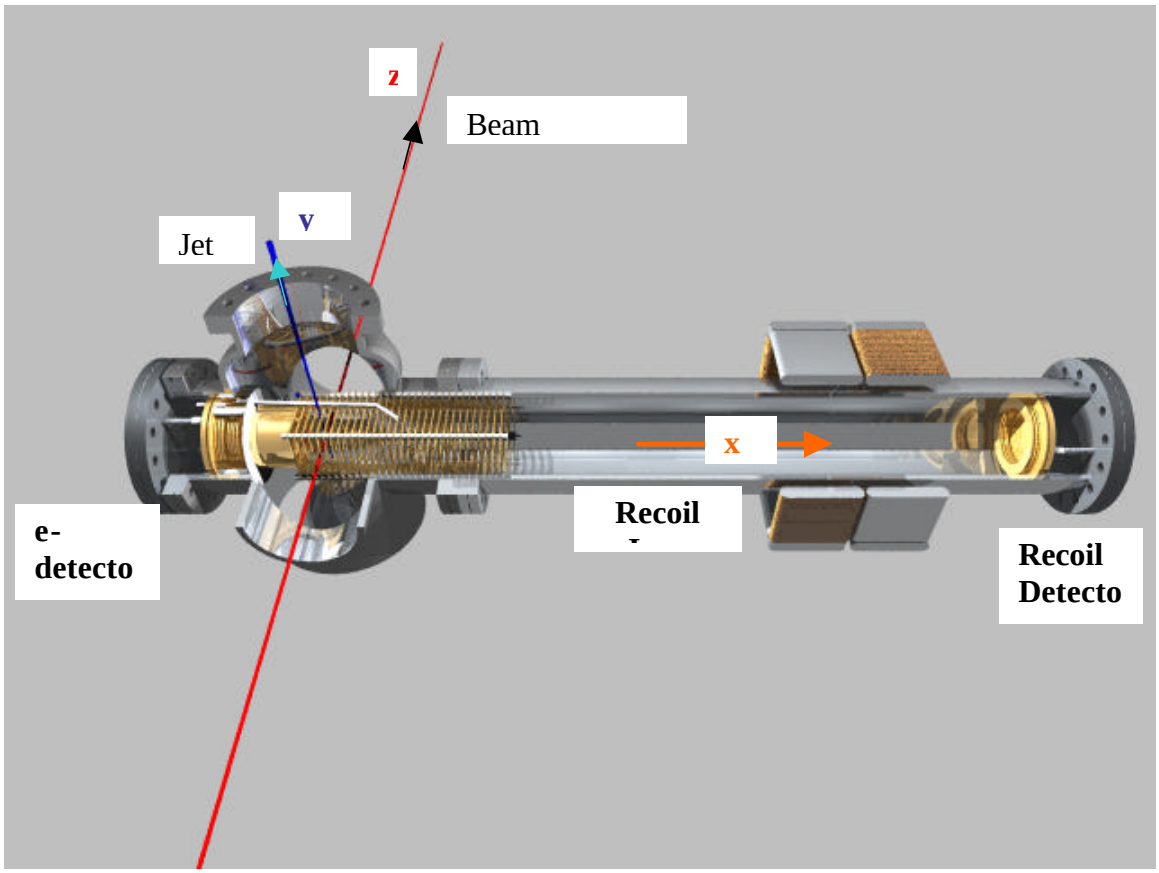

Fig. 3.6. POVRAY image of experimental setup.

Fig. 3.6 shows part of the experimental setup with a cut from the top. The strength of the recoil extraction field was set high enough to ensure that all recoil ions are extracted by the field and collected by the recoil detector. The recoil charge states were determined by measuring the time-of-flight difference between recoil ions and charge-exchanged projectile ions.

Recoil detector

A backgammon anode detector was used in the experiment to detect recoil ions. The backgammon detector has three output channels X, Y and R. However, there is signal coupling between different output channels. In the data-taking process, the three position signals x', y', r' from the backgammon board (PSD) were first corrected for the offset in channel and then multiplied by the decoupling matrix D to get three uncoupled signals x, y, r:

$$(x, y, r)^T = D \cdot (x', y', r')^T$$

where the matrix D is found to be:

$$D = \begin{bmatrix} 1.0 & 0.007437 & -0.088410 \\ 0.007717 & 1.00471 & -0.09050 \\ -0.09175 & -0.09050 & 1.07598 \end{bmatrix}$$

The recoil position x_R, y_R was then calculated by

$$x_R = \frac{x}{x + y + br} \cdot ch_{tot}$$

$$y_R = \frac{y}{x + y + br} \cdot ch_{tot}$$

b was taken to be one. The value for ch_{tot} was 256 channels.

Also, at this point it needs to be mentioned that the last set of data for I^{q+}- ion beams was taken with a resistive anode detector, and at the time of the writing of this dissertation the resistive anode has not been completely characterized.

Electronics

Fig. 3.7 shows the electronics setup for the experiment. The three position signals from the backgammon board (recoil) were first amplified by CATSA pre-amplifiers and further amplified and pulse-shaped and then sent to an analog-to-digital converter (ADC). The timing signals were taken from the back side of the second channelplate of the recoil detector and from the photo-multiplier tube. The timing signals were amplified, sent through the constant fraction discriminators, and input into a time-to-amplitude converter (TAC). The time difference between the recoils and the charge-changed projectiles was measured by the time-to-amplitude converter (TAC) and sent to the ADC. The typical TOF for the recoil ions was between one and five microseconds. The TAC was started with a projectile timing signal and stopped by the recoil-timing signal. The position signals and the TAC signals were digitized by the ADC and sent to the computer for analysis. The ADC strobe signal was taken from the projectile timing signal. The electron side of the detector was not used in the present experiments.

The data were taken on a DEC Micro-VAX computer using a CAMAC interface and stored on a removable 9 GB hard disk. All the data were taken in event mode with an XSYS data acquisition and analysis package. Later, the data were analyzed off line.

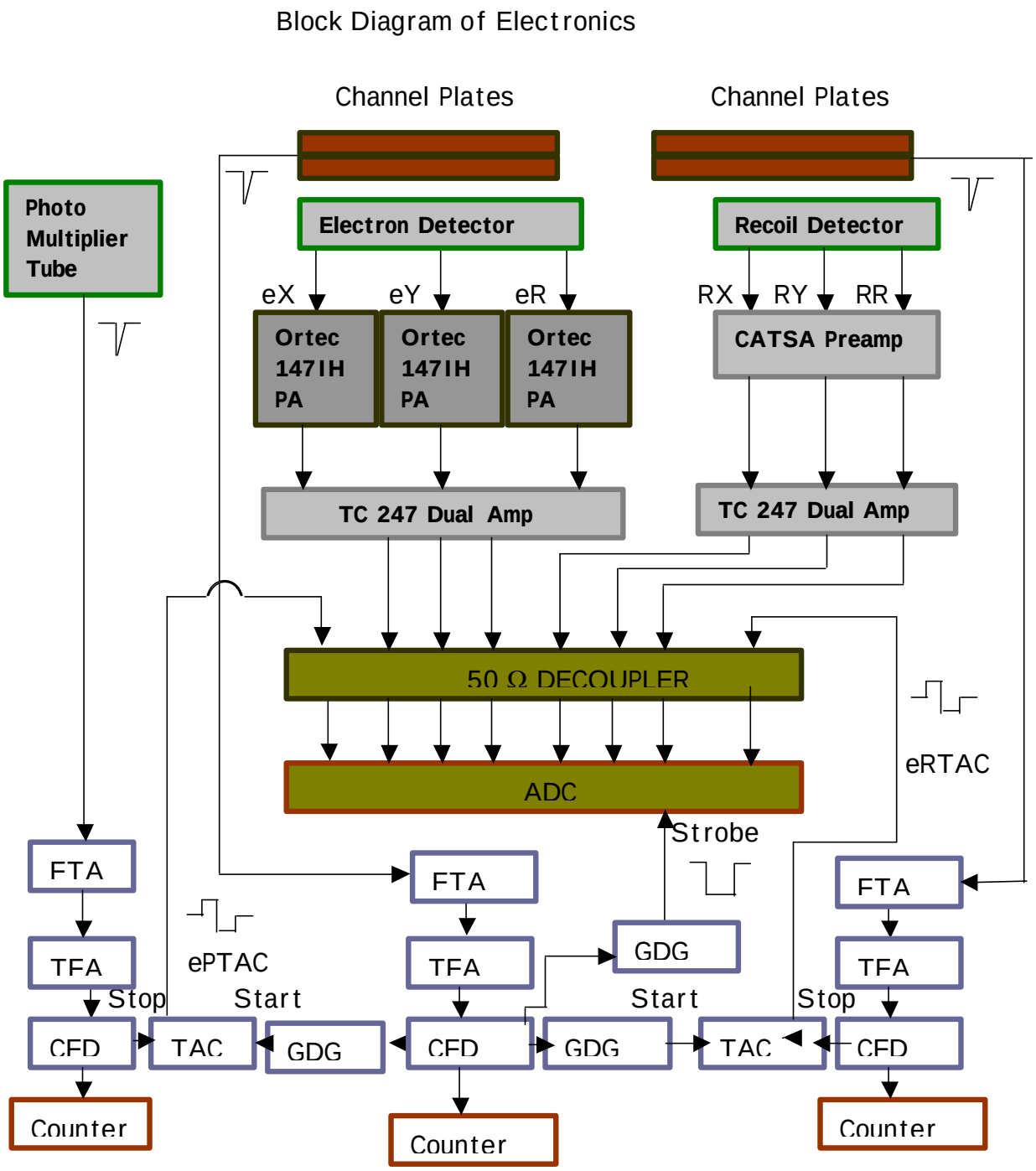

Fig. 3.7. The abbreviations used above should be read as: Amp: amplifier, FTA: Fast Timing Amplifier, TFA: Time Filter Amplifier, CFD: Constant Fraction Discriminator, TAC: Time-to-Amplitude Converter, GDG: Gate and Delay Generator, ADC: Analog-to-Digital Converter.

Data Collection and Analysis

All the data were taken in event mode with the JRML XSYS data acquisition and analysis package. Later, the data were analyzed off line. The data collection process can be separated into two stages: with the LINAC and without the LINAC. The low Z data were collected without the LINAC. The spectrometer pusher and focus voltage were set to 1500 V and 852 V, respectively. Figure 3.8 shows the 2 MeV/u F^{5+} on He case as it was accumulated in the computer. The figure is a direct printout from the display screen. Figure 3.8.D is a density plot of all events: the horizontal axis is the z-component of the recoil ion position (parallel to beam, beam is traveling right to left), the vertical axis is the y-component (jet direction) of the recoil ion position in terms of channel numbers, and the x-axis denotes the number of counts. The TAC is Fig. 3.8.C with two main peaks (He^{++} left and He^{+} right) and other small peaks. The small peaks easily could be identified as different oxygen charge states, which are a signature of the breakup of residual water in the beamline. Then software gates are introduced in the TAC spectra in order to separate the single capture and transfer ionization processes from single ionization. Figure 3.8.A and 3.8.B are the gated spectra on He^{++} and He^{+}, respectively. Figure 3.8.E and 3.8.F are down projections of Figure 3.8.A and 3.8.B. In the analysis of the data, two other software gates are also introduced to subtract the random event contributions from the true capture and the true transfer ionization events, which are shown in Fig. 3.9.B and Fig. 3.10.A. The true single capture events are obtained by subtracting Fig. 3.9.B from Fig. 3.9.A and is shown in Fig. 3.9.F. Then, Fig. 3.9.F is projected down on the z-axis as shown in Fig. 3.9.E and the number of net single capture events are obtained by taking the area under the peak in Fig. 3.9.E. The total number of TI events are obtained by following the similar prescription. Fig. 3.10 displays the results for TI. In all cases, random event contributions were low. We attribute this to a low count rate, good vacuum conditions, extra care given to eliminate contributions from the background, and to well-separated charge-exchanged beams.

The LINAC was used in collecting the high Z data. Fig. 3.11 shows results for Cl^{14+} on He at 1.75 MeV/u. We have discovered a unique opportunity for eliminating most of the single ionization contribution under the He^{2+} peak. The periodic peaks, Fig.3.11, every 81.63 nano-seconds, are created because of using a bunched beam and

can be identified as ionization peaks in the TAC spectra. We have moved the true He^{2+} peak between the periodic peaks, Fig. 3.12, by adjusting the pusher and focus voltage on the spectrometer (these voltages are indicated on the figure). This procedure has eliminated most of contributions from single ionization, as can be seen in the very clean 2D spectrum in Fig. 3.13.

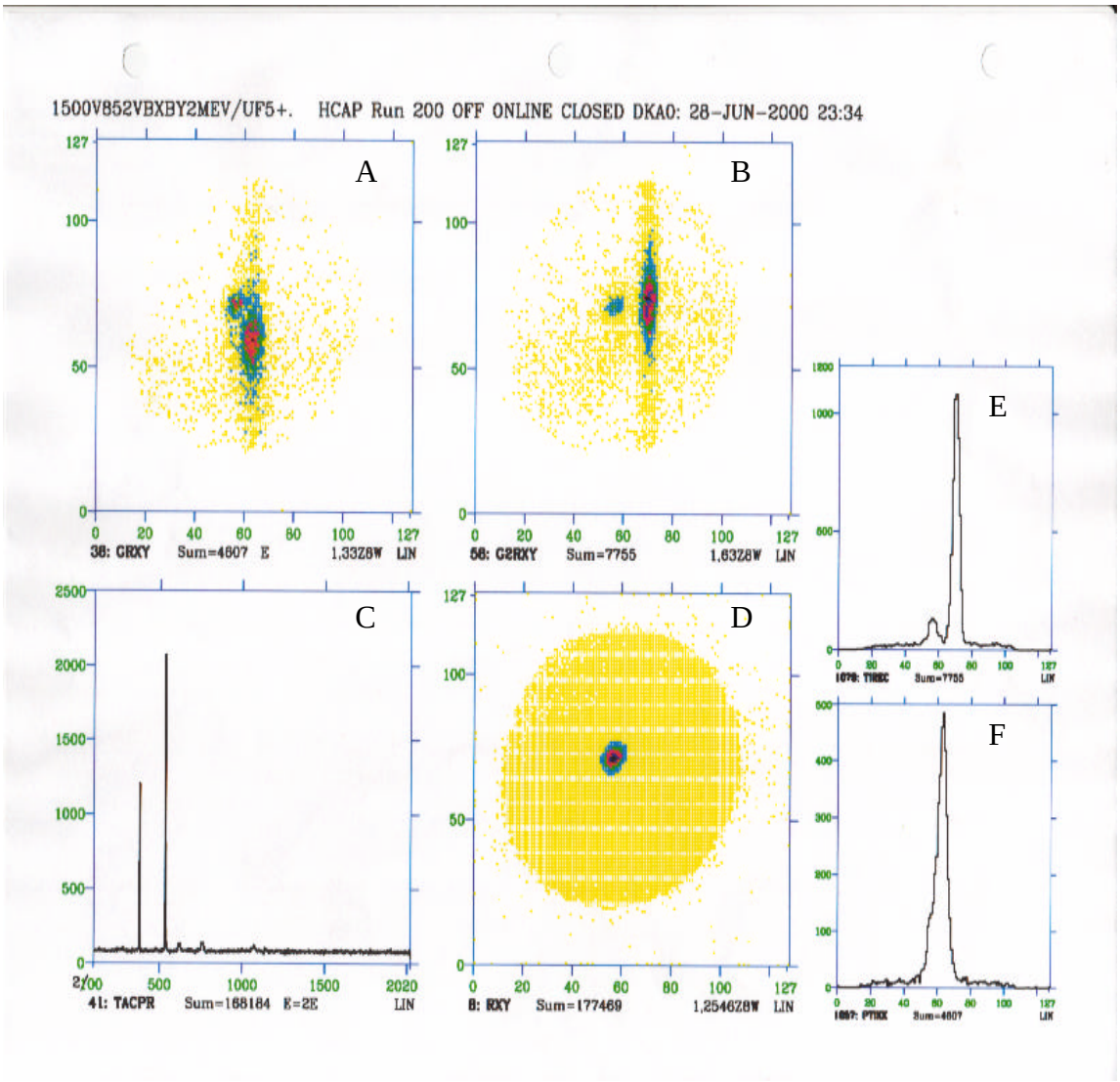

Fig. 3.8. 2.0 MeV/u F^{5+} on He as data were being collected

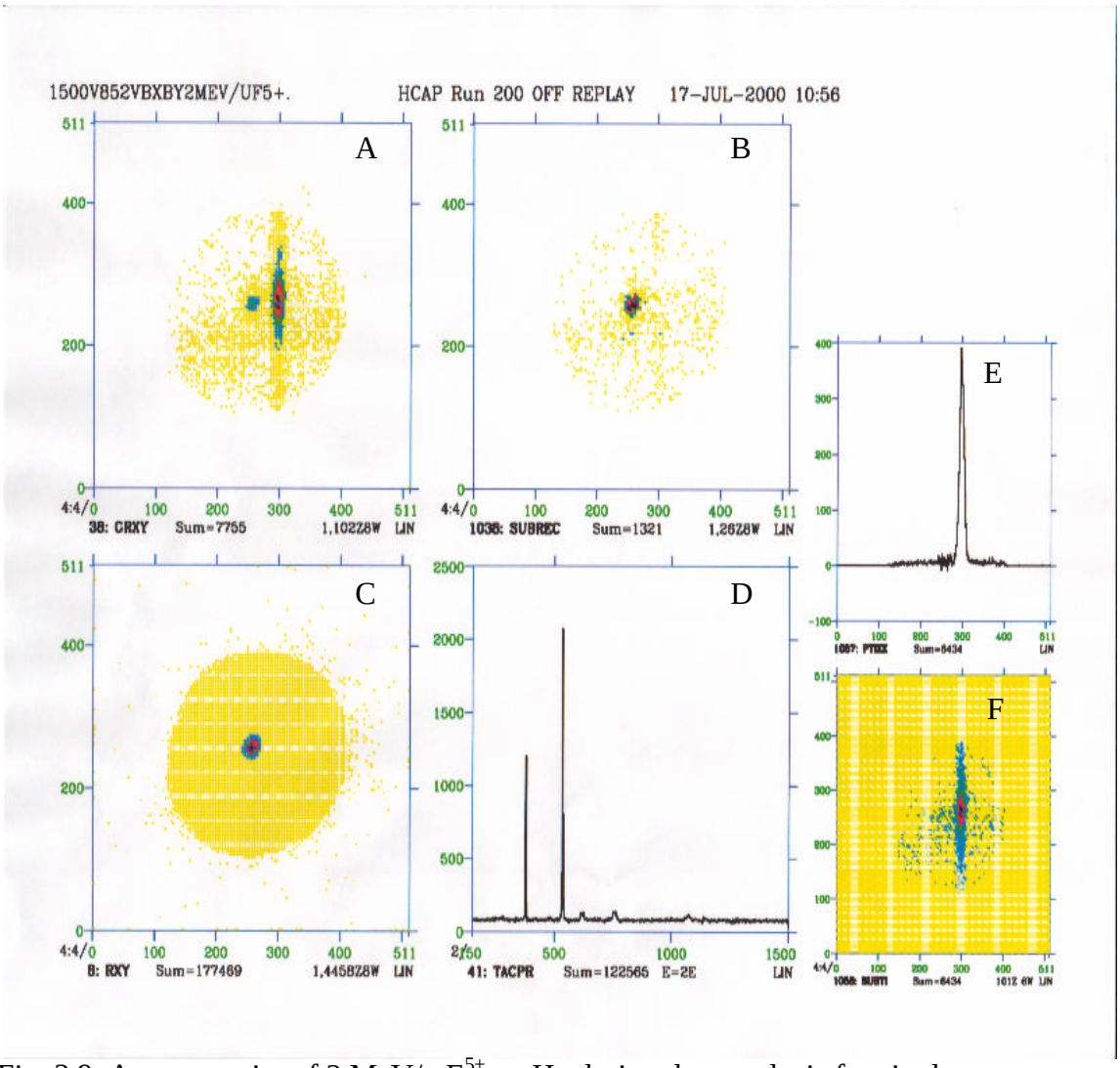

Fig. 3.9. A screen print of 2 MeV/u F^{5+} on He during data analysis for single capture case.

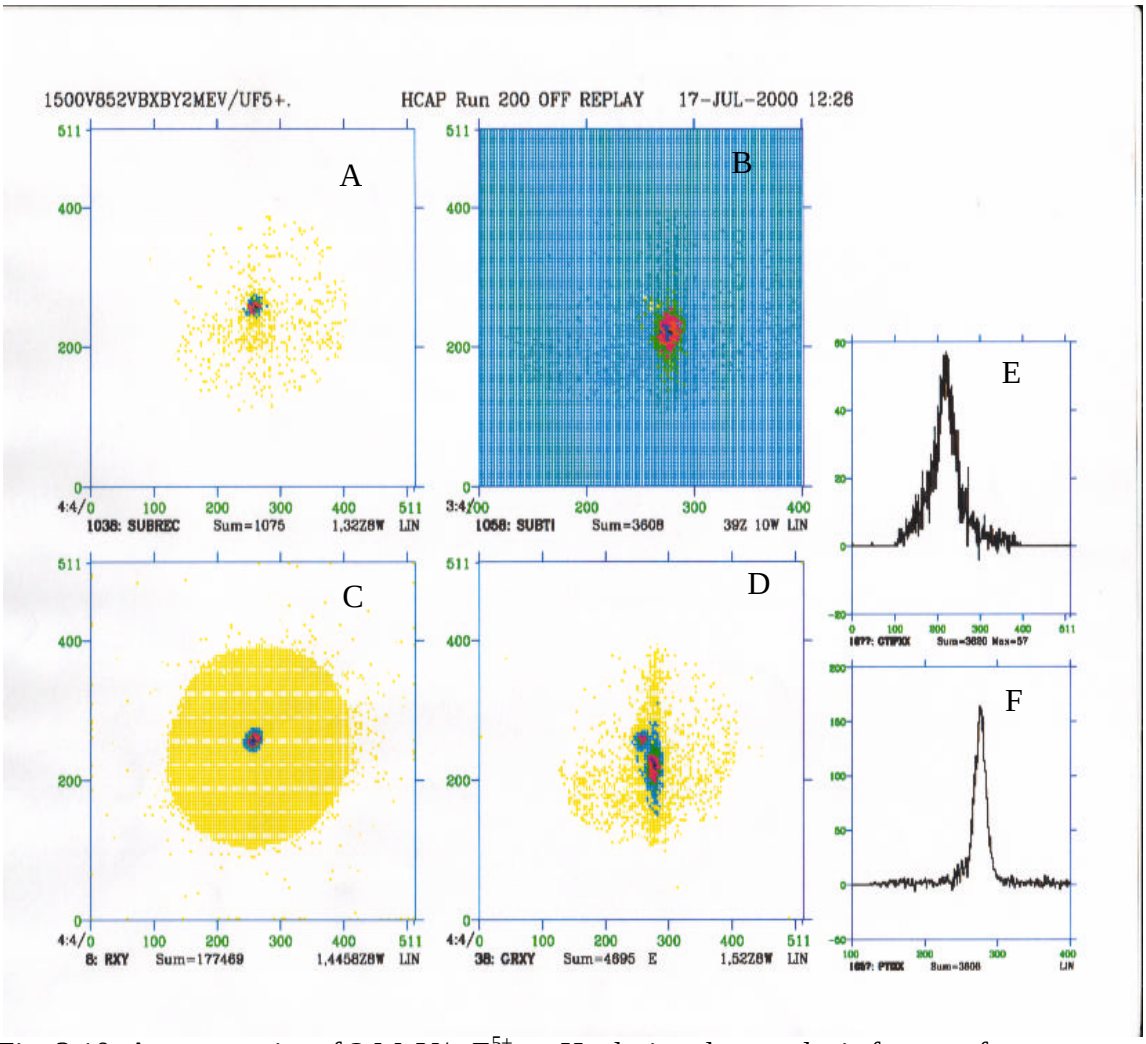

Fig. 3.10. A screen print of 2 MeV/u F^{5+} on He during data analysis for transfer ionization case.

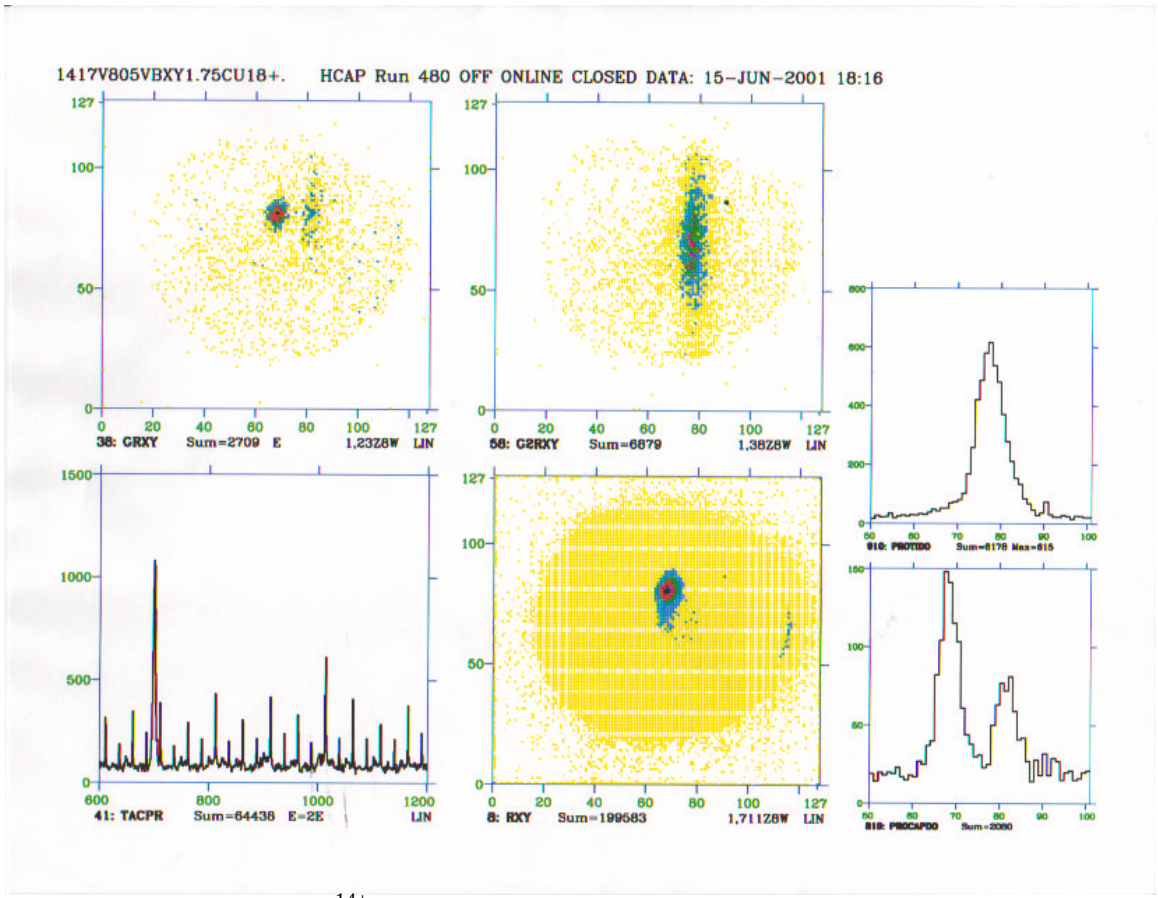

Fig. 3.11. 1.75 MeV/u Cl^{14+} on He as data were being collected.

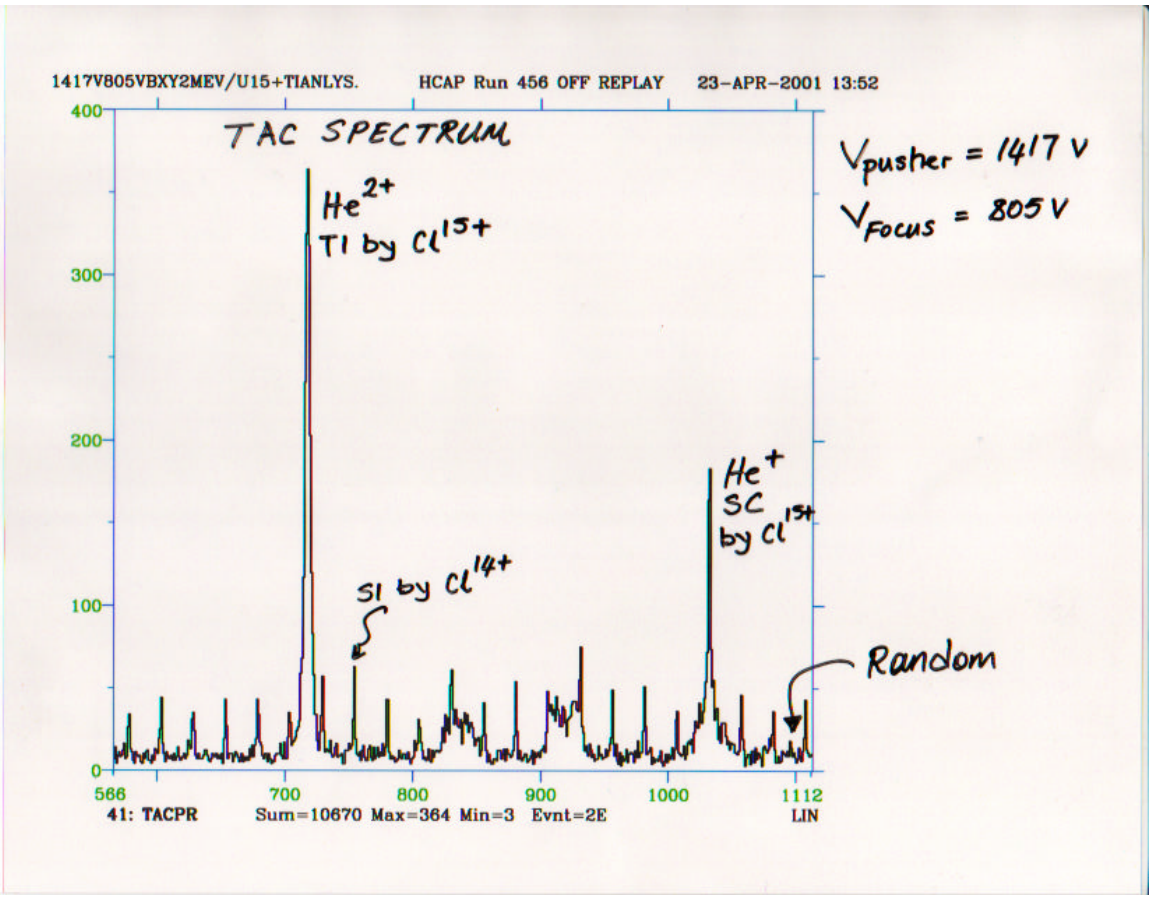

Fig. 3.12. The TAC spectra for 1.75 MeV/u Cl^{14+} on He. The small periodic peaks are the single ionization created by the Cl^{14+} impurity beam. Pusher and focus voltages are adjusted in order that the He^{++} TAC peak is between the periodic ionization peaks.

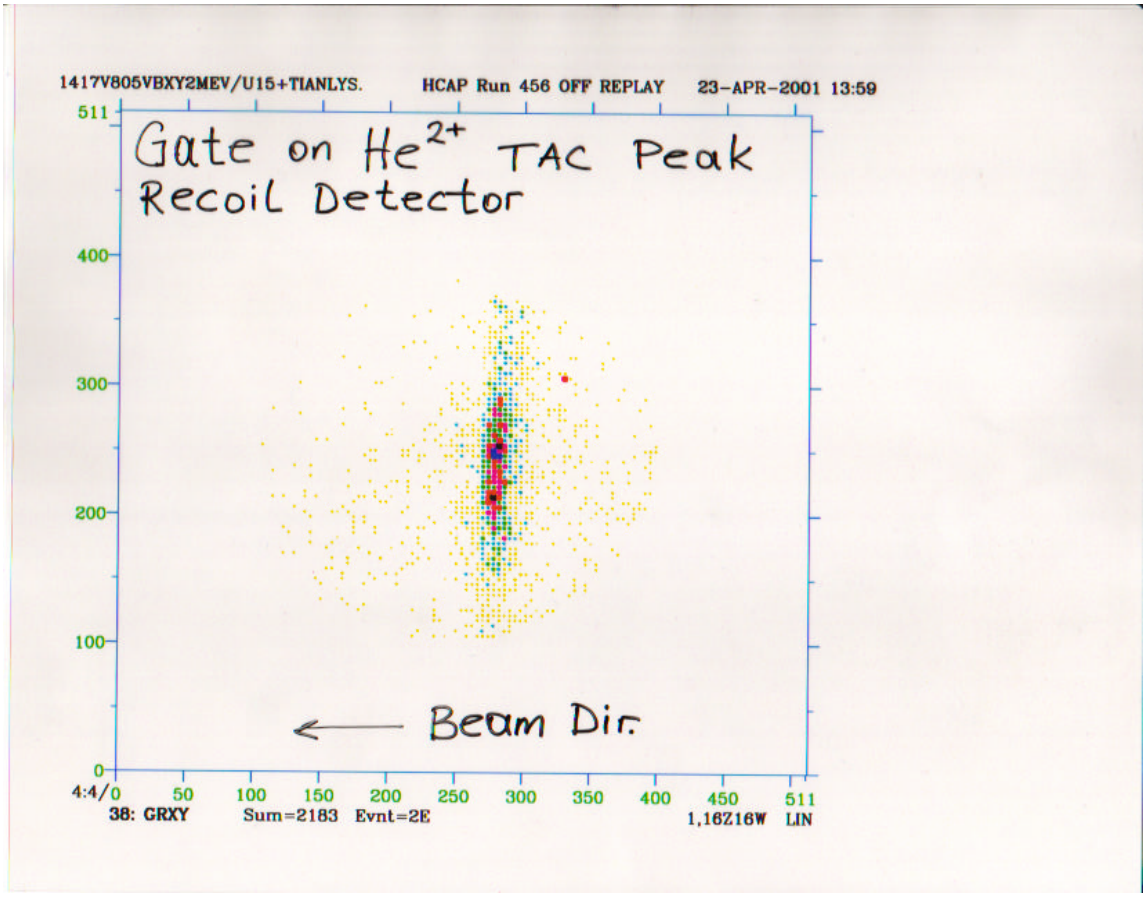

Fig. 3.13. Gate on He^{++} TAC peak as seen on recoil detector. It is evident from the spectra that using the bunched beam and right pusher and focus voltage eliminates the He^{+} ionization contribution.

IV. RESULTS AND DISCUSSION

A. TI and SC in 1 MeV/u O^{q+} + He: A Test Case

Figure 4.1 shows a typical recoil-ion position spectrum of He^+ recoil ions produced by 1 MeV/u O^{5+} ions, which we considered as a test case for our COLTRIMS setup. Spectra are for recoil-ion O^{4+}-projectile coincidences. The beam direction is right to left in the figure. The left-most peak is associated with ionization. The right-most peak is the one corresponding to SC. The lower right figure indicates the longitudinal momentum delivered to the He^+ ions. The scale is converted from the channel numbers to momentum by using the following equation as described in Appendix A.

$$P_z(au) = [Ch - 256.5] \times 0.0981 \qquad \text{Eq. 4.1}$$

The average P_z for SC is ~3 au as can be seen in Fig. 4.1. The relationship between the Q-value and the longitudinal momentum transfer, P_z, is $P_z\ v_p = Q + v_p^2/2$ where v_p is projectile velocity.[27] This equation then predicts that the capture is mainly to n = 3 states of O^{4+}. This means that the capture is from K-shell to M-shell and higher. No K-shell to K-shell capture is observed in this collision system. In H^+- He collision K-shell to K-shell is expected to be the dominating process.

Much higher resolution can be achieved by running the spectrometer at lower voltages. Figure 4.2 shows similar results for the He^{2+} recoil ions in coincidence with O^{4+}, for the same collision system. Coincidences between charge-changed projectiles of appropriate recoil longitudinal momentum yield accurate TI and SC ratios by eliminating contributions from single ionization and double ionization processes from impure beams. Figure 4.3 shows the results measured in our COLTRIMS system for the TI/SC ratio for 1 MeV/u $O^{(4-8)+}$ + He compared with previous results taken from the literature.[38,48] The difference could be attributed to experimental techniques. The small error bars in the present work demonstrate the large improvement in the present set of measurements. The disagreement with the previous data is presumably due to beam contamination, because small beam impurities can be a major source of error in this kind of measurement if not properly separated. Shinpaugh *et al.*[38] have reported two types of correction factors in determining the cross sections for single capture and transfer ionization in the coincidence experiments done with gas cells.

The first type was due to impurities present in the primary beam. Shinpaugh *et al*.[38] found this correction to be as large as fifty percent of the single capture cross section at 38 MeV for F^{9+} on He. The second type of correction originated from double-collision processes and geometrical considerations of the recoil-ion spectrometer and varies inversely with projectile velocity due to the dependence on charge transfer. Shinpaugh *et al*.[38] reported that this correction was as large as 14 percent of the single capture cross section for 13 MeV F^{9+} on He at a target gas pressure of 0.4 mTorr. Since the corrections to the single capture cross sections were larger than those to the transfer ionization cross sections, the determination of the relative cross sections were affected. The ratio of transfer ionization to single capture has larger values than those uncorrected values.

Fig. 4.1. The 2-D recoil ion momentum spectrum of He^{+} ions in coincidence with O^{4+} from 1 MeV/u O^{5+} + He collisions as observed on the position sensitive recoil-ion detector. In the left-most figures the ordinate is the momentum parallel to the beam (longitudinal momentum) and the abscissa is one component of the momentum perpendicular to the beam. The three spectra are for: total coincidences (top), random coincidences (middle) and the true SC coincidences (bottom). The right-most figures are the projections onto the longitudinal direction in a.u.

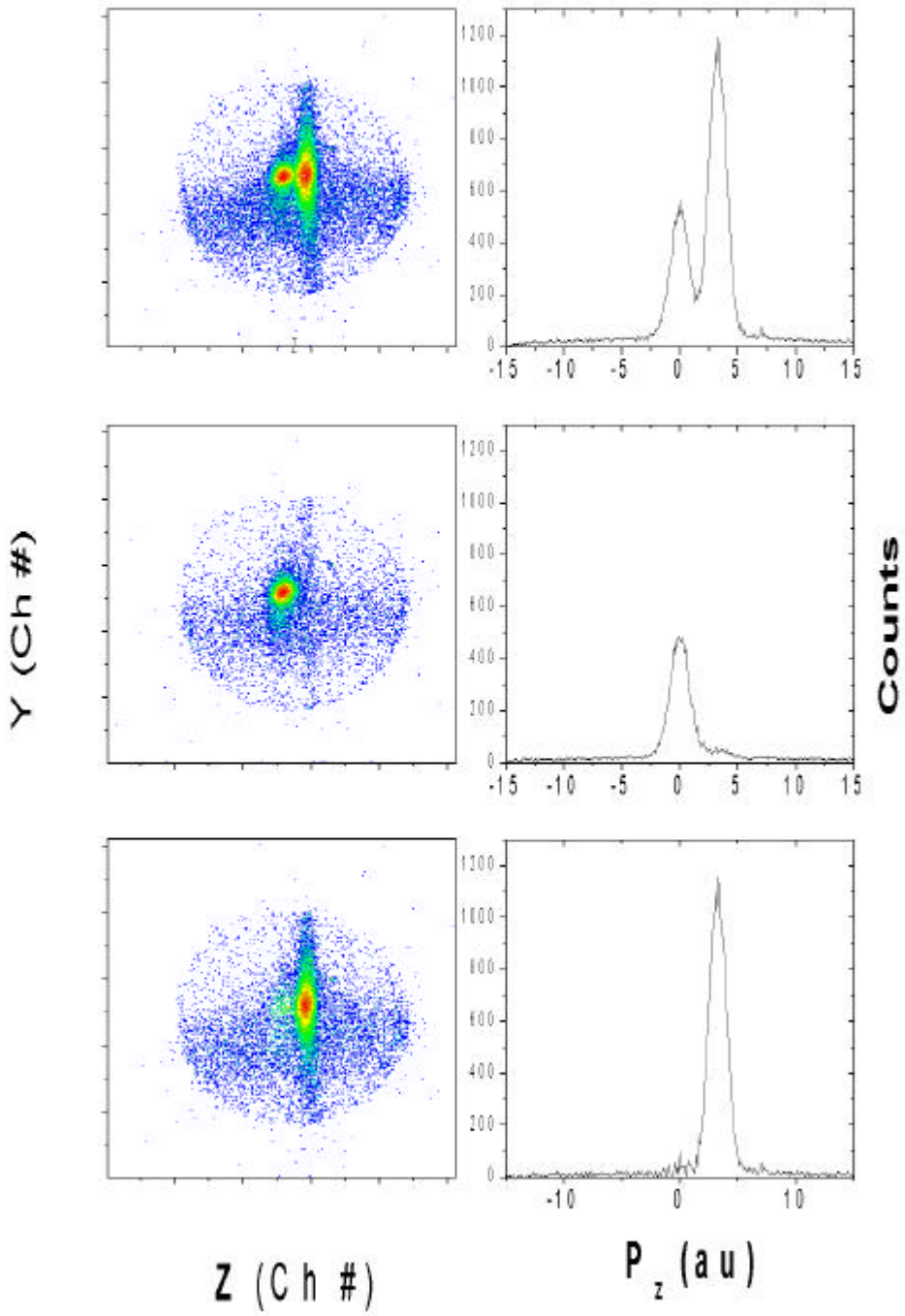
Y (Ch #)
Counts
Z (Ch #)
P z (au)

Fig. 4.2.The 2-D recoil ion momentum spectrum of He^{2+} ions in coincidence with O^{4+} from 1 MeV/u O^{5+} + He collisions as observed on the position sensitive recoil-ion detector. In the left-most figures the ordinate is the position (Ch #) parallel to the beam and the abscissa is one component of the position perpendicular to the beam. The three spectra are for: total coincidences (top), random coincidences (middle) and the true TI coincidences (bottom). The right-most figures are the projections onto the longitudinal direction in Ch #'s.

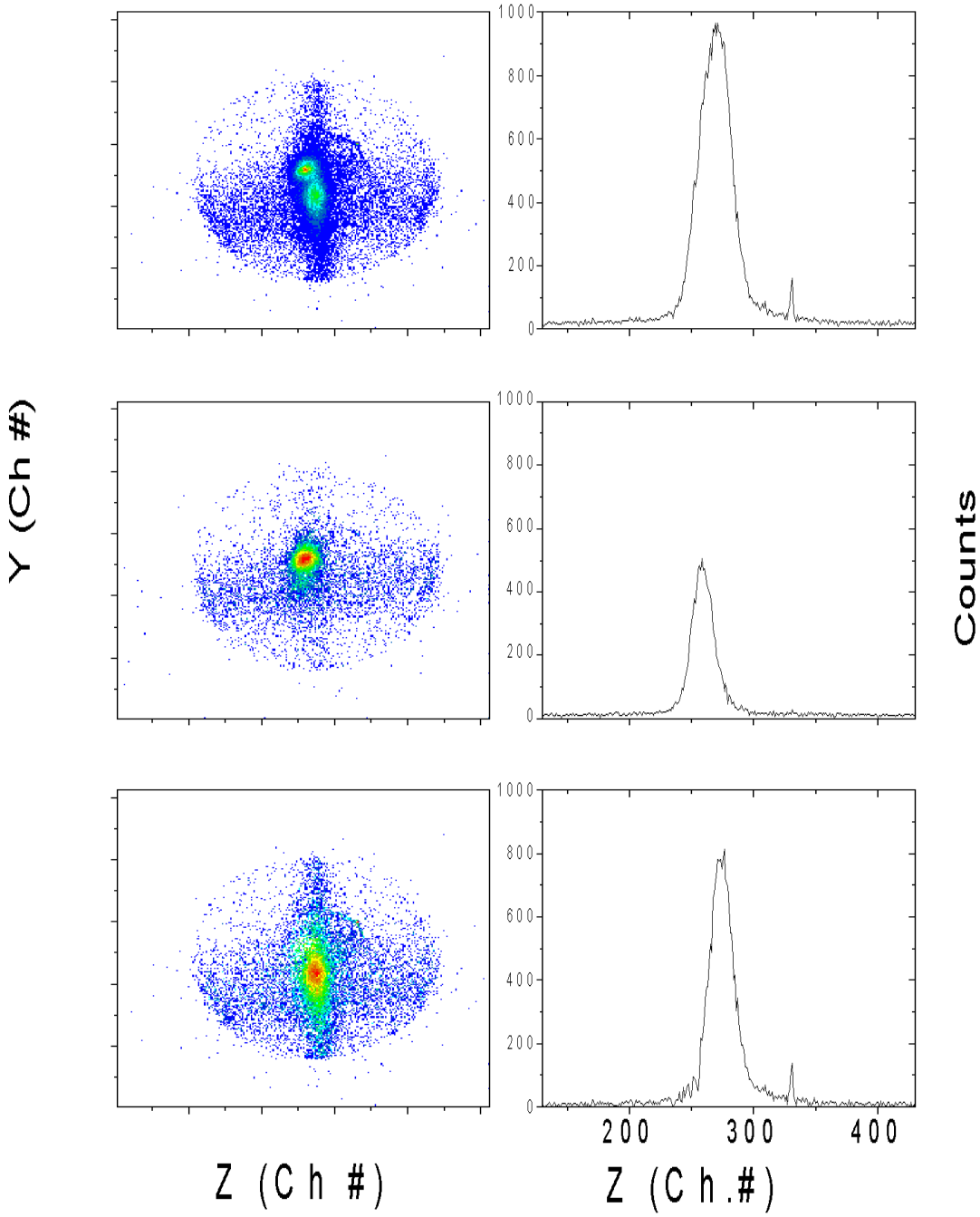
Y (Ch #)
Z (Ch #)
Z (Ch.#)
Counts
0
200
400
600
800
1000
200
300
400

Fig. 4.3. TI to SC ratio for 1 MeV/u O^{q+} incident on He. Included are the data of Tanis *et al*.[48] and Shinpaugh *et al*.[38]

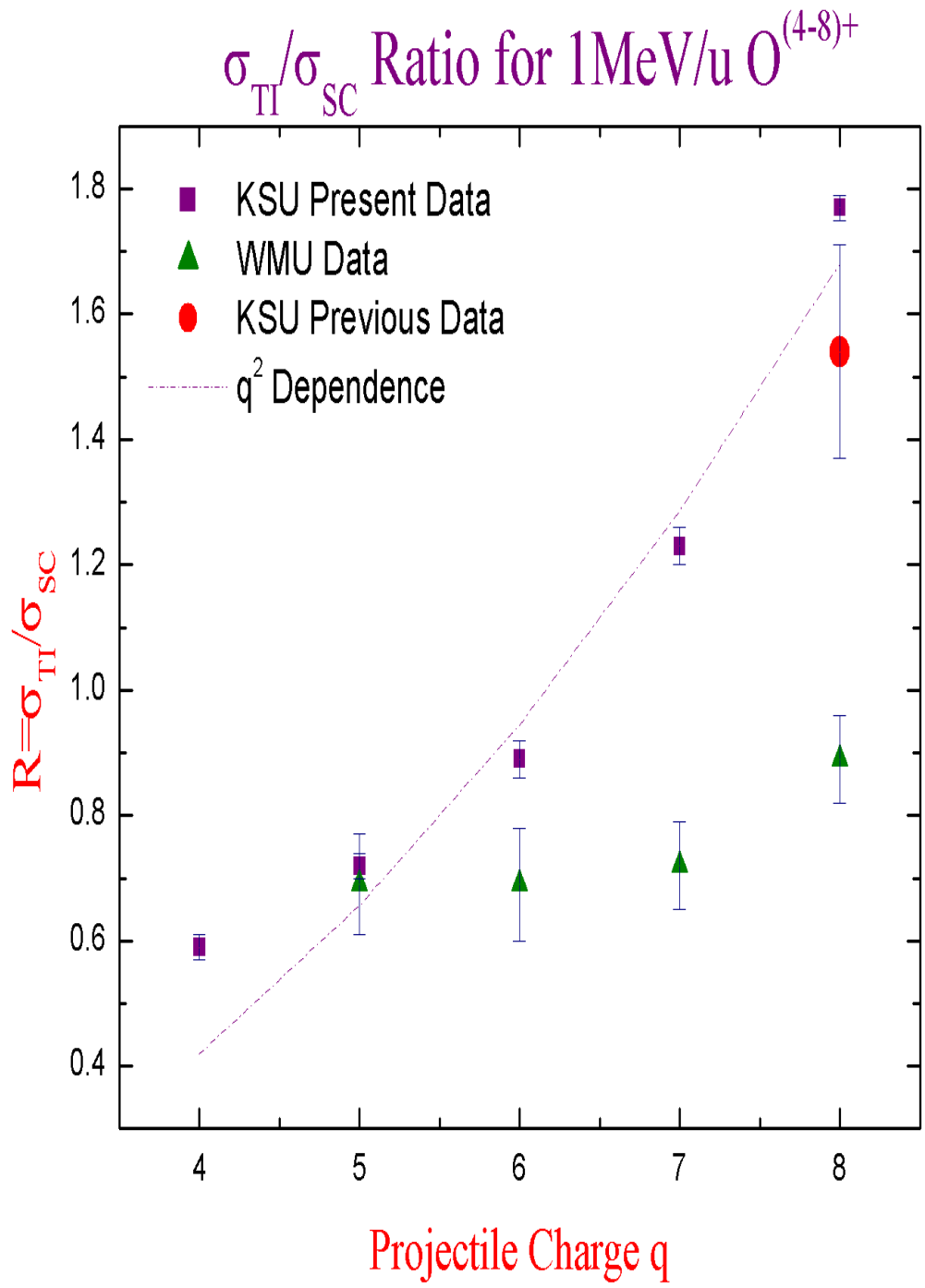
σTI/σSC Ratio for 1MeV/u O(4-8)+
KSU Present Data
WMU Data
KSU Previous Data
q2 Dependence
R=σTI/σSC
Projectile Charge q
1.8
1.6
1.4
1.2
1.0
0.8
0.6
0.4
4
5
6
7
8

If we assume that the two-electron removal from He is occurring by independent interactions with the projectile, the ratio of TI-to-SC is expected to vary as Z^2, where Z is the projectile charge. Our measurements follow the Z^2 dependence for bare and hydrogen like ion impact as expected. The deviation from the Z^2 dependence is relatively small.

The discrepancy of the measured values of R reported here with those previously published by Tanis *et al*.[48] for 1 MeV/u $^{(5\text{-}8)+}$ on He may be attributed to their experimental method. Moreover, their data do not include the corrections mentioned above.

B. Systematic Study of Velocity, Charge State and Energy Dependence of TI to SC Ratio for F^{q+} Incident on He

Figures 4.4 through 4.11 show measured relative cross sections of transfer ionization to single capture obtained in coincidences between charge exchanged projectiles and appropriate recoil ions for several different energies and charge states. Our study includes both dressed and bare fluorine projectiles. The target is delivered by the supersonic two-stage helium gas jet. The target was well localized therefore we have not suffered from the problems and corrections that occurred in previous gas cell experiments.

The data included are 0.5 MeV/u – 2.5 MeV/u $F^{(4-9)+}$ ions incident on He with three exceptions: First, we could not make the measurement for 0.5 MeV/u F^{9+} on He, because of the very low intensity of the projectile beam. The second and third ones were the 2.0 MeV/u F^{4+} and 2.5 MeV/u F^{5+}on He, which were not measured due to the fact that the dipole magnet was not powerful enough to bend the charge-exchanged beam of F^{3+} and F^{4+}, respectively. All other charge states at all energies were measured. In all runs analyzed, TI and SC peaks were clearly separated from any contamination contribution. For F^{q+} ions incident on He, the ratio of transfer ionization to single capture are given in Table 4.1.

We compared our measurements with available previous measurements and calculations done by Shingal *et al.*[51], and Tseng and Lin for bare and hydrogen like projectiles. Unfortunately calculations for $F^{(4-7)+}$ on He cases are not available to date, and no other experimental data exist. Also, the q^2 dependence is plotted as an eye guide for all the data. Even though it is not expected that the data will follow the q^2 dependence when R becomes large, it is used as a "reference guide" to the trend in the data. The q^2 dependence is normalized to the He^{2+} + He published data.[45,46]

Figure 4.6 shows a plot of the s_{TI}/s_{SC} ratios as a function of projectile charge q for 1 MeV/u $F^{(4-9)+}$ on He. The solid line represents a q^2 scaling normalized to He^{2+} + He. The bare F^{9+}, hydrogenlike F^{8+} and F^{7+} ratios scale extremely well with q^2 dependence normalized to the 1 MeV/u He^{2+} + He data. Furthermore, it is reasonable that the He^{2+} sees full screening for the tightly bound K-shell structure of F^{8+} and F^{7+} projectiles. The

calculations of our theory collaborators, Tseng and Lin, are displayed also. The calculated q dependence matches the data but slightly overestimates the measured ratio. We may conclude that these collisions can be approximately described within the perturbative regime. The data for F^{4+}, F^{5+} and partly F^{6+} demonstrate the effect of dressing the projectile. This anti-screening effect (which means "not full screening") takes place because ionization in the TI process occurs within the projectile electron cloud and increases the effective charge and therefore enhances the ionization cross-section. Deviations from the q^2 ratio can also arise from the behavior of the capture probability, however this probability is usually small for these systems as can be seen in the calculations of Tseng and Lin that are given in Fig. 2.7.

The trend seen in the 1 MeV/u data is characteristic of the data at other energies. The 0.5 MeV/u data in Fig. 4.4 is a good example. The F^{8+} and F^{7+} agree extremely well with the scaled He^{2+} + He data whereas the lower charge states show antiscreening. The highest energy data, 2 MeV/u, also agrees very well with the scaled He^{2+} + He data for F^{9+} but shows a behavior for the other charge states that cannot be explained by the simple screening model.

Table 4.1. The ratio of transfer ionization to single capture for F^{q+} incident on He.

0.5 MeV/u F^{q+}	
q	Ratio
4	0.849 ± 0.03
5	1.234 ± 0.04
6	1.450 ± 0.04
7	1.707 ± 0.07
8	2.309 ± 0.05

0.75 MeV/u F^{q+}	
q	Ratio
4	0.796 ±0.02
5	0.918 ± 0.05
6	1.258 ± 0.03
7	1.519 ± 0.05
8	2.055 ± 0.05
9	2.810 ± 0.05

1.0 MeV/u F^{q+}	
q	Ratio
4	0.66 ± 0.01
5	0.82 ± 0.01
6	1.07 ± 0.01
7	1.33 ± 0.01
8	1.77 ± 0.01
9	2.23 ± 0.05

1.25 MeV/u F^{q+}	
q	Ratio
4	0.61 ± 0.009
5	0.779 ± 0.01
6	0.91 ± 0.01
7	1.205 ± 0.03
8	1.62 ± 0.03
9	2.16 ± 0.03

1.5 MeV/u F^{q+}

q	Ratio
4	0.59 ± 0.01
5	0.64 ± 0.006
6	0.79 ± 0.008
7	1.07 ± 0.02
8	1.49 ± 0.01
9	2.03 ± 0.04

1.75 MeV/u F^{q+}

q	Ratio
4	-
5	0.616 ± 0.02
6	0.712 ± 0.02
7	0.892 ± 0.03
8	1.42 ± 0.04
9	1.923 ± 0.07

2 MeV/u F^{q+}

q	Ratio
4	-
5	0.627 ± 0.009
6	0.632 ± 0.007
7	0.82 ± 0.03
8	1.085 ± 0.04
9	1.87 ± 0.05

2.5 MeV/u F^{q+}

q	Ratio
4	-
5	-
6	0.513 ± 0.02
7	0.692 ± 0.03
8	0.913 ± 0.05
9	1.38 ± 0.13

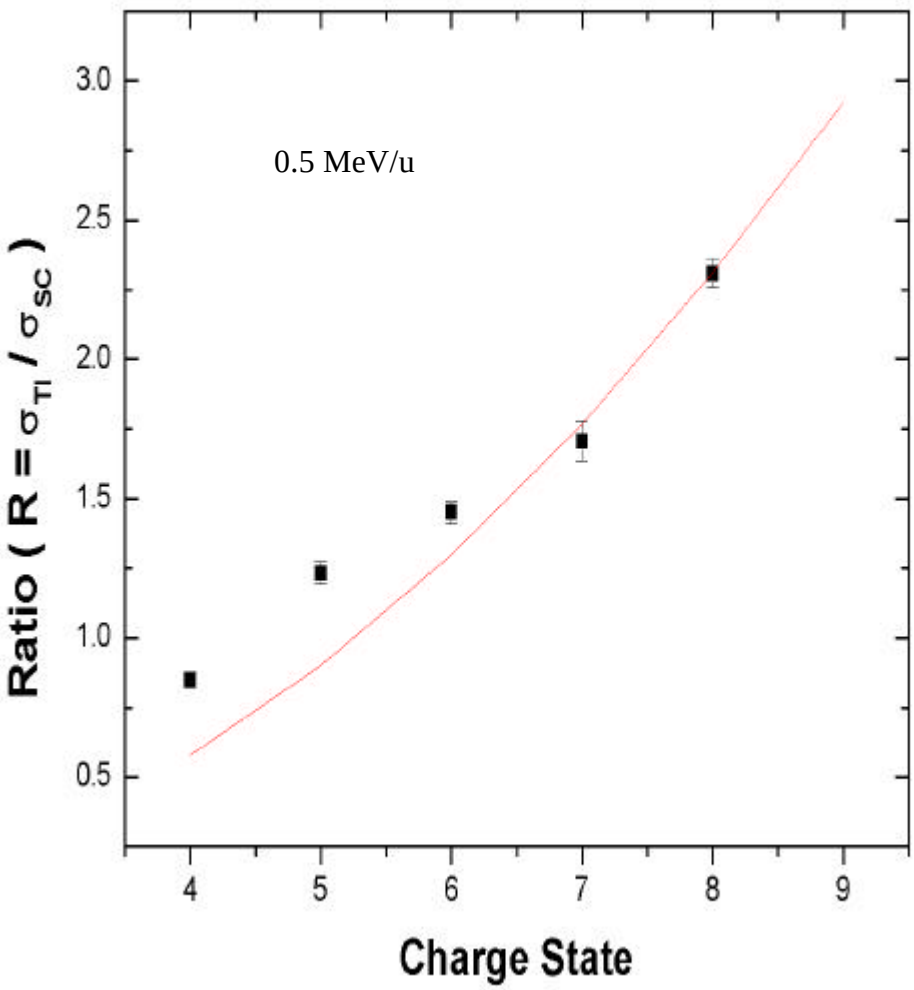

Fig. 4.4. The ratio of transfer ionization to single capture for 0.5 MeV/u $F^{(4-8)+}$ incident on He. The solid squares represent results from $F^{(4-8)+}$. The solid line represents a q^2 scaling normalized to He^{2+} + He. The error bars in the present data are purely statistical.

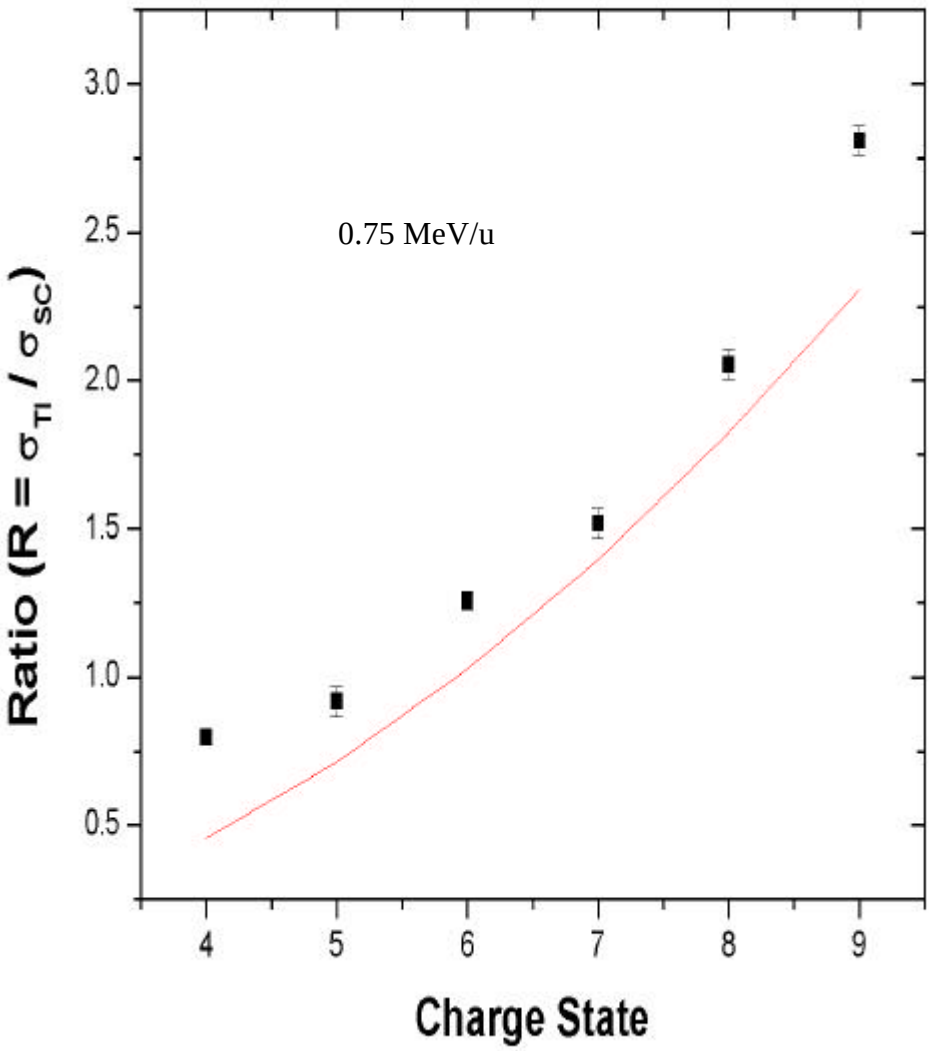

Fig. 4.5. Same as Caption 4.4 except for 0.75 MeV/u $F^{(4\text{-}9)+}$.

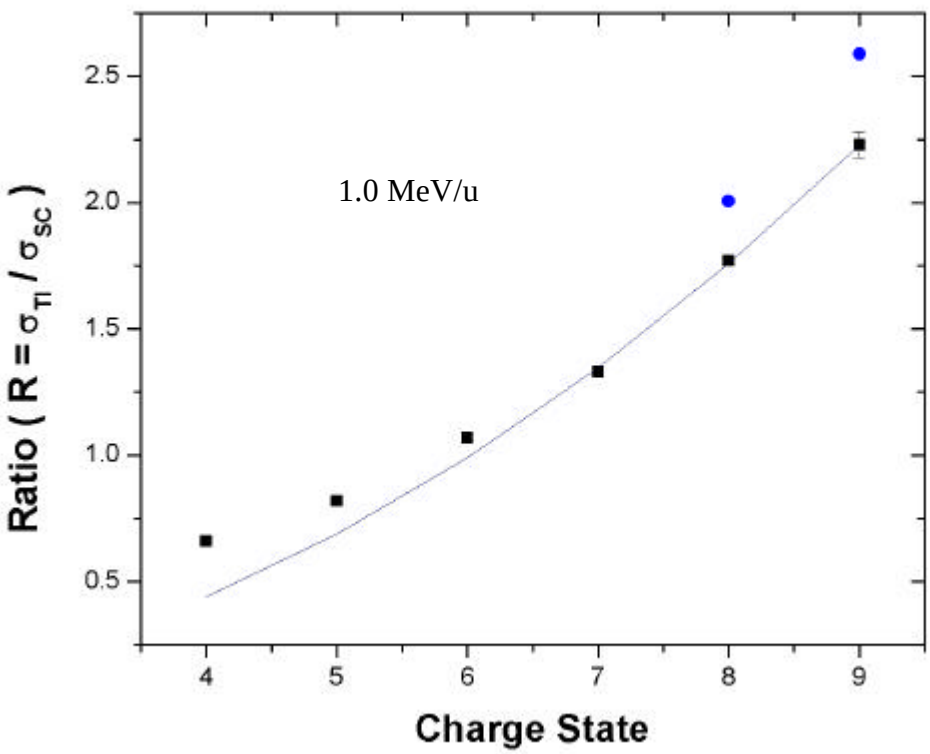

Fig. 4.6. Same as Caption 4.4 except for 1.0 MeV/u $F^{(4\text{-}9)+}$.

.

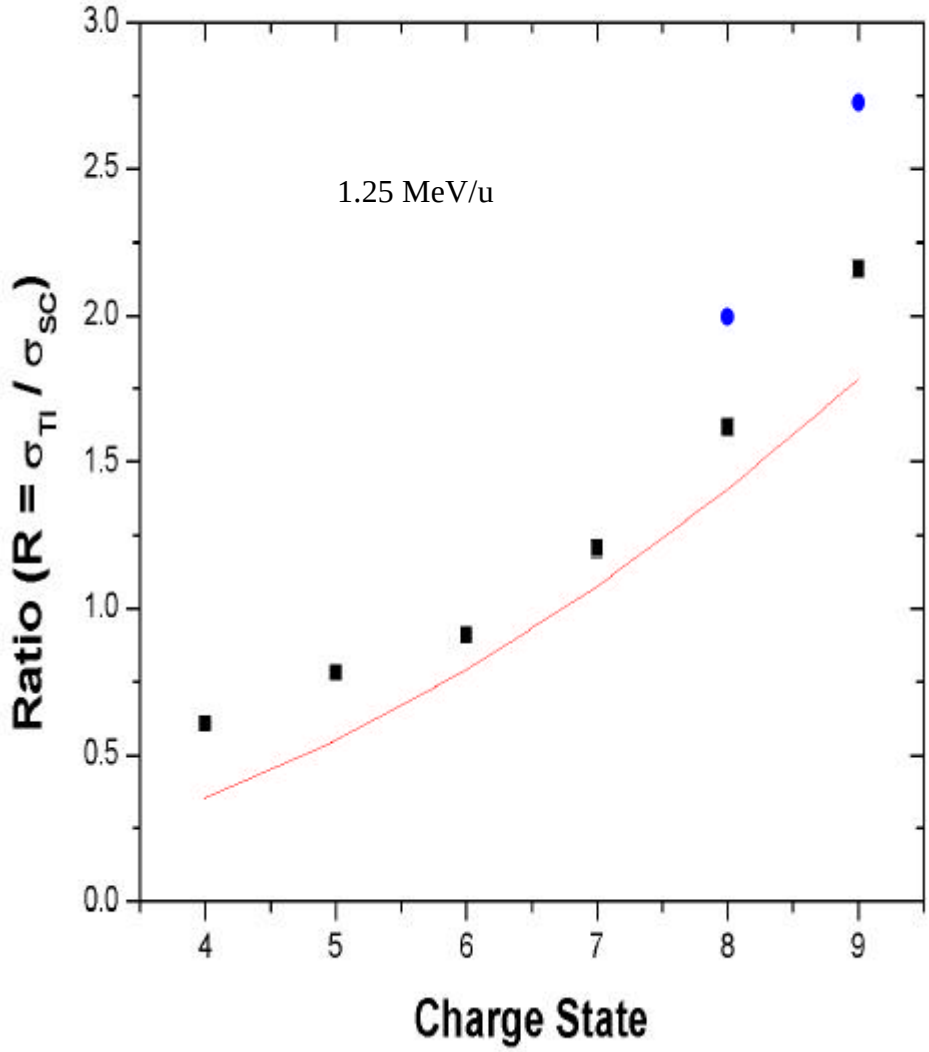

Fig. 4.7. Same as Caption 4.4 except for 1.25 MeV/u $F^{(4\text{-}9)+}$.

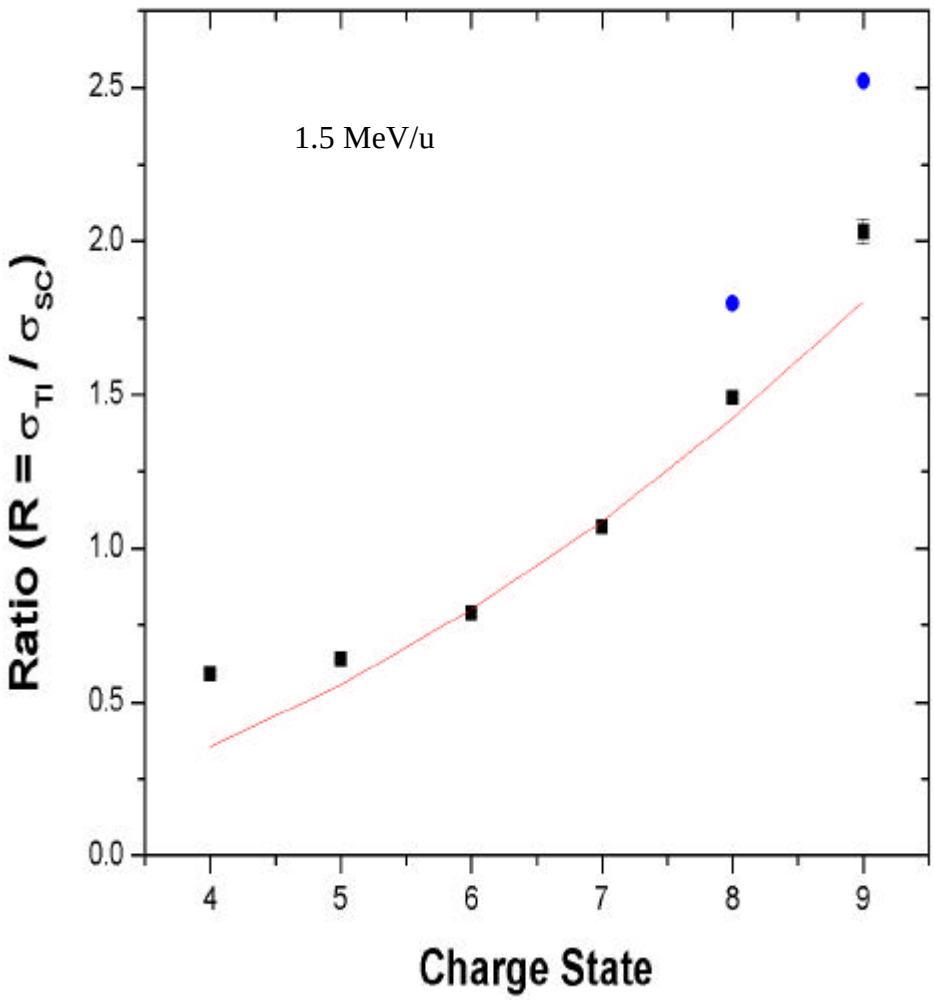

Fig. 4.8. Same as Caption 4.4 except for 1.5 MeV/u $F^{(4\text{-}9)+}$.

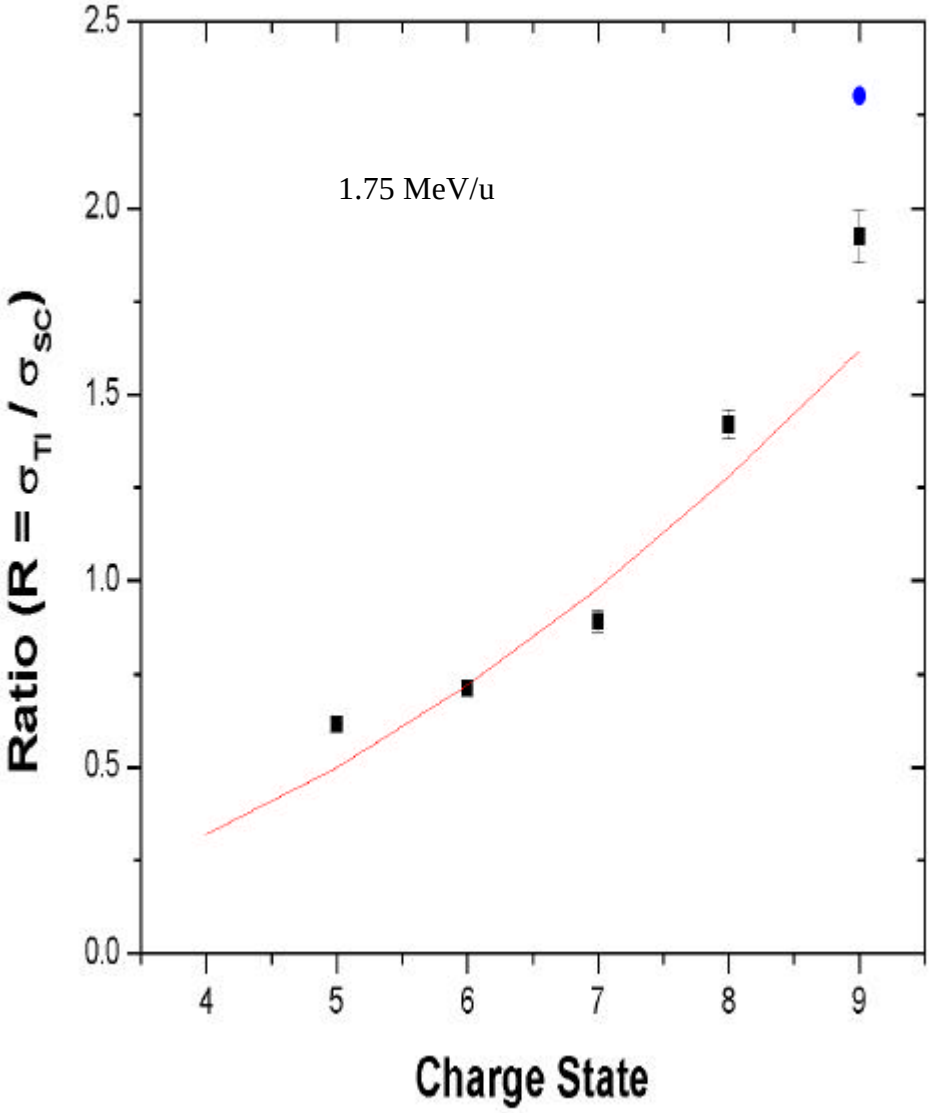

Fig. 4.9. Same as Caption 4.4 except for 1.75 MeV/u $F^{(5\text{-}9)+}$.

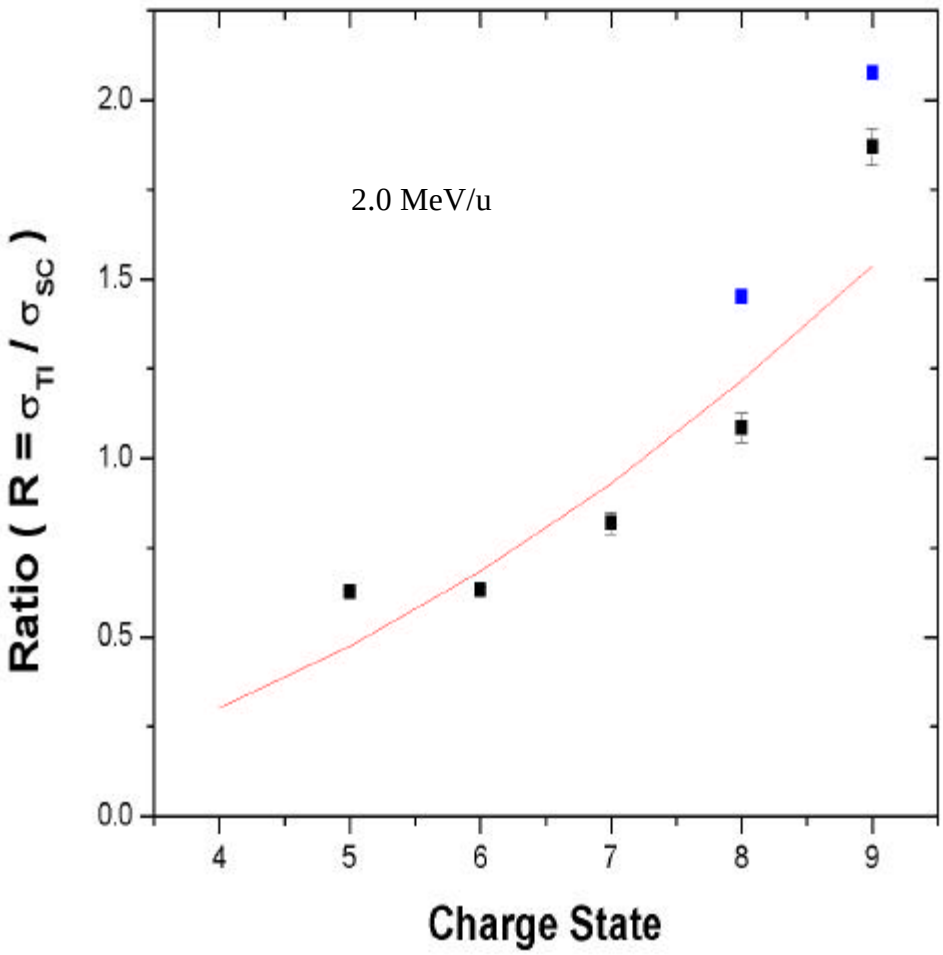

Fig. 4.10. Same as Caption 4.4 except for 2.0 MeV/u $F^{(5\text{-}9)+}$.

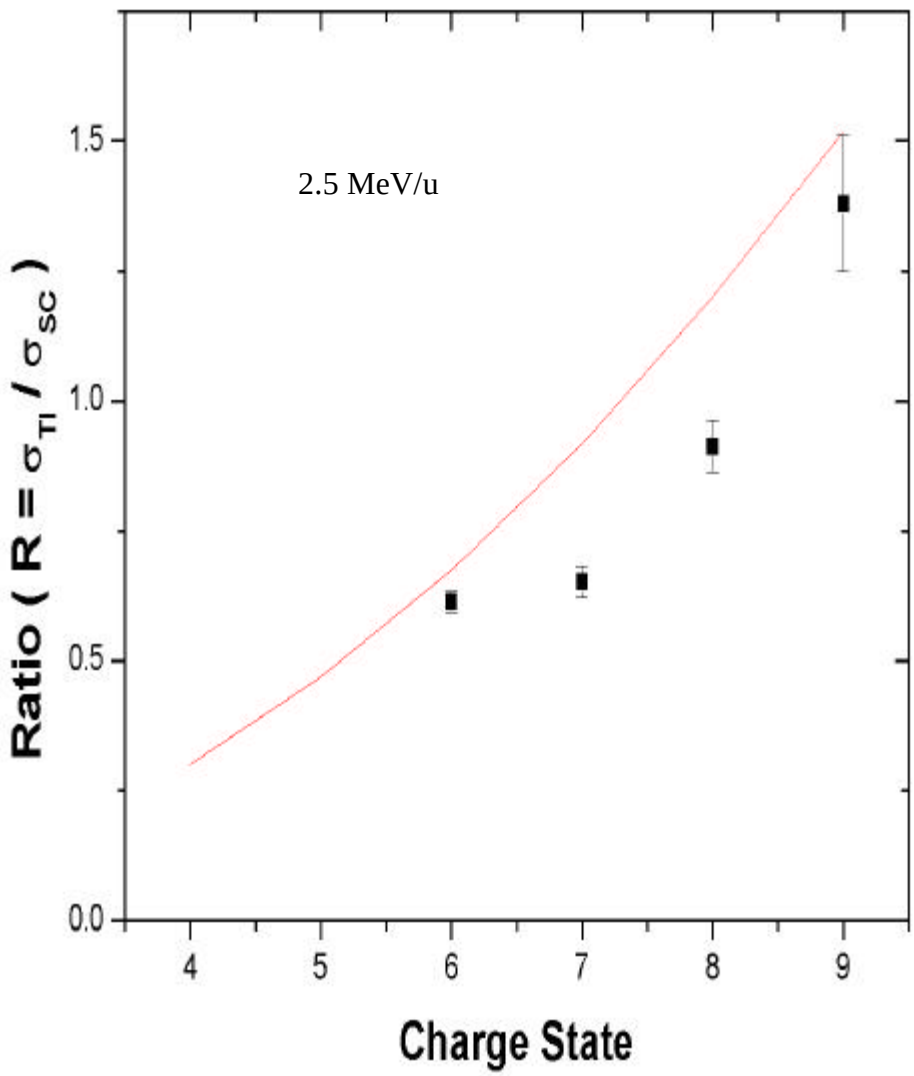

Fig. 4.11. Same as Caption 4.4 except for 2.5 MeV/u $F^{(6\text{-}9)+}$.

Figure 4.12 shows the energy dependence of the ratio, $\frac{s_{TI}}{s_{SC}}$, for F^{9+} on He. It includes present measurements, and results for Shinpaugh *et al*.[38], and calculations from Shingal and Lin[51], and Tseng and Lin. Present measurements qualitatively agree with Shinpaugh *et al*.[38] measurements. However, we see much larger $\frac{s_{TI}}{s_{SC}}$ ratios for the higher energy data points. We do not have measurements below 0.75 MeV/u for F^{9+}, which makes it impossible to compare with their data points in that region. There is fairly good agreement between the data and the calculations of Tseng and Lin, but large disagreements with Shingal *et al*.[51]

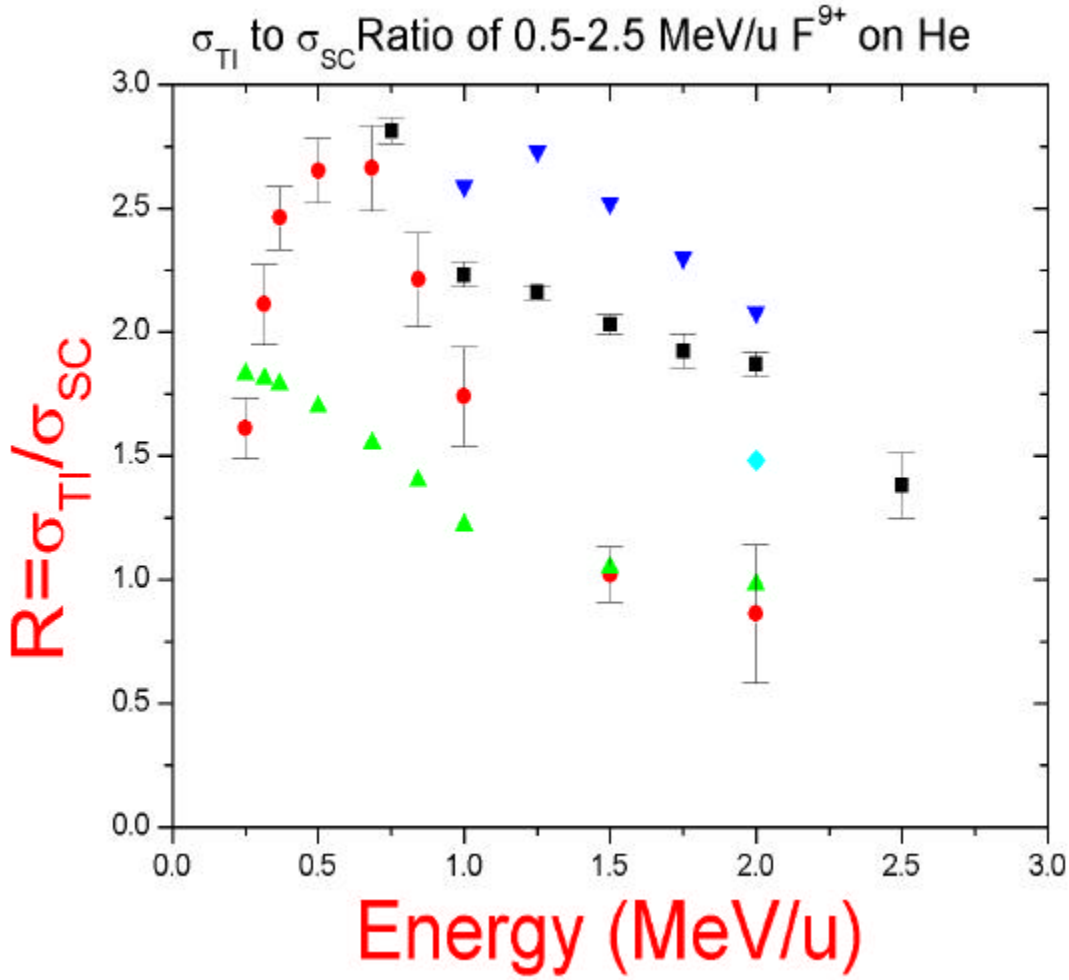

Fig. 4.12. The ratio of transfer ionization to single capture for F^{9+} incident on He. Symbols for data: solid squares, present data; solid circles, Shinpaugh *et al*.[Ref. 38]; solid diamond, Wu *et al*. [Ref. 36]. Theory: solid triangles, Shingal *et al*.[Ref. 51]; inverted triangles, Tseng *et al*.

C. Total One-Electron Transfer Cross Sections for F^{9+} and F^{8+} Incident on He

The single capture and transfer ionization cross sections were derived from the $\frac{s_{TI}}{s_{SC}}$ ratio measurements and the total one electron transfer cross sections provided from previous studies[73] by using the following relations:

$$s_{SC} = s^{q,q-1} \frac{1}{1+R} \qquad \text{Eq. 4.2}$$

$$s_{TI} = s^{q,q-1} \frac{R}{1+R} \qquad \text{Eq. 4.3}$$

For F^{8+} ions incident on He, the measured cross sections for total one-electron transfer, single capture and transfer ionization are given in table 4.2. These cross sections are plotted in Fig. 4.13. The calculations of Tseng and Lin are also given.

Table 4.2. Measured cross sections for one-electron transfer, single capture and transfer ionization for F^{8+} incident on He. The projectile velocity is given in MeV/u and all cross sections are given in units of 10^{-18} cm^2.

	Dillingham *et al.*[73]	F^{8+} + He			
E	s_{87}	s_{87}^{01}		s_{87}^{02}	
		Exp.	Theory	Exp.	Theory
0.50	80	24.1		55.8	
0.75	12.5	4.092		8.41	
1.00	3.37	1.22	1.166	2.15	2.339
1.25	1.57	0.599	0.467	0.971	0.931
1.50	0.67	0.268	0.205	0.399	0.369
1.75	0.38	0.157		0.223	
2.00	0.15	0.072	0.056	0.0781	0.0818
2.50	0.085	0.044		0.041	

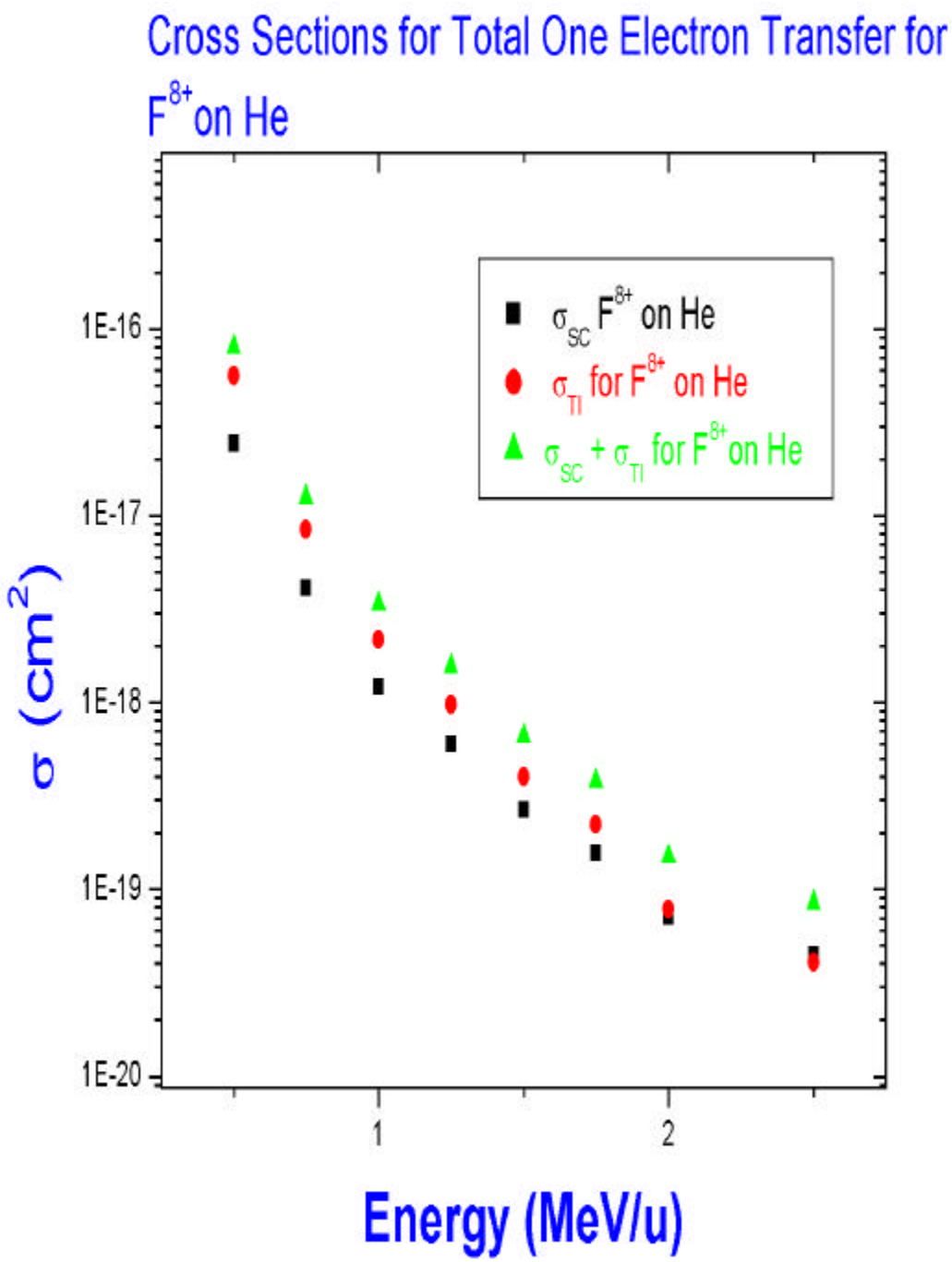

Fig. 4.13. Cross sections for total one-electron transfer, single capture, and transfer ionization for F^{8+} incident on He.

For F^{9+} ions incident on He, the measured cross sections for total one-electron transfer from Dillingham *et al*.[73], single capture, and transfer ionization are given in table 4.3. Total one-electron cross sections measured by Dillingham *et al*.[73] and by Shinpaugh *et al*.[38] are compared as shown in Fig. 4.14. The data show a good agreement between these two measurements. In this study Dillingham *et al*.[73] measurements of total one-electron transfer cross sections are used to determine the single capture and transfer ionization cross sections by equations 1 and 2. These cross sections are plotted in Fig. 4.15 and compared to the measurements of Shinpaugh *et al*.[38]

As seen in Fig. 4.15, Shinpaugh *et al*.[38] measurements indicate that transfer ionization is larger than single capture at low energies, where it dominates the capture process around the velocity of 0.6 MeV/u, and then single capture surpasses TI around 1.5 MeV/u. However, we observed that the TI process is dominant over the SC process over the energy range in the present study. Present results agree well with Shinpaugh *et al*.[38] for the TI cross section, but differ for the single capture process.

Table 4.3. Measured cross sections for one-electron transfer, single capture and transfer ionization for F^{9+} incident on He. The projectile velocity is given in MeV/u and all cross sections are given in units of 10^{-18} cm^2. The calculations of Tseng and lin are also given.

	Dillingham *et al.* [73]	F^{9+} + He			
E	s_{98}	s_{98}^{01}		s_{98}^{02}	
		Exp.	Theory	Exp.	Theory
0.50	-	-		-	
0.75	13	3.41		9.59	
1.00	5.26	1.63	1.254	3.63	3.245
1.25	2.20	0.696	0.49	1.50	1.335
1.50	1.00	0.33	0.220	0.67	0.554
1.75	0.50	0.171		0.329	
2.00	0.28	0.0976	0.061	0.182	0.127
2.50	0.14	0.0588		0.0812	

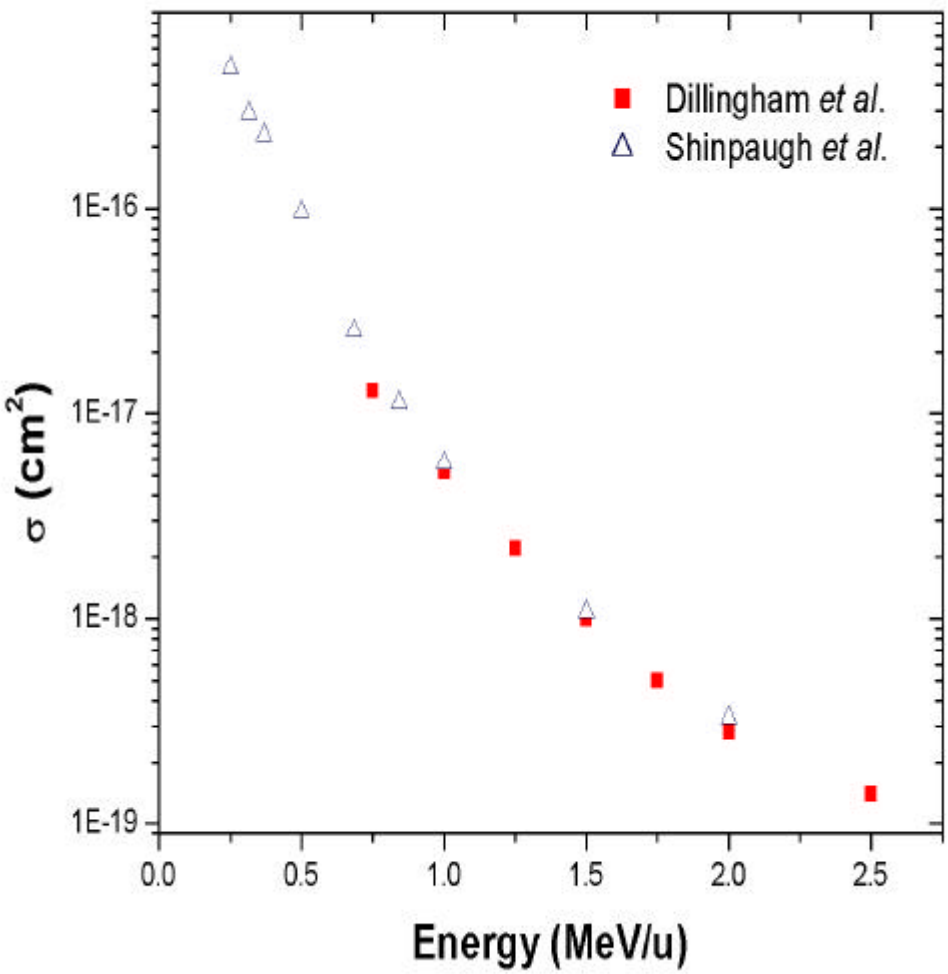

Fig. 4.14. Total one-electron transfer cross sections for F^{9+} incident on He. Symbols for data: solid squares, Dillingham *et al*. [Ref. 73]; open triangles, Shinpaugh *et al*.[Ref. 38]

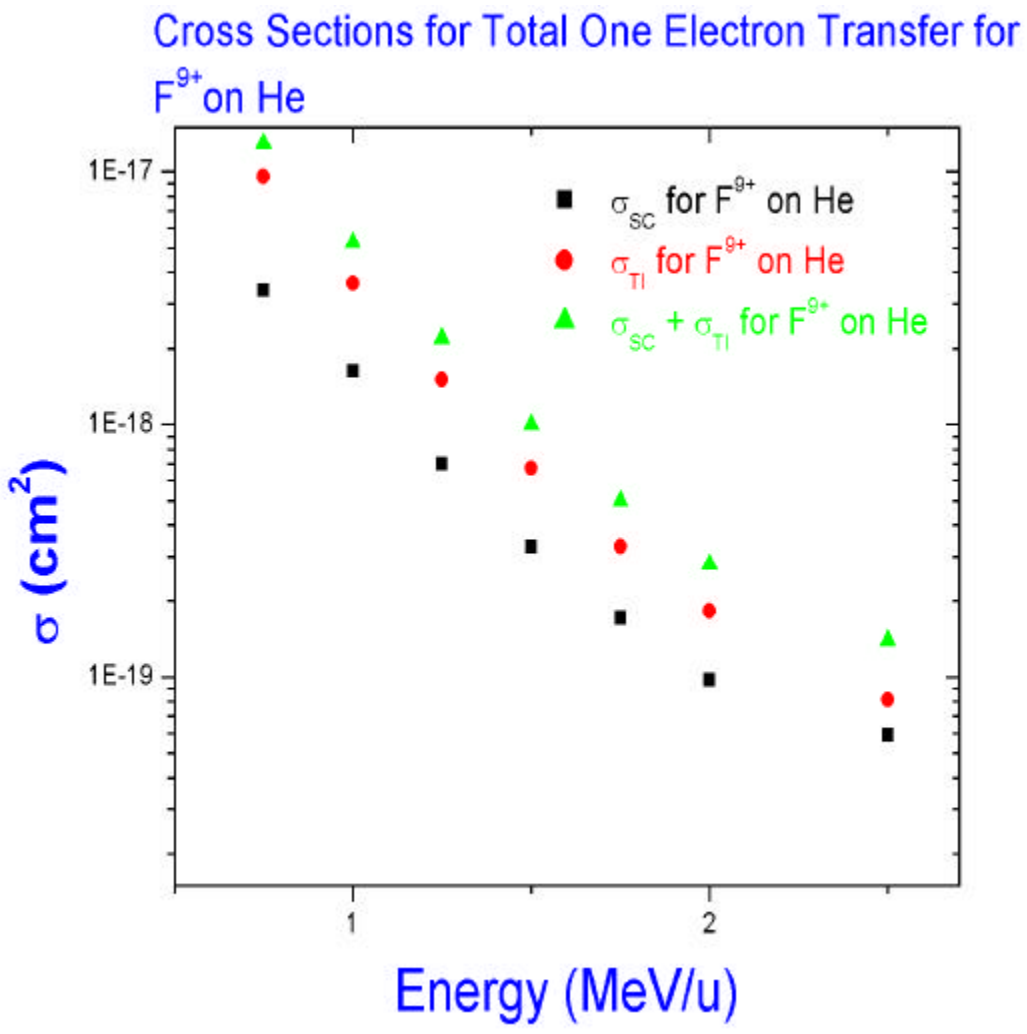

Fig. 4.15. Cross sections for total one-electron transfer, single capture, and transfer ionization for F^{9+} incident on He.

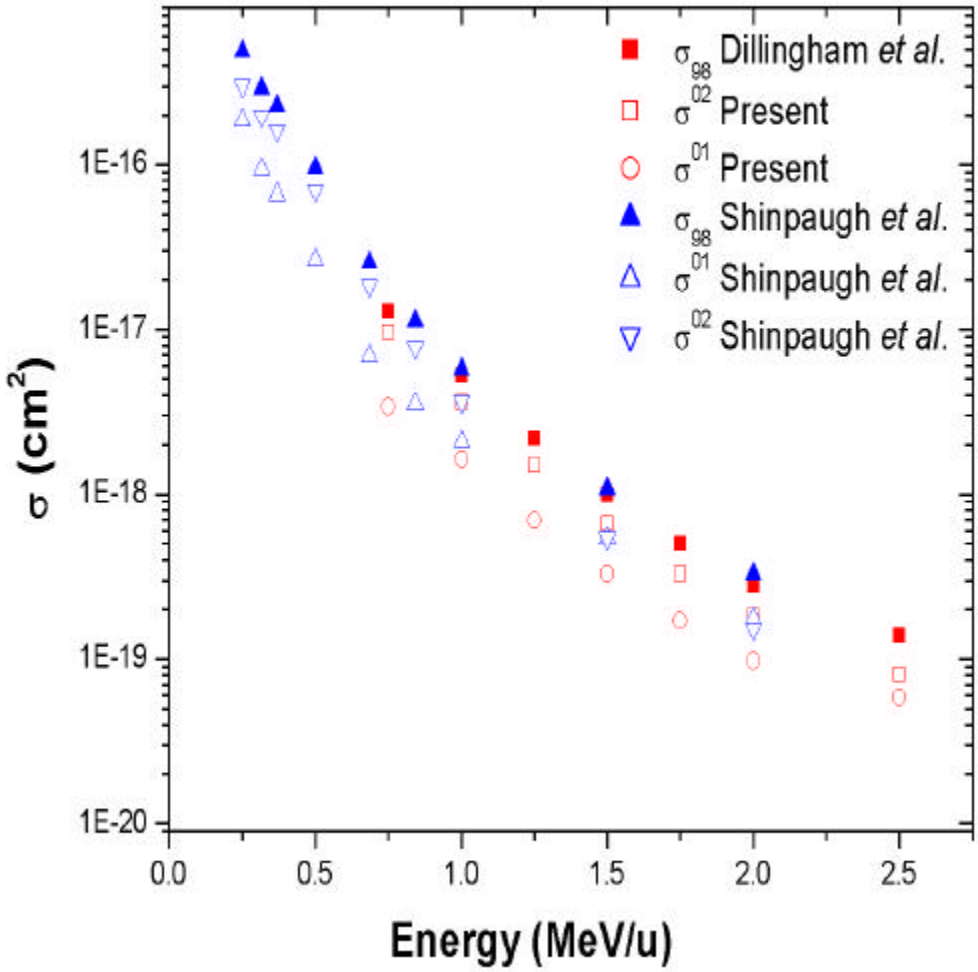

Fig. 4.16. Cross sections for total one-electron transfer, single capture, and transfer ionization for F^{9+} incident on He. Symbols for data: solid squares, Dillingham *et al*. [Ref. 73]; solid triangles, open triangles and inverted open triangles Shinpaugh *et al*.[Ref. 38]: open squares and open circles, Present.

D. TI and SC for Z > 9 projectiles

The other question that we have addressed with the TI/SC ratio is the projectile q dependence for projectiles greater than q=9. The big unanswered question here is the sudden fall in the TI/SC ratio for values of q above q = 20, as reported by Datz *et al.*[49] shown in Fig 2.3

In the first set of experiments for Z > 9 ions, extended our studies[50,70] to new measurements for Si, Ti, and Cu. The results of this data are given in Table 4.4 and Table 4.5. In Fig. 4.17, we see a ratio that follows a q^2 dependence up to approximately q = 9. Above q = 9 the experiment exceeds the q^2 dependence prediction due to antiscreening. The new data, Fig. 4.18, Si, Cl and Ti go up only to q = 18 and show a smooth monotonically increasing TI/SC ratio. The inverted triangles are data for Ti^{15+} and Ti^{18+} from Montenegro *et al.*[34] The new data points for $Ti^{15,17,18+}$ have smaller errors, and when combined with the $Cu^{18,20+}$, Fig. 4.19, reflect a more gently increasing behavior than might be inferred from the earlier Ti data. Moreover, the high q data of Datz *et al.*[49], which showed TI/SC ratios of approximately 2, is 5 times smaller than our TI/SC ratio for q = 20.

Therefore, in our final experiment these measurements were performed for I^{q+} beams at 0.25 MeV/u, 0.375 MeV/u and 0.5 MeV/u. We have extended our measurements up to $q = 25$ in order to compare directly with Datz *et al.*[49] Results are given in Table 4.6. Measurements for 0.25 MeV/u I^{q+} (q = 15, 17 and 19) are shown in Fig. 4.20. The present measurement differs by a factor of ~2.5 from those of Datz *et al.*[49] Their measured ratio, $\frac{s_{TI}}{s_{SC}}$, for $q = 15$ to 20 seems to be constant at ~1.5 and after that drops down to approximately one at q = 27. However, we observe a decrease in the ratio in the same region, which led us to make further measurements to see whether or not the ratio is energy dependent. The results are shown in Fig. 4.21 for 0.375 MeV/u $I^{(17,19,21,23,25)+}$ on He and in Fig. 4.22 for 0.5 MeV/u $I^{(19,21,23)+}$ on He cases. The ratio differs by a factor of 7 for 0.375 MeV/u I^{q+} on He compared with 0.25 Me/u I^{q+} on He case of Datz *et al.*[49] Our measurements indicate that the ratio, $\frac{s_{TI}}{s_{SC}}$, first increases and

peaks around $q = 19$ and then decreases. The most significant result of these sets of measurements is the very steep rise in the $\frac{s_{TI}}{s_{SC}}$ ratio with energy as shown in Fig. 4.23. Datz *et al*.[49] observed only a small rise in the $\frac{s_{TI}}{s_{SC}}$ ratio between the 0.1 and 0.25 MeV/u I^{q+} cases, besides being a factor of 3 below the present data at 0.25 MeV/u. The present results of the I^{q+} data are more in line with the trends expected for the lower z data. This can be seen in the global plot of all the data taken by Recoil Ion Momentum Spectroscopy (Fig. 4.24).

Table 4.4. The ratio of transfer ionization to single capture for 2 MeV/u A^{q+} incident on He.

Projectile Charge State		Ratio		
	Q	Present	Wong *et al*.	Montenegro *et al*.
F^{q+}	5	0.627 ± 0.009		
	6	0.632 ± 0.007		
	7	0.820 ± 0.030		
	8	1.085 ± 0.040		
	9	1.870 ± 0.050		
Si^{q+}	12	3.340 ± 0.190		
Cl^{q+}	13	4.450 ± 0.200	4.400 ± 0.400	
	14	4.190 ± 0.310	5.400 ± 0.400	
	15	6.420 ± 0.425	5.190 ± 0.400	
Ti^{q+}	15	6.100 ± 0.310		7.500 ± 1.500
	17	7.220 ± 0.370		
	18	8.470 ± 1.100		16.75 ± 6.000

Table 4.5. The ratio of transfer ionization to single capture for 1.6 and 1.75 MeV/u Cu^{q+} incident on He.

Energy (MeV/u)	Charge State q	Ratio R
1.6	Cu^{18+}	10.34 ± 0.67
1.6	Cu^{20+}	10.48 ± 0.912
1.75	Cu^{18+}	12.50 ± 0.672

Table 4.6. The ratio of transfer ionization to single capture for I^{q+} incident on He.

0.25 MeV/u I^{q+}

Charge State	Ratio	
q	Present	Datz *et al.*[49]
15	4.104 ± 0.34	1.39
17	3.74 ± 0.23	1.44
19	3.51 ± 0.14	1.35
21		1.41
23		1.15
25		1.12
27		1.06

0.375 MeV/u I^{q+}

q	Ratio
17	9.62 ± 0.22
19	11.24 ± 0.19
21	11.30 ± 0.20
23	9.18 ± 0.21
25	8.67 ± 0.45

0.50 MeV/u I^{q+}

q	Ratio
19	16.40 ± 0.41
21	17.97 ± 0.32
23	16.07 ± 0.36
25	14.61 ± 0.48

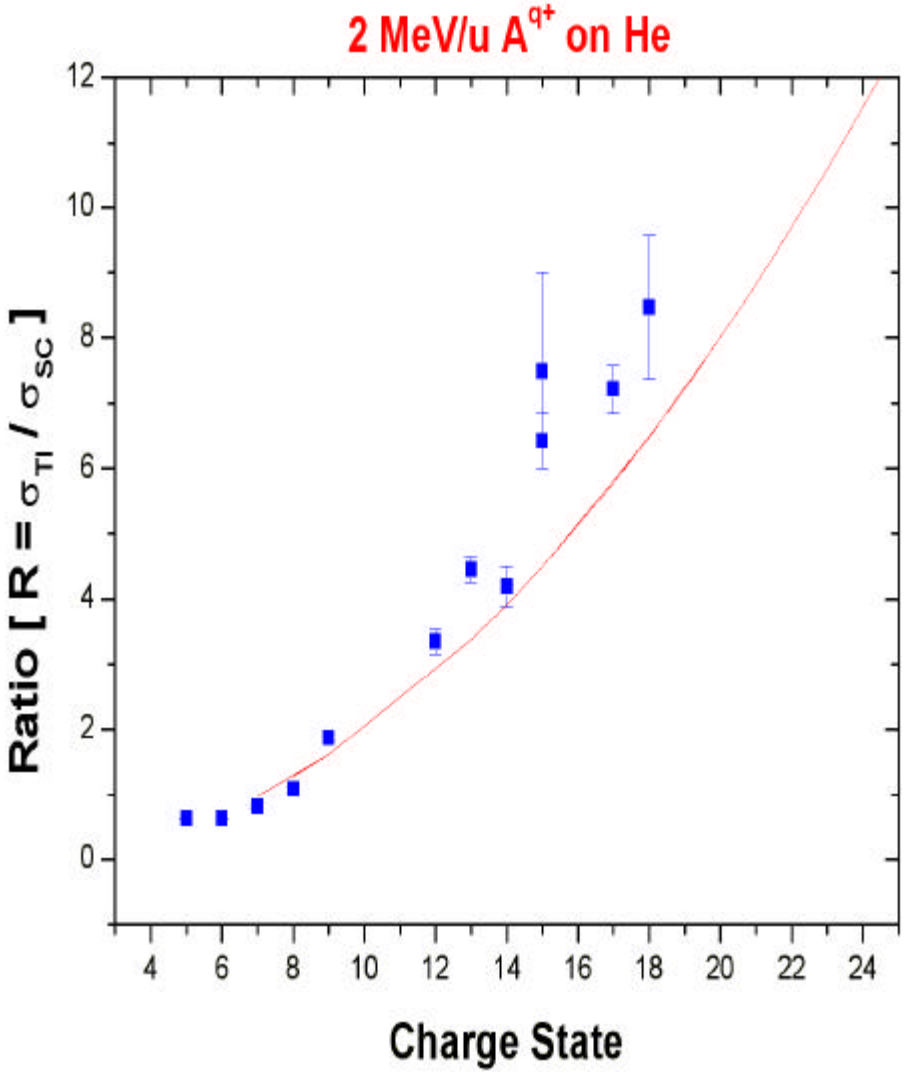

Fig. 4.17. Charge state dependence of SC and TI processes in 2 MeV/u A^{q+} on He system.

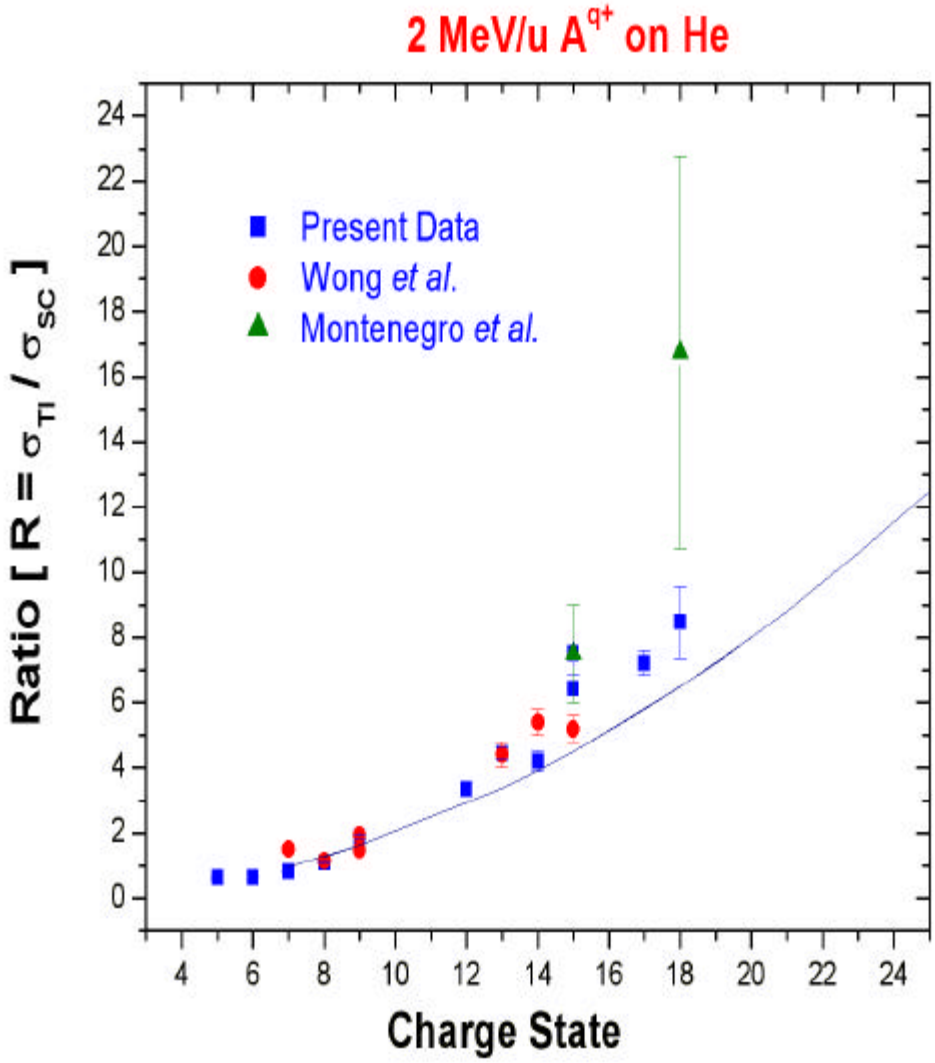

Fig. 4.18. Charge state dependence of SC and TI processes in 2 MeV/u A^{q+} on He system. Symbols for data: solid squares, present data; solid circles, Wong *et al*.[Ref. 70]; solid triangles, Montenegro *et al*. [Ref.50].

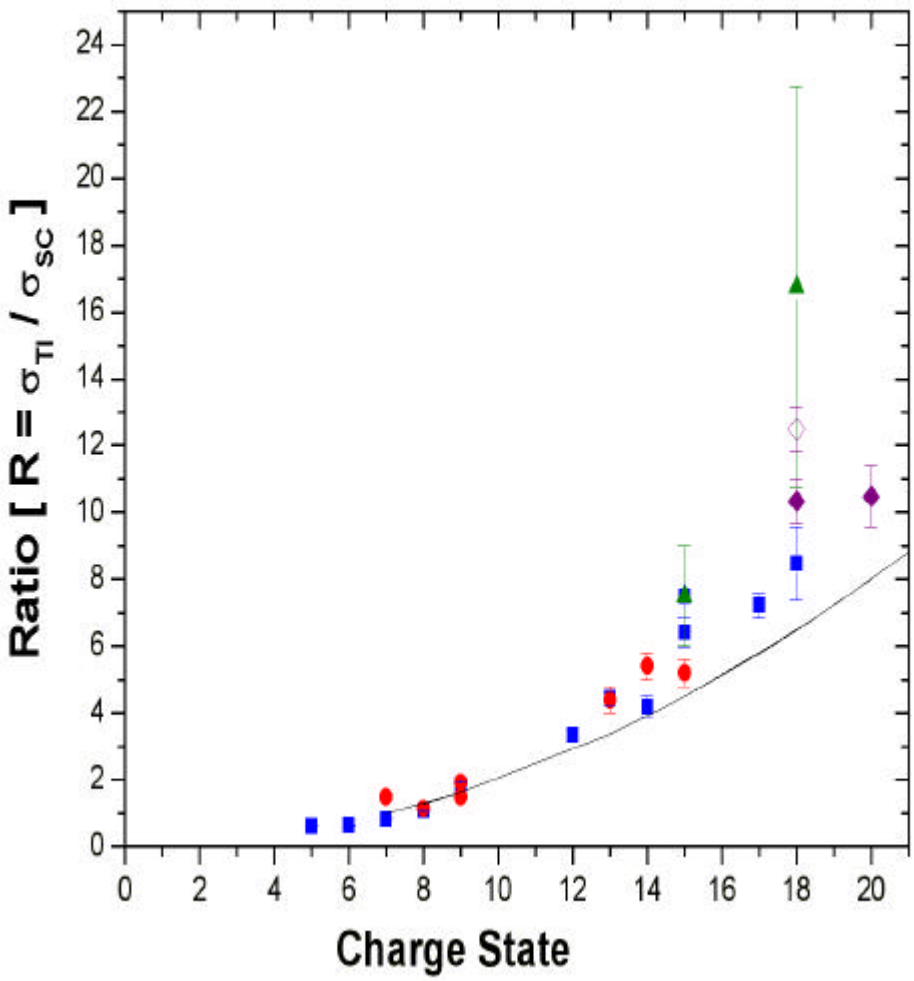

Fig. 4.19. Charge state dependence of SC and TI processes in A^{q+} on He system. Symbols for data: solid squares, 2 MeV/u A^{q+}, are the present results; solid circles, 2 MeV/u A^{q+}, Wong *et al*.[Ref. 70]; solid triangles, 2 MeV/u A^{q+}, Montenegro *et al*.[Ref. 50]; solid diamonds, 1.6 MeV/u Cu^{q+}, present results; open diamonds, 1.75 MeV/u Cu^{q+}, present.

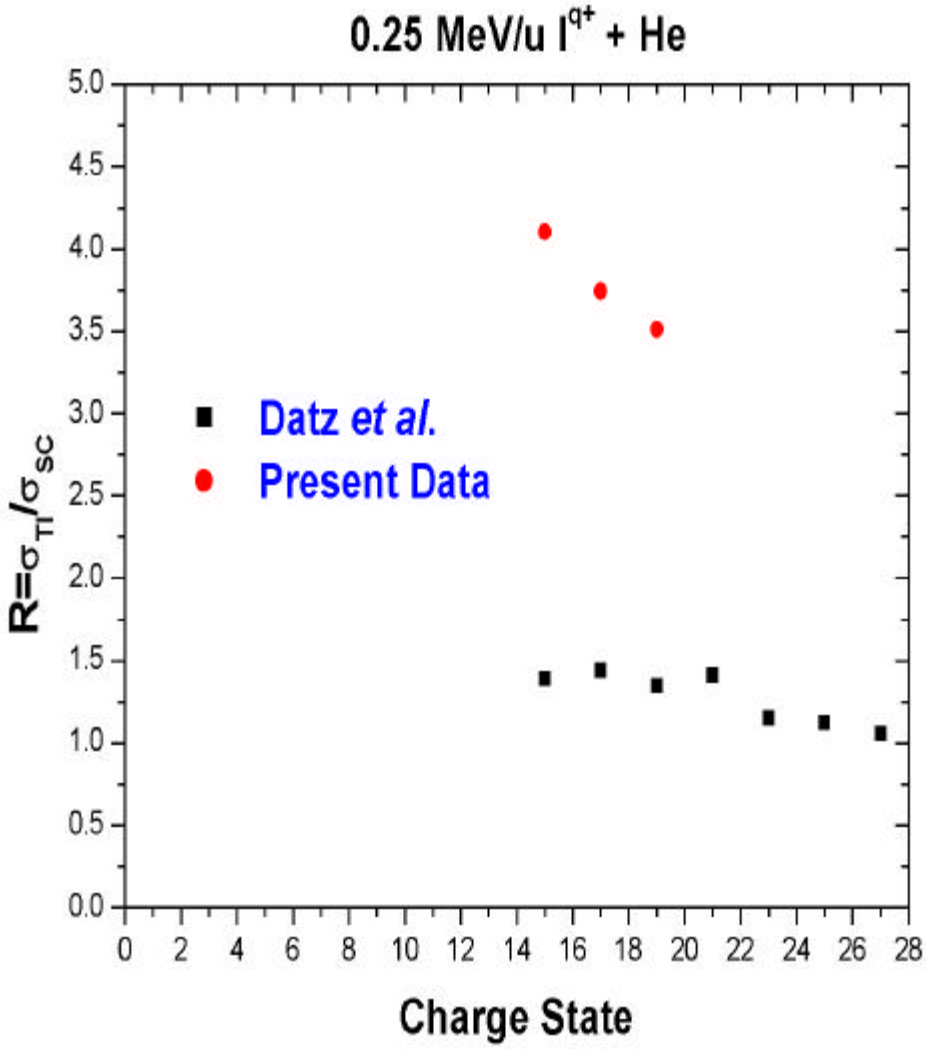

Fig. 4.20. The ratio of transfer ionization to single capture for 0.25 MeV/u I^{q+} incident on He. Solid circles are the present results and the solid squares are the results for Datz *et al*.[49]

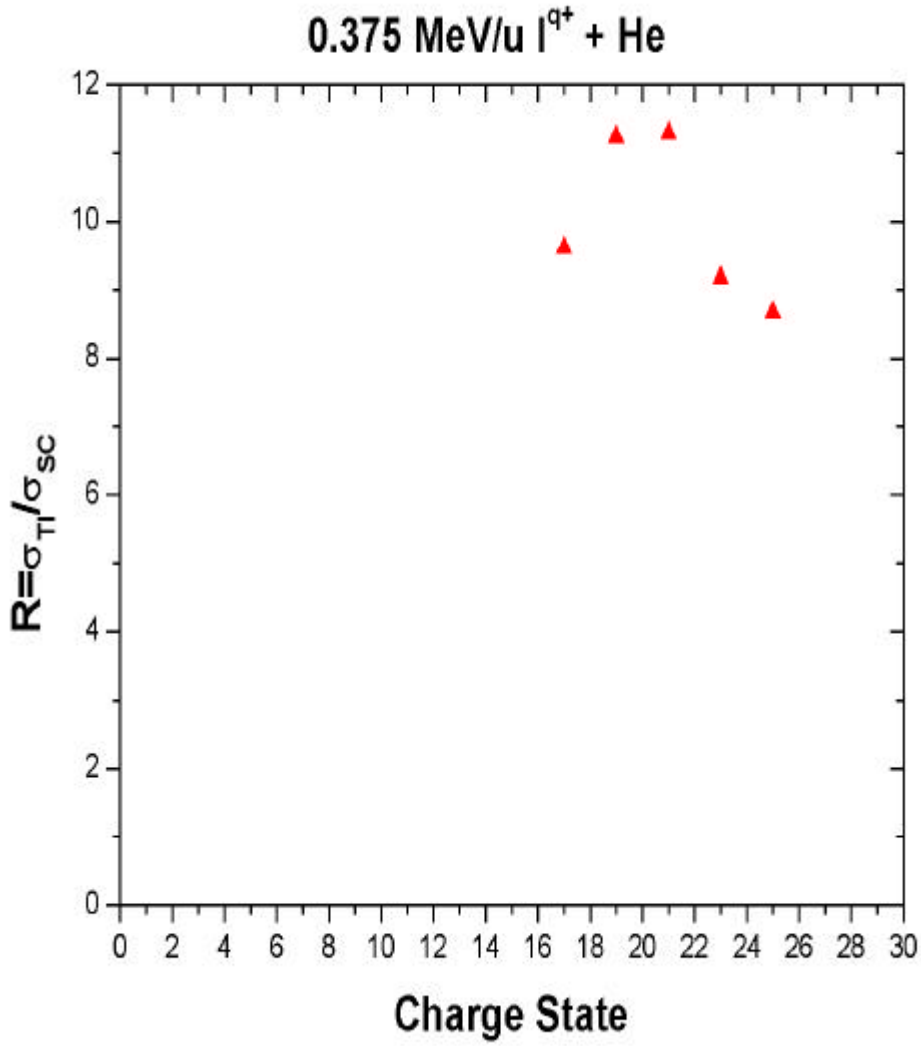

Fig. 4.21. The ratio of transfer ionization to single capture for 0.375 MeV/u I^{q+} incident on He. The solid triangles are the results of the present experiment.

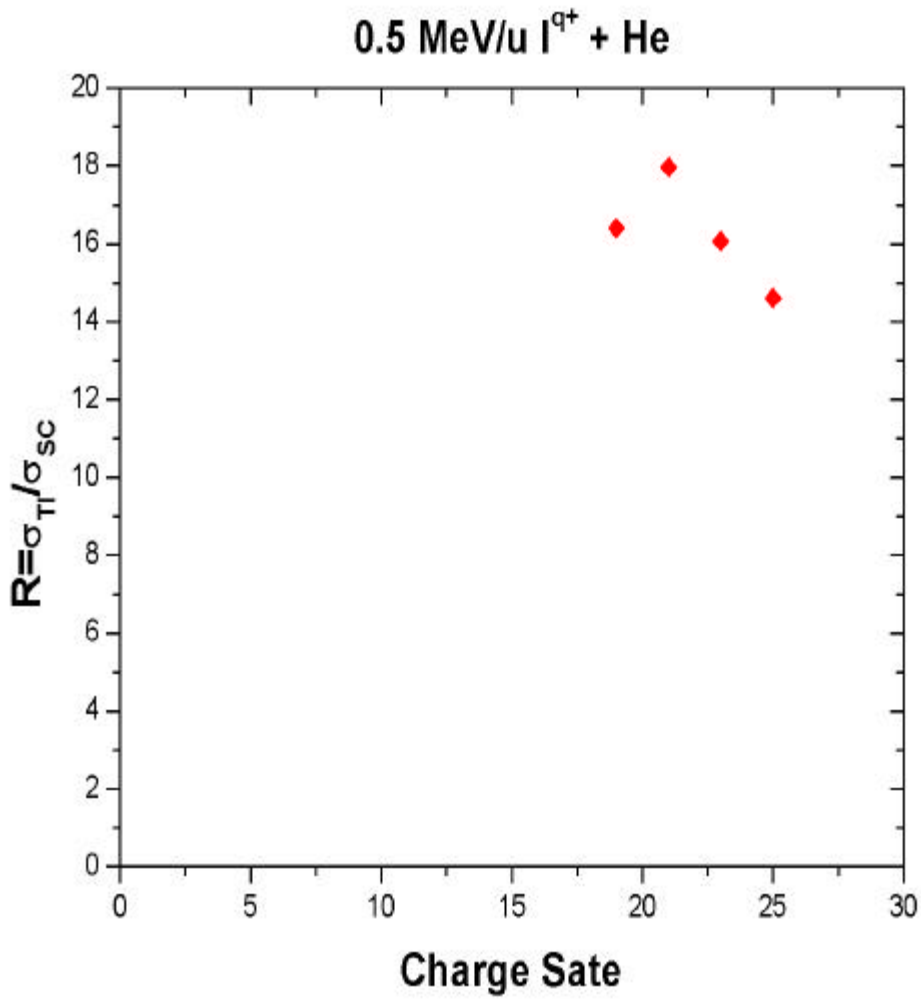

Fig.4.22. The ratio of transfer ionization to single capture for 0.5 MeV/u I^{q+} incident on He. The solid diamonds are the result of the present experiment.

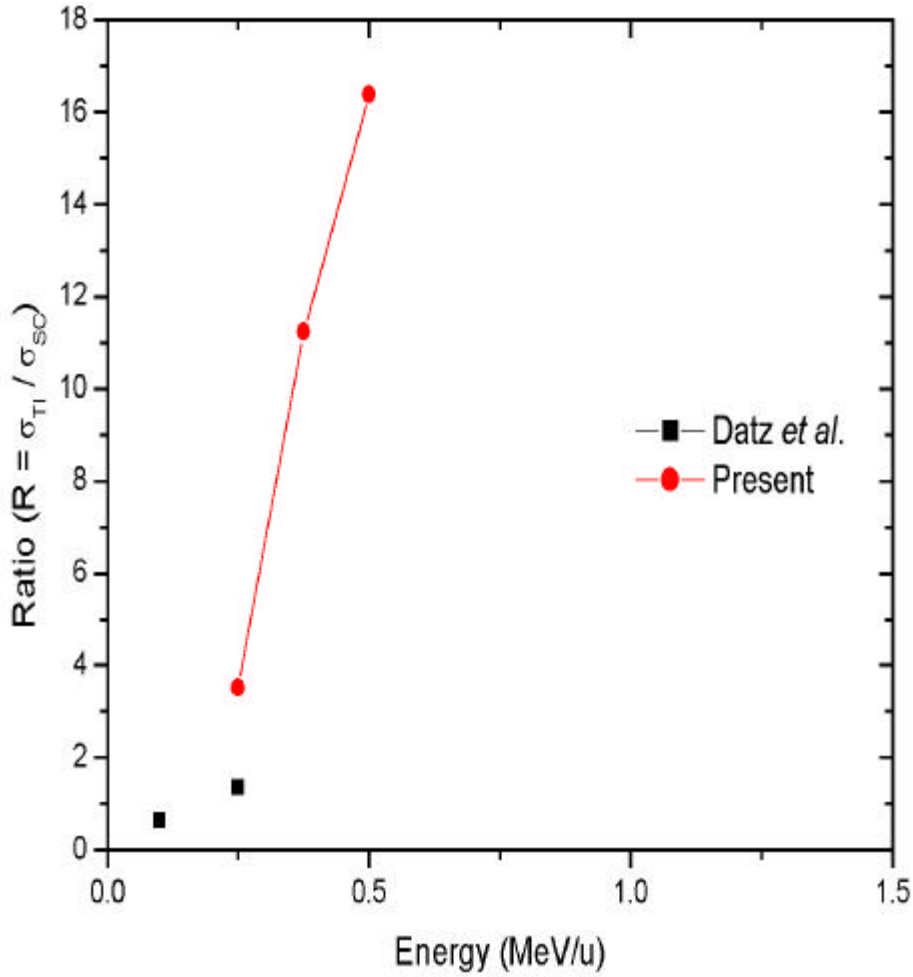

Fig. 4.23. Energy dependence of the ratio of $\frac{s_{TI}}{s_{SC}}$ for I^{19+} on He. Datz *et al*.[49] data are for I^{16+} at 0.10 MeV/u and for I^{19+} at 0.25 MeV/u.

Fig. 4.24. Charge state dependence of SC and TI processes in A^{q+} on He system. Symbols for data: solid squares, 2 MeV/u A^{q+}, are the present results; solid circles, 2 MeV/u A^{q+}, Wong *et al*.[Ref. 70]; solid triangles, 2 MeV/u A^{q+}, Montenegro *et al*.[Ref. 50]; solid diamonds, 1.6 MeV/u Cu^{q+}, present results; open diamonds, 1.75 MeV/u Cu^{q+}, (present.); Δ - I^{q+} (0.25 MeV/u, present data); ∇ - I^{q+} (0.375 MeV/u); $\triangleright$ - I^{q+} (0.5 MeV/u, present data)

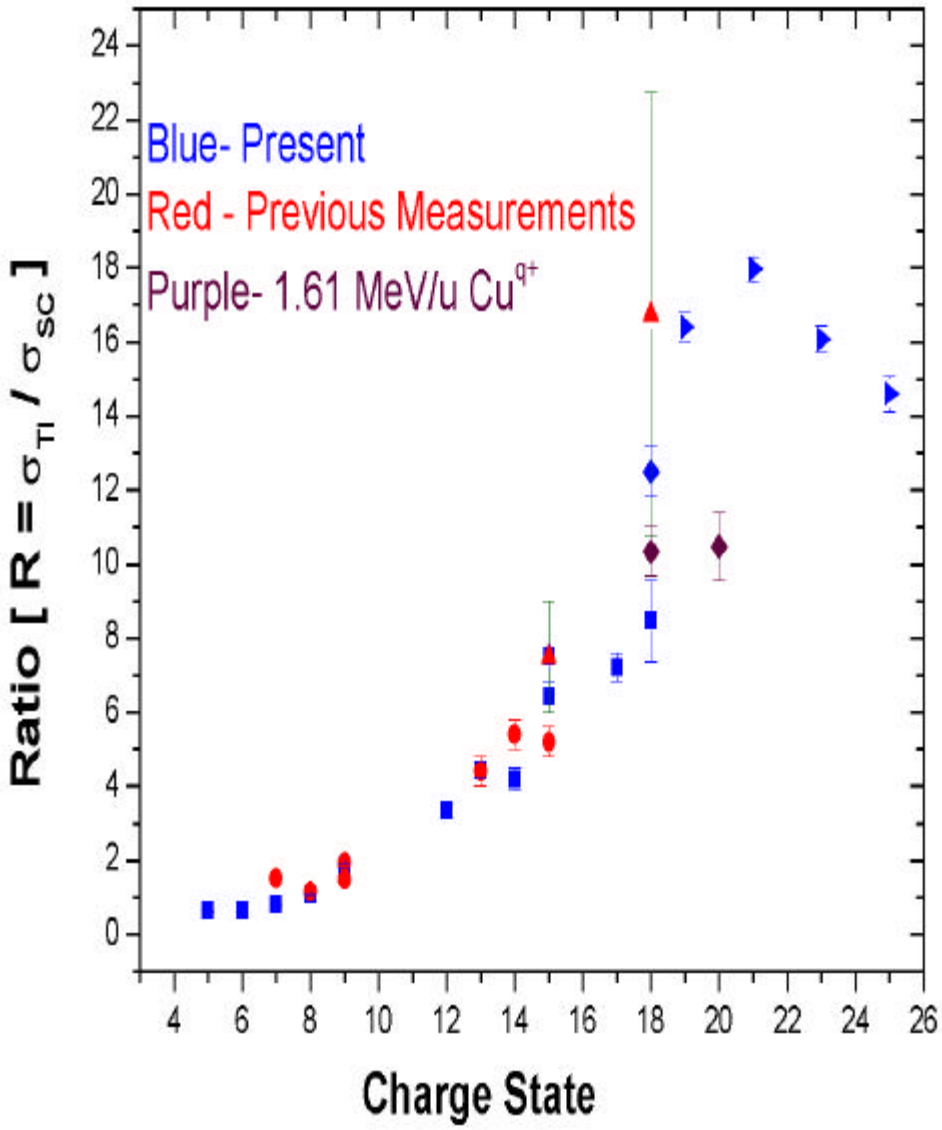
Blue- Present
Red - Previous Measurements
Purple- 1.61 MeV/u Cu^{q+}
Ratio [R = σ_{TI} / σ_{SC}]
Charge State
0
2
4
6
8
10
12
14
16
18
20
22
24
4
6
8
10
12
14
16
18
20
22
24
26

E. Mechanisms for Transfer ionization Ion-He Collisions

The process of removing two electrons from He by a charged ion has been studied for several years. One of the interesting questions is the behavior of the transfer ionization process, TI, in which the projectile captures one of the electrons and the other is emitted to the continuum. Several features existing in the data are not understood to date and to add intrigue to the problem, recent new data on H^+ + He showed a completely unexpected result at collision velocities above 4.0 au. Below 4 au the ratio of TI-to- SC, is flat at a value of ~2.5%. The new results[34] showed the ratio linearly increasing with velocity up to a value of ~4.4% in the range of 4.0 to 7.5 au. It was expected that the ratio would fall slowly with increasing velocity to the shake-off value of ~1.6%. The shake-off value is defined as the probability that a second electron will be lost by the He ion in its final state electronic readjustment following SC. The electron emission is due to the incomplete overlap of the wave function of the intermediate He^+ state with that of the He^+ ground state. We have studied the $\frac{s_{TI}}{s_{SC}}$ ratio for high velocity highly charged ions on He at velocities in the range of 6 to 10 au and observed, conversely, that the ratio is monotonically decreasing with velocity. If we assume that the two-electron removal from He is occurring by independent interactions with the projectile, the ratio of TI-to-SC is expected to vary as Z^2, where Z is the projectile charge. Using this assumption, we can compare our results for F^{9+} projectiles to that of H^+ on He by using the appropriate scaling as we did with He^{2+} + He scaling in the previous sections. These results can be seen in Fig. 4.25.

This was the status of the $\frac{s_{TI}}{s_{SC}}$ ratio until the summer of 2001, when Schmidt *et al.*[68] extended the H^+ + He measurements to higher velocity (V ~ 10 to 14 au) using the storage ring at Stockholm. Their results were reported at ICPEAC 2001 in Santa Fe. The value of the ratio is observed to decrease from ~4% to ~3% with velocity in the range of 10 au to 17 au. These latter results compare favorably with the behavior of our F^{9+} data. Earlier F^{9+} + He results from Shinpaugh *et al.*[38] show a turnover at lower energies similar

to the H^+ + He data at about 7 au. These data were not taken with the COLTRIMS method used by Mergel *et al.*[65], Unal *et al.*[71], and Schmidt *et al.*[68] and suffer from fairly large errors. For this reason they are not used in the comparison, however those data are very suggestive of a favorable comparison between the velocity dependence of H^+ + He to a scaled F^{9+} + He assuming an independent electron model. This suggests that we attempt the difficult measurements of F^{9+} + He at velocities below 6 au using our COLTRIMS apparatus. C. D. Lin and H. C. Tseng have performed coupled channel calculations for the energy dependence of TI and SC for F^{9+} + He and find values slightly higher than our measured values, but with approximately the same energy dependence (Fig. 4.25). We show this calculation scaled with the same formula as used for the experimental data. One of the difficulties of performing accurate calculations is the large basis set needed to properly describe the collision system.

The TI process can proceed via two independent e-projectile ion interactions as discussed above [sometimes referred to as kinematical TI or TS2 (two-step, two e-nuclear interactions)] or it can proceed via the Thomas scattering mechanism [sometimes referred to as e-e Thomas TI of TS1 (two-step, one e-nuclear interaction)]. The Thomas scattering mechanism transfers little momentum to the recoiling target nucleus, whereas kinematical SC transfers longitudinal momentum to the recoiling target nucleus. The same holds true for the corresponding TI processes. By using COLTRIMS one can separate the two TI processes based on the observed longitudinal momentum transfer to the recoiling target ion. Schmidt *et al.*[68] have done this for H^+ + He and reported that the e-e Thomas TI is 35% of the total TI. The e-e Thomas TI scattering becomes negligible for high Z projectiles due to the Z^2 scaling expected for the kinematical TI. The resulting kinematical $\frac{s_{TI}}{s_{SC}}$ ratio for H^+ + He then compares very favorably with the scaled $\frac{s_{TI}}{s_{SC}}$ ratio for F^{9+} + He in Fig. 4.25. Higher velocity data (V ~ 4.5 to 7 au) from Mergel *et al.*[65] are shown as solid squares and the F^{9+} + He data from Unal *et al.*[71] are shown as solid circles.

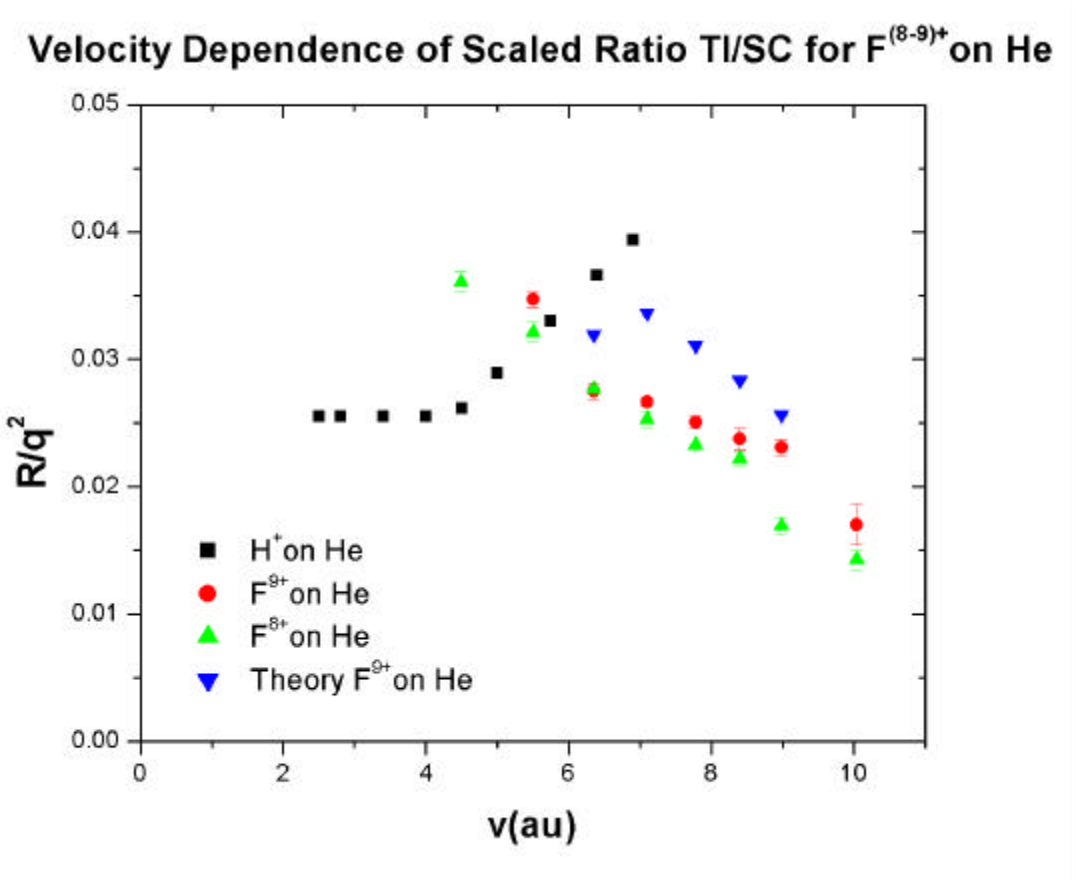

Fig. 4.25. Velocity dependence of scaled ratio of $\frac{s_{TI}}{s_{SC}}$ for H^+ on He and the scaled ratio of $\frac{s_{TI}}{s_{SC}}$ for $F^{(8\text{-}9)+}$ on He.

Fig. 4.26 shows the velocity dependence of scaled ratio for F^{9+} data according to $R(scaled) = \frac{R(measured) - R(shake)}{Z^2} + R(shake)$, where R (shake) is taken as the theoretical value. This formula is used since the shake-off limit is independent of projectile Z. This procedure brings the data a little more in line with H^+ + He data.

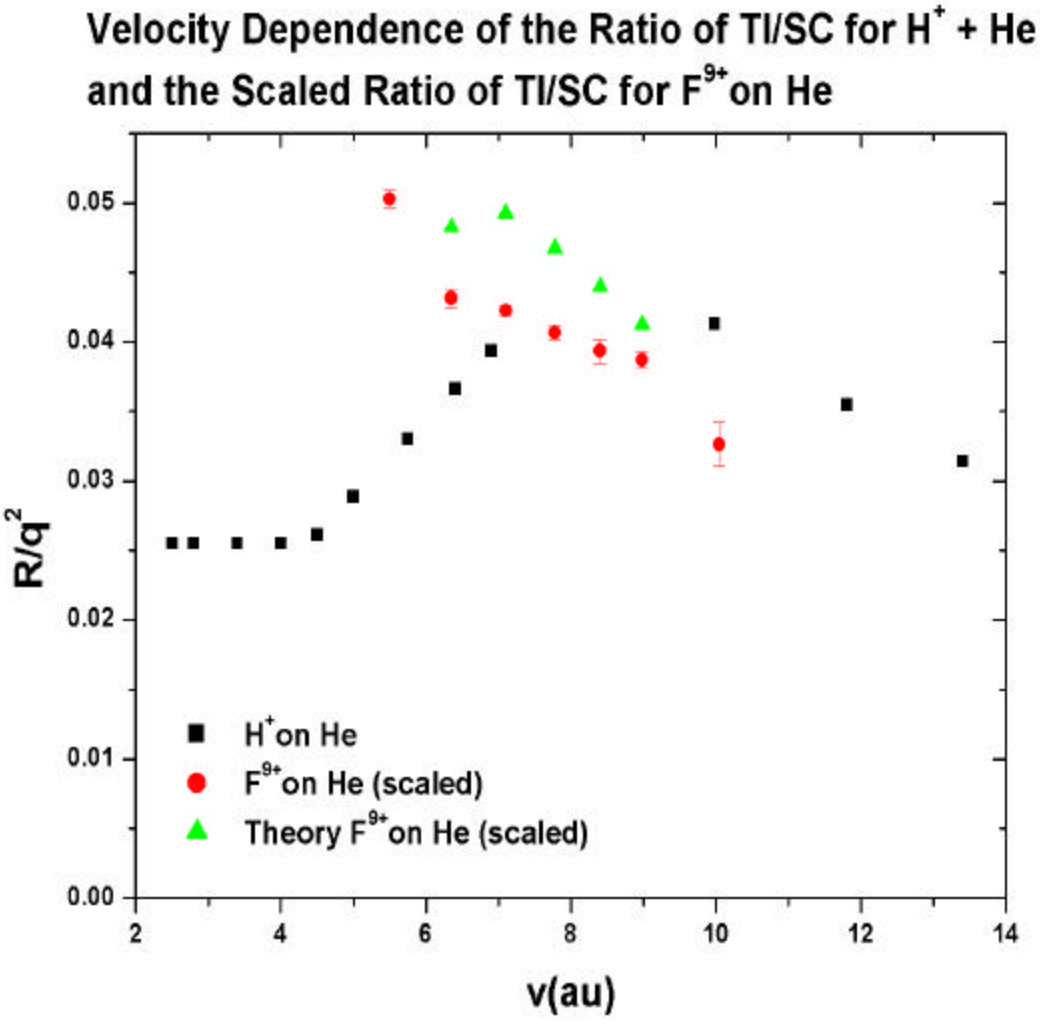

Fig. 4.26. Velocity dependence of scaled ratio of $\frac{s_{TI}}{s_{SC}}$ for H^+ on He and the scaled ratio of $\frac{s_{TI}}{s_{SC}}$ for F^{9+} on He with:

$$R(scaled) = \frac{R(measured) - R(shake)}{Z^2} + R(shake)$$

V. CONCLUDING REMARKS

The results reported in this dissertation were an important addition to the general understanding of the transfer ionization and single capture process in highly charged very fast ion-atom collisions. The charge state and energy dependences of Transfer Ionization (TI) and Single Capture (SC) processes in collisions of multiply charged ions with He from intermediate to high velocities are investigated using coincident recoil ion momentum spectroscopy. The simultaneous (coincident) detection of the momentum analyzed recoil ions gave this technique a unique power that enabled us to determine very accurate $\frac{s_{TI}}{s_{SC}}$ ratios. Our results are an important improvement over the previous measurements made by using gas cells. The present results are significantly higher than the measurements reported by Tanis *et al.*[48], Shinpaugh *et al.*[38], and Datz *et al.*[49] We have provided a very accurate set of $\frac{s_{TI}}{s_{SC}}$ ratio data to the scientific community.

The collision systems reported here are 1 MeV/u $O^{(4-8)+}$, 0.5-2.5 MeV/u $F^{(4-9)+}$, $Ti^{15,17,18+}$, 1.6-1.75 MeV/u $Cu^{18,20+}$ and 0.25-0.5 MeV/u $I^{(15-25)+}$ ions interacting with helium. We have also studied the $\frac{s_{TI}}{s_{SC}}$ ratio for high velocity highly charged ions on He at velocities in the range of 6 to 10 au and observed that the ratio is monotonically decreasing with velocity. Furthermore, we see a ratio that follows a q^2 dependence up to approximately q = 9. Above q = 9 the experiment exceeds the q^2 dependence prediction due to antiscreening. C. D. Lin and H. C. Tseng have performed coupled channel calculations for the energy dependence of TI and SC for F^{9+} + He and find values slightly higher than our measured values, but with approximately the same energy dependence. The big unanswered question here was the sudden fall in the TI/SC ratio for values of q above q = 20, as reported by Datz *et al.*[33] The new data, Si, Ti and Cu, go up only to q = 20 and show a smooth monotonically increasing TI/SC ratio. The new data points for $Ti^{15,17,18+}$ have smaller errors, and when combined with the $Cu^{18,20+}$ reflect a more gently increasing behavior than might be inferred from the earlier Ti data.

Present measurements for I^{q+} suggest that the ratio is energy dependent contrary to the Datz *et al*.[33] data where they observed almost no difference in the ratio between the 0.1 and 0.25 MeV/u I^{q+} cases.

We have compared our results for F^{9+} projectiles to that of H^+ on He by using the appropriate scaling by assuming that the two-electron removal from He is occurring by independent interactions with the projectile. Schmidt *et al*.[52] reported that the value of the ratio is observed to decrease from ~4 % to ~3% with velocity in the range of 10 au to 17 au. These latter results compare favorably with the behavior of our F^{9+} data. Earlier F^{9+} + He results from Shinpaugh *et al*.[22] show a turnover at lower energies similar to the H^+ + He data at about 7 au. However, these data were not taken with the COLTRIMS method and suffer from fairly large errors.

Since the TI process can proceed via two independent e-projectile ion interactions as discussed before, by using COLTRIMS one can separate the two TI processes based on the observed longitudinal momentum transfer to the recoiling target ion. Schmidt *et al*.[52] have separated two independent e-projectile ion interactions in the TI process as discussed before, by using COLTRIMS for H^+ + He and reported that the e-e Thomas TI is 35% of the total TI. The e-e Thomas TI scattering becomes negligible for high Z projectiles due to the Z^2 scaling expected for the kinematical TI. The resulting kinematical $\frac{s_{TI}}{s_{SC}}$ ratio for H^+ + He then compares very favorably with the scaled ratio for F^{9+} + He.

On the experimental technique aspect, I want to mention the power of the recoil ion momentum spectroscopy and how details of the experimental setup have contributed to the accuracy of present results. The collision chamber is commissioned on the 15-degree port of a switching magnet, which allows the delivery of a beam with very little impurity. The target was provided using a supersonic He jet with a two-stage collimation. The two-stage, geometrically cooled, supersonic He jet has significantly reduced the background contribution to the spectrum compared to a single stage He jet. In the case of a differentially pumped gas cell complex calculations based on assumptions for the

correction due to the collisions with the contaminant beam led to corrections, which were up to 50%. The new setup allows one to make direct separation of contaminant processes in the experimental data using the longitudinal momentum spectra. Furthermore, this correction is much smaller (about 8.8%) yielding better overall precision.

In conclusion, further studies are needed to fully understand the transfer ionization mechanisms for fast highly charged projectile ions through kinematically complete experiments, where both recoil ion and electron momentum are measured simultaneously.

References

1. G. H. Henderson, Proc. R. Soc. London A **102**, 496 (1922).
2. A. S. Schlachter, J. W. Stearns, W. G. Graham, K. H. Berkner, R. V. Pyle and J. A. Tanis, Phys. Rev. A **27**, 3372 (1983).
3. H. Knudsen, H. K. Haugen, and P. Hvelplund, Phys. Rev. A **23**, 597 (1981).
4. H. Knudsen, L. H. Andersen, P. Hvelplund, J. Sorensen, and D. Ciric, J. Phys. B: At. Mol. Phys. **20**, L253-L257 (1987).
5. R. Bartiromo, in *Diagnostics for Fusion Reactor Condition, Proceedings of the International School of Plasma Physics*, edited by P. E. Stott, D. K. Akulina, G. G. Leota, E. Sindoni, and C. Wharton (Pergamon, New York, 1982).
6. G. Steigman, Astrophys. J. **199**, 642 (1975).
7. H. S. W. Massey, and E. H. S. Burhop, Electronic and Ionic Impact Phenomena, Clarendon Press Oxford (1952).
8. S. K. Allison, Rev.Mod. Phys. **30**, 1137.
9. S. K. Allison and M. Garcia-Munoz, in D. R. Bates, Ed., *Atomic and Molecular Process*, Academic Press, New York (1962).
10. J. B. Hasted, Physics of Atomic Collisions, Butterworth, London (1964).
11. H.-D. Betz, Rev. Mod. Phys. **44**, 465 (1972).
12. H. Tawara, and A. Russek, Rev. Mod. Phys. **45**, 178 (1973)
13. H. S. W. Massey, and H. B. Gilbody, *Electronic and Ionic Impact Phenomena*, **Vol. 4**, Clarendon Press, Oxford (1974).
14. H. B. Gilbody, Adv. At. Mol. Phys. **22**, 143 (1986).
15. B. H. Bransden and M. R. C. McDowell, *Charge Exchange and the Theory of Ion Atom Collisions*, Oxford University Press, New York (1992).
16. N. V. Federenko and V. V. Afrosimov, Sov. Phys.-Tech. Phys. **1**, 1872 (1956).
17. E. Everhart and Q. C. Kessel, Phys. Rev. Lett., **14**, 247 (1965).
18. Q. C. Kessel and E. Everhart, Phys. Rev., **146**, 16 (1966).
19. J. W. McConkey, A. Crowe and M. A. Hender, Phys. Rev. Lett. **29**, 1 (1972).

20. J. Ullrich,M. Horbatsch, V. Dangendorf, S. Kelbch and H. Schmidt-Bocking, J. Phys. B: At. Mol. Opt. Phys., **21**, 611 (1988)

21. J. Ullrich, H. Schmidt-Bocking and C. Kelbch, Nucl. Instrum. Method. A, **268**, 216 (1988).

22. J. Ullrich , R. Dorner, S. Lencinas, O. Jagutzki and H. Schmidt-Bocking, Nucl. Instrum. Method. B, **61**, 415 (1991).

23. W. Wu, J. P. Giese, Z. Chen, R. Ali, C. L. Cocke, P. Richard and M. Stockli, Phys. Rev. A., **50**, 502 (1994)

24. W. Wu, C. L. Cocke, J. P. Giese, F. Melchert, M. L. A. Raphaelian, and M. Stockli, Phys. Rev. Lett., **72**, 3170 (1994).

25. R. Ali, V. Frohne,C. l. Cocke, M. Stockli, S. Cheng and M. L. A. Raphaelian, Phys. Rev. Lett., **69**, 2491 (1992).

26. C. L. Cocke and R. E. Olson, Phys. Rep., **205**, 155 91991).

27. V. Frohne, S. Cheng, R. Ali, M. L. A. Raphaelian, C. L. Cocke and R. E. Olson, Phys. Rev. Lett., **71**, 696 (1993).

28. V. Frohne, S. Cheng, R. Ali, M. L. A. Raphaelian, C. L. Cocke and R. E. Olson, Phys. Rev. A **53**, 2407 (1996).

29. J. C. Levin, R. T. Short, S. B. Elston, J. P. Gibbons, I. A. Selin and H. Schmidt-Bocking, Phys. Rev. A **36**, 1649 (1987).

30. J. P. Grandin, D. Hennecart, X. Husson, D. Lecler, I. Lesteven-Vaisse and D. Lisfi, Europhys. Lett., **6**, 683 (1988).

31. J. Ullrich , R. Moshammer,R. Dorner, O. Jagutzki , V. Mergel, H. Schmidt-Bocking and L. Spielberger, J. Phys. B: At. Mol. Opt. Phys. **30**, 2917 (1997).

32. W. Wu, K. L. Wong, C. L. Cocke, J. P. Giese and E. C. Montenegro, Phys. Rev. A **51**, 3718 (1995).

33. R. Moshammer, J. Ullrich, M. Unverzagt, W. Schmidt, P. Jardin, R. E. Olson, R. Dorner, V. Mergel and H. Schmidt-Bocking, Nucl. Instrum. Method. B **107**, 62 (1996).

34. V. Mergel, PhD Thesis, Johann-Wolfgang-Goethe Universitat Frankfurt, ISBN 3-8265-2067-X (1997).

35. R. Moshammer, M. Unverzagt, W. Schmidt, J. Ullrich and H. Schmidt-Bocking, Nucl. Instrum. Method. B **108**, 425 (1996).
36. W. Wu, Ph.D. dissertation, Kansas State University, 1994.
37. H. Knudsen, L. H. Andersen, P. Hvelplund, G. Astner, H. Cederquist, H. Danared, K. Liljeby and K.-G. Rensfelt, J. Phys. B **17**, 3545 (1984).
38. J. L. Shinpaugh, J. M. Sanders, J. M. Hall, D. H. Lee, H. Schmidt-Bocking, T. N. Tipping, T. J. M. Zouros and P. Richard, Phys. Rev. A **45**, 2922 (1992).
39. Y. Kaneko, T. Iwai, S. Ohtani, K. Okuno, N. Kobayashi, S. Tsurubuchi, M. Kimura, H. Tawara and S. Takagi, in *Abstracts of the 12th Int. Conf. on the Physics of Electronic and Atomic Collisions*, edited by S. Datz, (North Holland, Amsterdam, 1982), p. 696.
40. R. Hippler, S. Datz, P. D. Miller, P. L. Pepmiller and P. F. Dittner, Phys. Rev. A **35**, 585 (1987).
41. T. Iwai, Y. Kaneko, M. Kimura, N. Kobayashi, S. Ohtani, K. Okuno, S. Takagi, H. Tawara and S. Tsurubuchi, Phys. Rev. A **26**, 105 (1982).
42. S. Bliman, D. Hitz, B. Jacquot, C. Harel, and A. Salin, J. Phys. B **16**, 2849 (1983).
43. J. A. Guffey, L. D. Ellsworth, and J. R. Macdonald, Phys. Rev. A **15**, 1863 (1977).
44. V. V. Afrosimov, A. A. Basalaev, E. D. Donets, K. O. Lozhkin and M. N. Panov, in *Abstracts of the 12th Int. Conf. on the Physics of Electronic and Atomic Collisions*, edited by S. Datz, (North Holland, Amsterdam, 1982), p. 690.
45. E. Horsdal Pederson and L. Larsen, J. Phys. B **12**, 4085 (1979).
46. M. B. Shaw and H. B. Gilbody, J. Phys. B **18**, 899 (1985); **15**, 413 (1982); **14**, 2361 (1981).
47. J. H. McGuire, E. Salzborn and A. Muller, Phys. Rev. A **35**, 3265 (1987)
48. J. A. Tanis, M. W. Clark, R. Price and R. E. Olson, Phys. Rev. A **36**, 1952 (1987).

49. S. Datz, R. Hippler, L. H. Andersen, P. F. Dittner, H. Knudsen, H. F. Krause, P. D. Miller, P. L. Pepmiller, T. Rosseel, R. Schuch, N. Stolterfoht, Y. Yamazaki, and C. R. Vane, Phys. Rev. A **41**, 3559 (1990).
50. E. C. Montenegro, K. L. Wong, W. Wu, P. Richard, I. Ben-Itzhak, C. L. Cocke, R. Moshammer, J. P. Giese, Y. D. Wang, and C. D. Lin, Phys. Rev. A **55**, 2009 (1997).
51. R. Shingal and C. D. Lin, J. Phys. B **24**, 251 (1991).
52. V. V. Afrosimov, Yu. A. Manaev, M. N. Panov, and V. Uroshevich, Sov. Phys.-Tech. Phys. **12**, 512 (1967).
53. V. V. Afrosimov, Yu. A. Manaev, M. N. Panov, and N. V. Federonko, Sov. Phys.-Tech. Phys. **14**, 109 (1969).
54. V. V. Afrosimov, G. A. Leiko, Yu. A. Manaev, and M. N. Panov, Sov. Phys.-JETP. **40**, 661 (1975).
55. R. D. DuBois, Phys. Rev. A **33**, 1595 (1986).
56. A. Niehaus, Comments At. Mol. Phys. **9**, 153 (1980).
57. C. L. Cocke, R. DuBois, T. J. Gray, E. Justiniano, and C. Can, Phys. Rev. Lett. **46**, 1671 (1981).
58. L. H. Andersen, M. Frost, P. Hvelplund, H. Knudsen, and S. Datz, Phys. Rev. Lett. **52**, 518 (1984).
59. J. H. McGuire, *Electron Correlation Dynamics in Atomic Collisions* (Cambridge University, Cambridge, England, 1997).
60. A. Lahmam-Bennani *et al*., Phys. Rev. A **59**, 3548 (1999).
61. L. H. Thomas, Proc. Roy. Soc. London, Ser. A **114**, 561 (1927).
62. E. Horsdal-Pederson, C. L. Cocke, and M. Stockli, Phys. Rev. Lett. **50**, 1910 (1983).
63. J. Palinkas *et al*., Phys. Rev. Lett. **63**, 2464 (1989).
64. R. Gayet and A. Salin, Nucl. Instrum. Methods Phys. Res., Sect. B **56/57**, 82 (1991).
65. V. Mergel, Ph. D. thesis, Universitat Frankfurt, Shaker Verlag, 1996.
66. J. S. Briggs and K. Taulbjerg, J. Phys. B **12**, 2565 (1979).
67. T. Ishihara and J. H. McGuire, Phys. Rev. A **38**, 3310 (1988).

68. H. T. Schmidt et al., Abstracts of Contributed Papers of XIII-ICPEAC 2001, Santa Fe, NM, (Rinton Press) p.439.

69. V. Mergel, R. Dorner, Kh. Kayyat, M. Achler, T. Weber, O. Jagutzki, H. J. Ludde, C. L. Cocke, and H. Schmidt-Bocking, Phys. Rev. Lett. **86**, 2257 (2001).

70. K. L. Wong *et al*., J. of Phys. B. **29**, L209 (1996).

71. R. Unal *et al*., AIP Conference Proceedings of CAARI 2000, Denton, TX, Vol. **576**, 36 (2001).

72. W. C. Wiley and I. H. McLaren, The Review of Scientific Instruments, **26**,1150 (1955).

73. T. R. Dillingham, J. R. Macdonald, and Patrick Richard, Phys. Rev. A **24**, 1237 (1981).

74. XSYS/IUCF Data Acquisition Software, Indiana university Cyclotron Facility, Bloomington, IN 47405.

75. Idaho National Engineering Laboratory, EG&G Idaho, Inc. Idaho Falls, ID 83415.

Appendix A
Calibration of the Detector

We have performed a series of measurements on the recoil detector in order to characterize the detector and the gas jet. A well-regulated mask was placed in front of the detector as shown in Fig. 3.5.A. Fig. 3.5.B shows the image of the mask, as seen on the two-dimensional position sensitive detector (2D PSD). These data allow us to determine the spatial resolution of the detector.

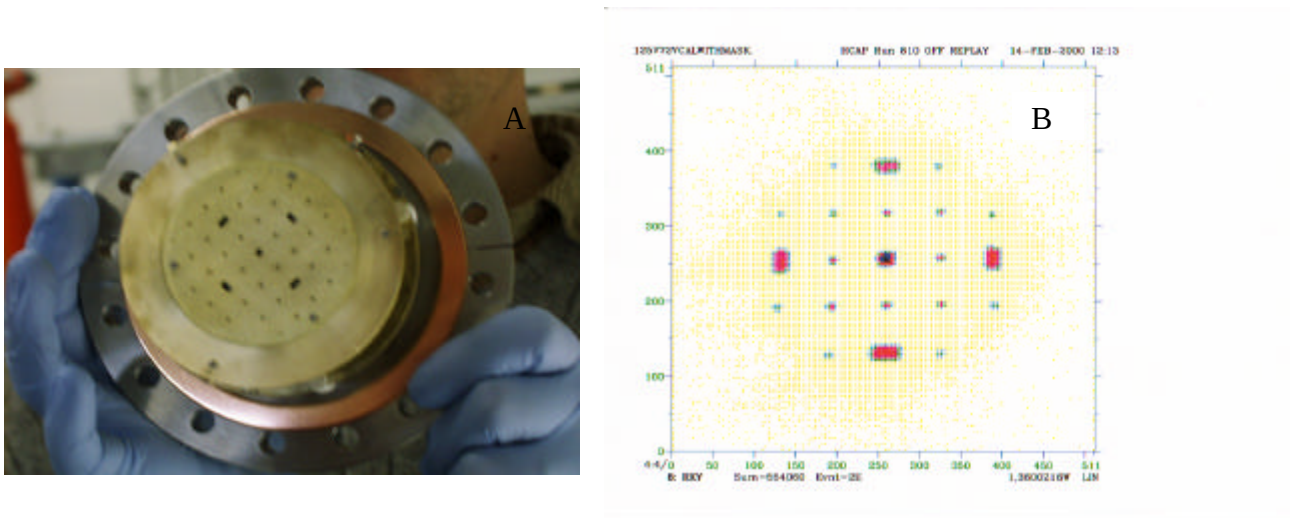

Fig. 3.5. The calibration of the 2DPSD. (A) is the picture of a metal mask and (B) is the image of this mask as seen by the detector. Note this analysis is based on a 512 by 512 2-D spectrum.

The next step was to take a downward projection of this image for a given slice in the vertical direction. Since we know the physical distance between the holes on the mask, we can assign the corresponding channel numbers in the downward projection of the image Fig. 3.5.B, as shown in Fig. 3.6.A, to a known distance.

It is found that 14.7 mm on the detector corresponds to 139 channels.

$$\frac{\Delta S}{\Delta C} = \frac{14.7mm}{139Ch} = 0.106\, mm/Ch \qquad \text{Eq. 3.1}$$

By using the full width at half maximum (FWHM) of the edges of the central region obtained by taking the derivative of the number of counts per channel as shown in Fig. 3.6.B, we are able to obtain the following:

$$\left(FWHM\right)_{av} = 7.76Ch\ .$$

We are then able to obtain the position resolution of the detector.

$$\mathrm{Re}\,s. \approx FWHM \times \frac{\Delta S}{\Delta C} \qquad \text{Eq. 3.2}$$

$$\mathrm{Re}\,s. \approx 0.82mm$$

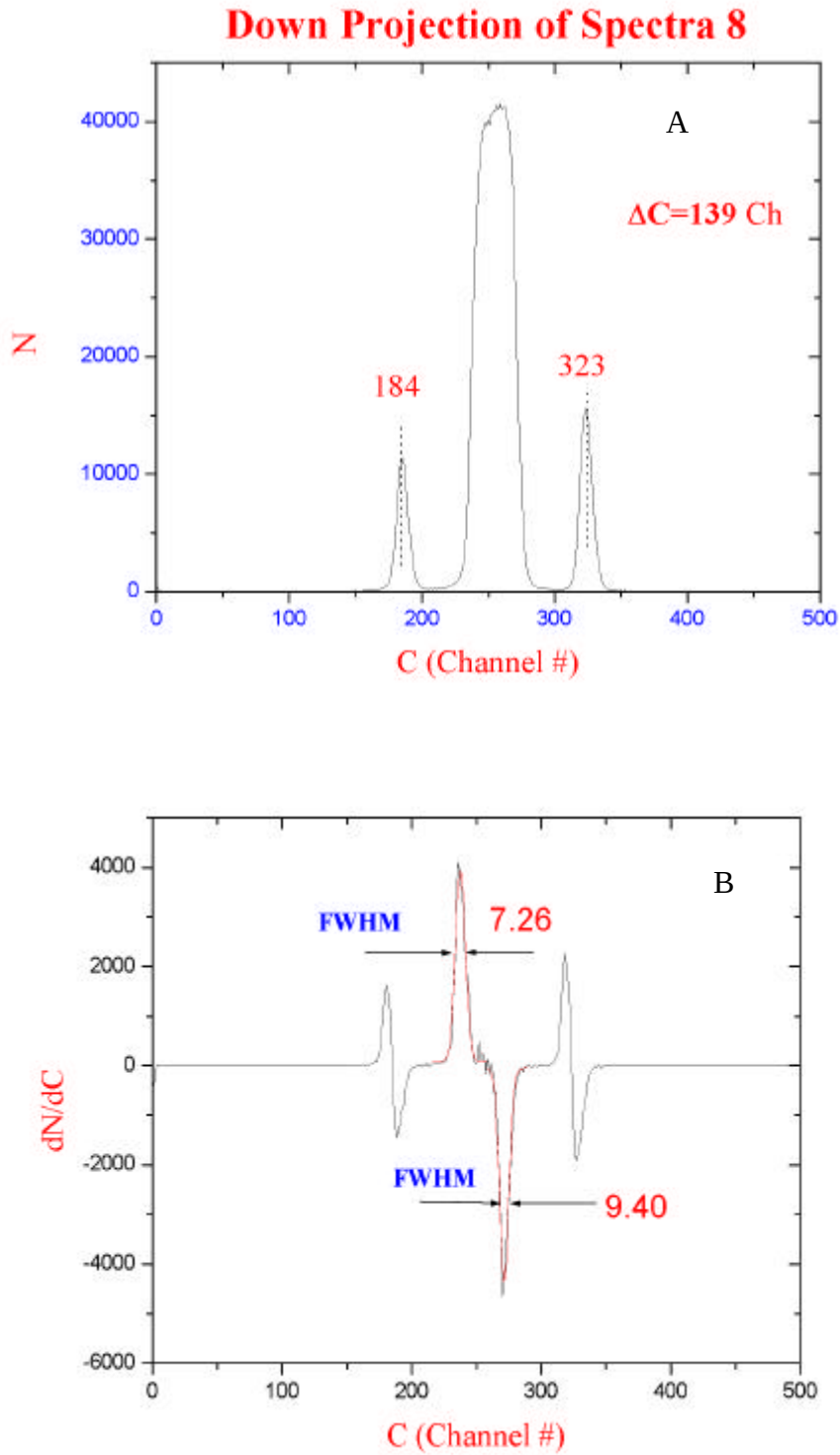

Fig. 3.6 Downward projection of the image obtained from the mask (A) and its derivative (B).

After the detector spatial calibration, the mask was removed and several test runs with different extraction voltage settings were made in order to characterize the jet. Table 3.1 shows the test runs and their results.

Table 3.1 Test run results for 1 MeV/u F^{7+} on He in order to calculate the jet speed.

Run #	Extraction Voltages Pusher	Time of Flight for He^+	Peak Positions (Ch. #) y	z
436	500 V	5.934×10^{-6} s	400	231
437	750 V	4.847×10^{-6} s	387	232.5

Since we know the detector calibration, time of flight of the He^+ recoil ions for different extraction voltages and corresponding jet positions on the detector, we can easily calculate the jet speed as following.

$$v_{JET} = \frac{\Delta y}{\Delta T} \qquad \text{Eq. 3.3}$$

where $\Delta y = (y_{500} - y_{750}) \times Cal.Con = (400 - 387) \times 0.106 = 1.378mm$

We found the jet speed to be ~1267 m/s, which is a supersonic speed. No correction due to any contribution from a $\vec{v} \times \vec{B}$ due to stray magnetic fields was made. The difference in the deflection in the z-direction indicate an error in the range of 10% due to the magnetic fields, assuming the component of the **B** field perpendicular to $\vec{v}$ makes an angle of ~45^0 to the y axis.

We also converted this number into momentum:

$$P_{JET} = m \times v_{JET} = 4.27au \qquad \text{Eq. 3.4}$$

The z-component of the momentum of He^+ is obtained similarly and found to be:

$$P_z = m_{He} \cdot v_z = m_{He} \cdot \left[(Ch_z - Ch_{z_0}) \times \frac{\Delta S}{\Delta C} \times \frac{1}{T_{He^+}} \right] \qquad \text{Eq. 3.5}$$

From Eq. 3.5 one can easily show that conversion from channel numbers to momentum is $P_z = (Ch_z - Ch_{z_0}) \times 0.0981$ in au for He^+ for this calibration.

Appendix B

Shown below are the spectrometer dimensions that are used in the experiment.

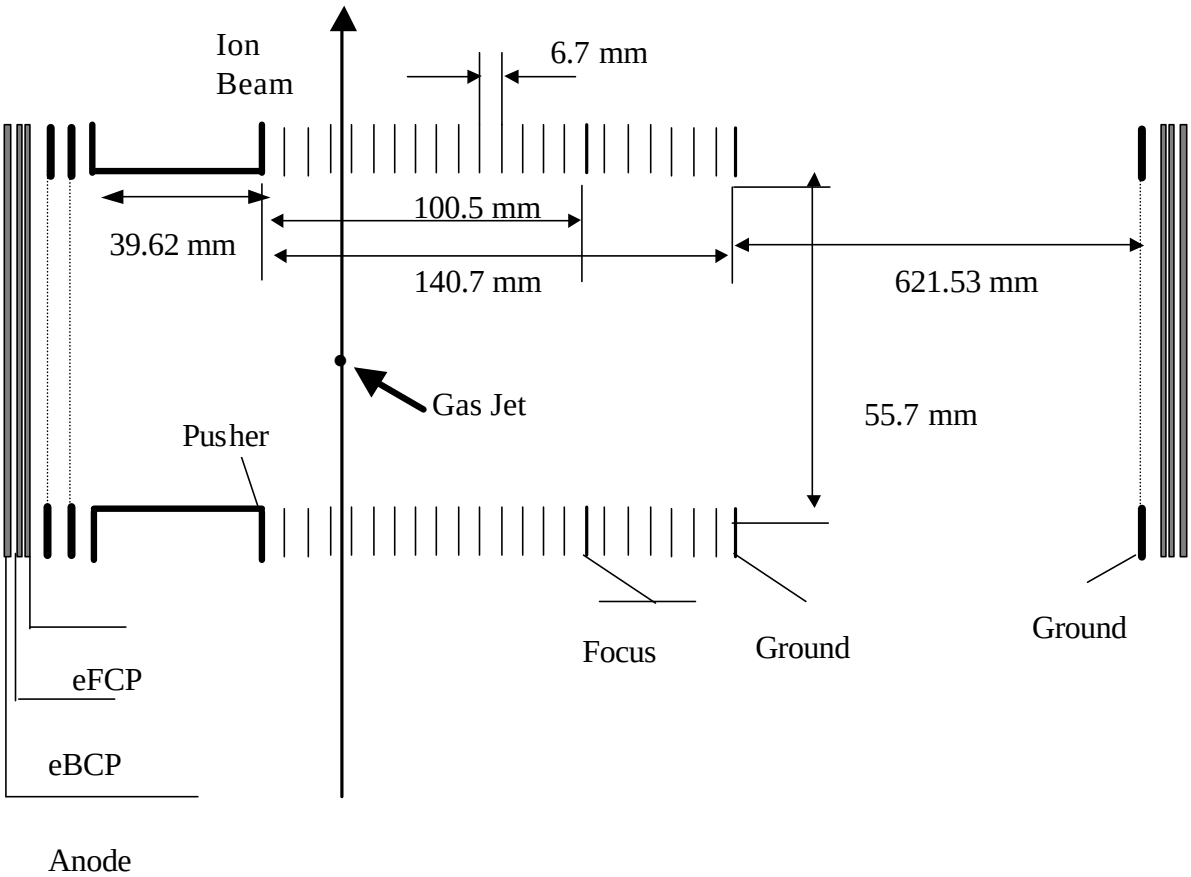

Simion[74] calculated time-of-flights for different pusher and focus voltages

Pusher (V)	Focus (V)	T (He^{+}, ms)	T (He^{2+}, ms)
1500	852	3.639	2.573
1000	568	4.456	3.151
750	429	5.151	3.642
500	285	6.305	4.459
250	142	8.913	6.302
200	114	9.970	7.050
125	72	12.63	8.931
70	40	16.86	11.92

Appendix C

Data Acquisition and Analysis Code

Data were read and stored in a list mode. In this mode every single event is stored separately, which allows one not only to rerun the experiment, but also impose different conditions to the data during data analysis.

The software XSYS[74] was used to collect (online) and to analyze (offline) the data. The two files, “.com and .evl”, were used in the data reading and analyses of the data. The filename.com file allocates the memory, specifies the areas and gates to be generated and used to store and analyze the data. The filename.evl contains the code for processing the signals through the computer.

In this appendix, one may find the code that we have used for collecting and analyzing the data.

```
$!################TRANION.COM ################
$!
$!              By Ridvan Unal modified from prev versions
$!       COM FILE FOR Transfer Ionization @ linac EXPERIMENT
$!
$ DMEM ALL GLOBAL FILE
$ AMEM NEW 30000 PAGES*
$!-------------------------------Recoil detector---------
$ AMEM   1   XR        2048
$ AMEM   2   YR        2048
$ AMEM   3   RR        2048
$ AMEM   4   SUMR      2048
$ AMEM   6   RXX       512        !128
$ AMEM   7   RYY       512        !128
$ AMEM   8   RXY       512 512    !128 128

$!----------------------Gated----Recoil detector---------
$ AMEM   31   gXR       2048
$ AMEM   32   gYR       2048
$ AMEM   33   gRR       2048
$ AMEM   34   gSUMR     2048
$ AMEM   36   gRXX      512      !128
$ AMEM   37   gRYY      512      !128
$ AMEM   38   gRXY      512 512 !128 128
$!----------------------Gated----Recoil detector---------
$ AMEM   51   g2XR       2048
$ AMEM   52   g2YR       2048
$ AMEM   53   g2RR       2048
$ AMEM   54   g2SUMR     2048
$ AMEM   56   g2RXX      512     !128
$ AMEM   57   g2RYY      512     !128
$ AMEM   58   g2RXY      512 512         !128 128
!----------------------Gated----Recoil detector---------
$ AMEM   61   g3XR       2048
$ AMEM   62   g3YR       2048
$ AMEM   63   g3RR       2048
$ AMEM   64   g3SUMR     2048
$ AMEM   66   g3RXX      512     !128
$ AMEM   67   g3RYY      512     !128
$ AMEM   68   g3RXY      512 512         !128 128
$!-------------------------------Position vs TAC----------
$ AMEM   11  RXTAC       512 2048        !128 2048
$ AMEM   12  RXTAC2      512 512         !128 128
$!-------------------------------TAC spec.--------------
$ AMEM  41   TACPR       2048            ! electron recoil TAC
$ AMEM  42   TACPR2      512 !128
$ AMEM  100  HiRes       512
$ AMEM  101  HIRERAN     512
$ AMEM  102  HIRERAN1    512
$ AMEM  141  TACg10      2048
$!-----------------------------Work space collection-------
$ AMEM  800  RANSUM              512 512
$ AMEM  801  PRORANSCDO          512
$ AMEM  805  NETCAP              512 512
$ AMEM  810  PROCAPDO            512
$ AMEM  815  PROCAPAC            512
$ AMEM  820  PROSPEC             512
$ AMEM  838  PROTOTSPECDO        512
$ AMEM  900  RANSUMTI            512 512
$ AMEM  901  PRORANTIDO          512
```

```
$ AMEM  905  NETTI              512 512
$ AMEM  910  PROTIDO            512
$ AMEM  915  PROTIAC            512
$ AMEM  920  PROJGSPECT         512
$ AMEM  938  PROSPECDO          512
$!--------------------------Gated TAC spec.---------------
$ Clear Flags
$ Gate New
$ Gate
$ tdg alloc 10 g10 spec 8
$ Gate 41 3
$ CLEAR ALL
```

```
!
!####################HCAP.EVL#####################
!              Modified by Ridvan Unal from
!EVL FILE FOR SOFT ELECTRONS FROM D2 EXPERIMENT AT LINAC
!
!Allen Landers & Mahendrajit Singh
!Aug. 25 1997
!!!!!!!!!!!!!!!!!PARAMETERS AND VARIABLES!!!!!!!!!!!!!!!!!!!

!------------REC. DET.--------------
        REAL OFF=10
        REAL RTHS=10
        REAL RTHH=2040
        REAL RGX=1
        REAL RGY=1
        REAL RGR=1
        REAL RCH=250
        REAL RAMPX=1.0
        REAL RAMPY=1.0
        REAL RXSH=0.0
        REAL RYSH=0.0
        REAL RFACTOR=2.0
        REAL SRXF        ! Recoil Signals after Offset
        REAL SRYF        ! and Gains have been applied
        REAL SRRF        !
        REAL RV1         !
        REAL RV2         !
        REAL RV3         !
        REAL RS          ! Recoil Signal Sum/3
        REAL RIX7        ! Recoil "X" Position (along beam) real
        INTEGER RIX      ! Recoil "X" Position (along beam)
        REAL RIY7        ! Electron "Y" Position (perp. to beam) real
        INTEGER RIY      ! Recoil "Y" Position (perp. to beam)
        INTEGER RIXIY    ! Recoil 2D Position for 2D Spectrum
!
!--------------Recoil Matrix Variables---------
        REAL Temp1
        REAL Temp2
        REAL M11=1
        REAL M12=-.003
        REAL M13=-.08
        REAL M21=-.002
        REAL M22=.99
        REAL M23=-.08
        REAL M31=-.10
        REAL M32=-.10
        REAL M33=1.07
        REAL MRX
        REAL MRY
        REAL MRR
!

!--------------REC. DET. ----------------
        REAL RT=0.0              !ANGLE OF ROTATION FOR REC. DET.
        REAL SINRT
        REAL COSRT
        REAL X1SINRT
        REAL X1COSRT
        REAL RX0=256
        REAL RY0=256
```

```
        REAL RX1
        REAL RY1
        REAL RX2
        REAL RY2
        REAL RX3
        REAL RY3

        Integer RIxres
!------------TACS--------------------------
        REAL TACPRL=-10.0
        REAL TACPRH=2048.0

!----------GENERAL PURPOSE PARAMETERS----------
        INTEGER SEED
        REAL RanNum1                    !Random number between 0 & 1
        REAL RanNum2                    !Random number

!================ SORTING==========================
        OPTION ALLSPEC
        OPTION TAPE
!
        FORMAT STACPR 1 12 1     ! TACER,  Recoil's TAC
        FORMAT STACPR2 1 12 5    ! TACER/8
        FORMAT SRX    2 12 1
        FORMAT SRY    3 12 1
        FORMAT SRR    4 12 1
!
                EVENT 2

        IF STACPR GT TACPRH EXIT
        IF STACPR LT TACPRL EXIT
        IF SRX GT RTHH EXIT
        IF SRY GT RTHH EXIT
        IF SRR GT RTHH EXIT
TAPE
!===============CORRECTION FOR GAINS AND OFFSETS============
!-----------REC. DET.----------------
        GET SRX
        SUB OFF
        MUL RGX
        STA MRX
                GET SRY
                SUB OFF
                MUL RGY
                STA MRY
        GET SRR
        SUB OFF
        MUL RGR
        STA MRR

!--------RECOIL MATRIX MULTIPLICATION-----
        LDA MRX
        MUL M11
        STA TEMP1
        LDA MRY
        MUL M12
        STA TEMP2
        LDA MRR
        MUL M13
        ADD TEMP1
```

```
        ADD TEMP2
        STA SRXF
        STA RV1
                LDA MRX
                MUL M21
                STA TEMP1
                LDA MRY
                MUL M22
                STA TEMP2
                LDA MRR
                MUL M23
                ADD TEMP1
                ADD TEMP2
                STA SRYF
                STA RV2
        LDA MRX
        MUL M31
        STA TEMP1
        LDA MRY
        MUL M32
        STA TEMP2
        LDA MRR
        MUL M33
        ADD TEMP1
        ADD TEMP2
        STA SRRF
        STA RV3

!
!============================DIVISIONS=========================
!--------------REC. DET.-------------
        LDA RV3
        MUL RFACTOR
        ADD RV1
        ADD RV2
        DIV 3.0
        STA RS
    IF RS LT RTHS EXIT
                LDA RV1
                MUL RCH
                DIV RS
                DIV 3.0
                MUL RAMPX
                SUB RXSH
                STA RIX7
                FIX
                STA RIX
        LDA RV2
        MUL RCH
        DIV RS
        DIV 3.0
        MUL RAMPY
        SUB RYSH
        STA RIY7
        FIX
        STA RIY

!
!===================DETECTORS ROTATIONS===================
!
```

```
!---------------------REC. DET.------------------------
        LDA RIX7
        SUB RX0
        STA RX1
                LDA RIY7
                SUB RY0
                STA RY1
        LDA RT
        SIN
        STA SINRT
                LDA RT
                COS
                STA COSRT
        LDA RX1
        MUL COSRT
        STA X1COSRT
        LDA RY1
        MUL SINRT
        ADD X1COSRT
        STA RX2
                LDA RX1
                MUL SINRT
                STA X1SINRT
                LDA RY1
                MUL COSRT
                SUB X1SINRT
                STA RY2
        LDA RX2
        ADD RX0
        STA RX3
        STA RIX7
        FIX
        STA RIX
                LDA RY2
                ADD RY0
!               IF LT 0 EXIT
                STA RY3
                STA RIY7
                FIX
                STA RIY
LDA RIx7
MUL 4
STA RIxres

LDA RIX7
MUL 4
STA RIx1res

LDA RIX7
MUL 4
STA RIX2res
!=====================SPECTRA INCREMENTS==================
!

!-----------TACS-------------
TINC STACPR TACPR                       !  Increment Raw Electron and
TINC STACPR2 TACPR2                     !  Recoil TACS
!---------REC.----------------
TINC SRXF XR                            !  Increment Raw Recoil Signals
TINC SRYF YR                            !  and Position Spectra
```

```
TINC SRRF RR                                !
TINC RS SUMR                                !
TINC RIX RIY RXY                                    !
STA RIXIY                                   !  Store Recoil Position for Gate
TINC RIX RXX                                !
TINC RIY RYY                                !
!---------------RX vs TAC-----------------
TINC RIX STACPR RXTAC
TINC RIX STACPR2 RXTAC2
!---------------GATES---------------------
        SPEC TACPR
                GATE G1 TACPR 1
                GATE G2 TACPR 2
                GATE G3 TACPR 3
!---------------Gated Spectra Increment----------------
!
If Stacpr g1 then
        TINC SRXF gXR                       !  Increment Gated Recoil Signals
        TINC SRYF gYR                       !  and Position Spectra
        TINC SRRF gRR                       !
        TINC RS gSUMR                       !
        TINC RIX RIY gRXY                   !
        TINC RIX gRXX                       !
        TINC RIY gRYY                       !
        TINC RIxres hires
Endif
If Stacpr g2 then
        TINC SRXF g2XR                      !  Increment Gated Recoil Signals
        TINC SRYF g2YR                      !  and Position Spectra
        TINC SRRF g2RR                      !
        TINC RS g2SUMR                      !
        TINC RIX RIY g2RXY                  !
        TINC RIX g2RXX                      !
        TINC RIY g2RYY
        TINC RIX2res HIRERAN1               !
Endif

If Stacpr g3 then
        TINC SRXF g3XR                      !  Increment Gated Recoil Signals
        TINC SRYF g3YR                      !  and Position Spectra
        TINC SRRF g3RR                      !
        TINC RS g3SUMR                      !
        TINC RIX RIY g3RXY                  !
        TINC RIX g3RXX                      !
        TINC RIY g3RYY
        TINC RIx1res HIRERAN               !
Endif

If RIXIY g10 then
        TINC STACPR TACg10
Endif
END
```